Advanced Atomic Force Microscopy:
3D Printed Micro-Optomechanical Sensor Systems

Zur Erlangung des akademischen Grades eines
DOKTORS DER NATURWISSENSCHAFTEN (Dr. rer. nat.)

von der KIT-Fakultät für Physik des
Karlsruher Institut für Technologie (KIT)
genehmigte

DISSERTATION

von

Dipl.-Phys. Gerald Göring

Tag der mündlichen Prüfung: 02. Februar 2018
Referent: Prof. Dr. Thomas Schimmel
Korreferent: Prof. Dr. Gerd Ulrich Nienhaus

Contents

1 Introduction

Since the recognition of the limit of conventional optical microscopy by Ernst Abbe in the year 1873 [1], new ways have been developed to provide deeper insights into the microscopic world. This is becoming increasingly important due to the ongoing miniaturization in technology or material science. The advance of nanotechnology has produced manifold approaches to obtain images in the nanometer regime.

The invention of scanning electron microscopy (SEM) enables us to surpass the diffraction limit of light by scanning the sample with electrons. However, SEM requires vacuum conditions, which inherently inhibit in situ measurements of samples containing liquids, for example biological systems. Additionally, samples often have to be coated with a conducting material to prevent charges, which often leads to a reduction in imaging resolution and to artifacts. While SEM produces impressive high resolution images, it lacks quantitative topographic information. Scanning probe microscopy (SPM) was invented by Binnig and Rohrer [2] in 1982 and provided a tool for the evaluation of topography, thus contributing greatly to many surface processes. Here, a tunneling current between a sharp conductive tip and a sample is measured and used as a feedback for the measurement of the topography. Scanning tunneling microscopy (STM) was the first technique that provided true topographical information in the nanoscale range and the ability to manipulate matter down to the resolution of single atoms [3]. Since the current between the tip and the sample depends on the conductance of the sample surface, it typically has to be metallic or at least semi-conducting.

To enable measurements on non-conductive samples, Binnig, Quate and Gerber invented the atomic force microscope (AFM) [4] in 1986. Here, the probe consists of a cantilever beam with a sharp tip on the bottom of the free end. The tip points towards the sample and is brought into direct contact with it. When the topography changes during the scan, the cantilever deflects. This deflection is measured with a laser that is focused on the back of the cantilever and detected with a split photodiode which delivers a linear signal for the deflection of the cantilever. Despite this contact mode, there are other advanced modes of operation like the intermittent contact mode, where the cantilever is actuated at its freeair resonance frequency, whose amplitude is damped when the tip oscillates near the sample surface. This reduced amplitude can be used as a feedback signal to survey the topography of a sample. AFM is still one of the most important techniques in nanoscience and exists in many variations.

Despite its many advantages, a major disadvantage of AFM is its size. Whereas typical scan ranges are smaller than 100 µm, the AFM head, consisting of the cantilever holder and the op-

tical readout for the cantilever, is in the decimeter range, which is orders of magnitudes bigger. This inherently inhibits in situ measurements on the surface of large objects or even endoscopic measurements. The probes used for AFM are typically etched from silicon or silicon nitride. This technology provides a limited degree of freedom in design and is associated with variations typically more than 30 % of critical properties of the final device, such as its bending resonance frequency [5, 6]. The alignment and calibration procedure for each newly mounted cantilever requires an experienced operator. To simplify the setup, different self-sensing techniques have been introduced comprising piezoelectric, piezoresistive, tunnel magnetoresisitve or capacitive readouts of the cantilever bending. Despite the additional and expensive fabrication steps, they have limited sensitivity [7–9].

Another approach is the use of an interferometric readout principle in which light is partially reflected by a reference mirror and the cantilever itself and then collected by an optical fiber to return a distance dependent light intensity [10–12]. A modern approach, using focused ion beam milling leads to a cantilever carved out of the glass at the end of an optical fiber. With this approach, the laser alignment process becomes unnecessary [13, 14] but the production of such highly integrated, tipless cantilevers is extremely time-consuming.

A possible route to effective AFM probe fabrication may be found in 3D printing, which was introduced to produce three dimensional objects in a layer-by-layer manner [15]. Two-photon polymerization (TPP) lithography provides a viable solution to printing microscopic objects in the nanometer range [16, 17]. This 3D fabrication method is mainly used to make small objects which interact with light to yield products such as photonic wire bonds [18], photonic metamaterials [19] or photonic surfaces [20].

In this work, two-photon polymerization 3D lithography is used to create a cantilever equipped with a tip on top of a fiber array. The optical properties of the resist and the possibility to shape freeform optical grade surfaces are used for guiding, absorbing and reflecting optical beams within the device. The fibers are arranged in a row and the first fiber is used to photothermally actuate the micro cantilever at its resonance frequency. The second fiber is used as an interferometer on which the cavity is formed between the fiber facet and a freeform mirror e.g. on the backside of the cantilever. With the third fiber, light can be collected from an aperture at the very end of the tip. A fourth fiber is equipped with a freeform mirror, which focuses sideways on the tip. This can be used for either detecting light from or shining light on the tip. This near-field optical information integrates the concept of scanning near-field optical microscopy (SNOM) [21] into the new self-sensing micro-optomechanical system.

The cantilever actuation for tapping mode is accomplished by optothermal heating, which allows the system to operate in changing environments or conductive liquids. The actuation process is investigated by congruent simulations of heat transfer and wave optic properties. To ensure that the polymer meets the required mechanical criteria to operate as a tip, long-term wear measurements are performed and the shape of the tip is determined by deconvolution. In addition, 3D printing technology is used to modify commercial silicon cantilevers. By adding a calculated and

simulated framework structure of resist on the back of the cantilevers, the eigenmodes and the quality factor of the resonance spectrum are modified to improve the dynamic properties in order to obtain high sensitivity for small tip-sample forces. To sum up, with 3D printing it is possible to improve existing approaches in AFM or design new superior ones, which can combine the advantages of AFM with the possibility of SNOM to measure the optical near-field.

2 Fundamentals

2.1 Atomic Force Microscopy

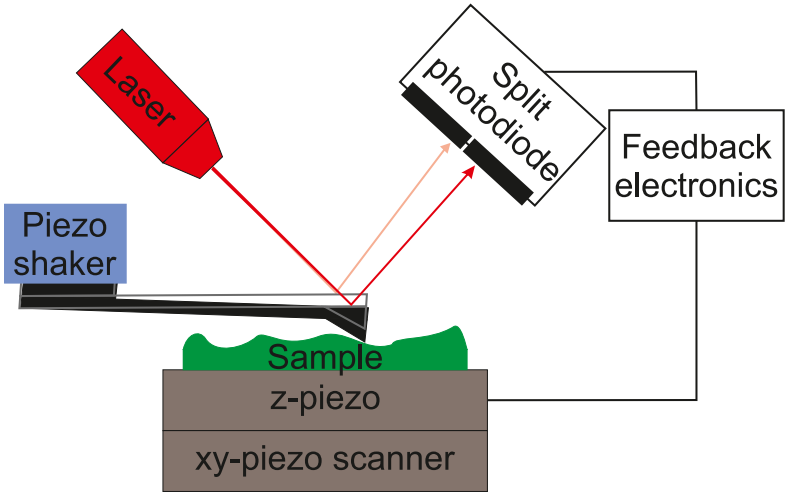

Figure 2.1: Basic principle of an AFM. The sample is scanned in the xy-direction, while a feedback loop keeps the deflection of the cantilever constant. Adopted from [22].

Nanotechnology is omnipresent in smartphones, TVs and cars. They all possess computerchips with transistors in the nanometer scale [23]. To be able to develop technology of this size, one has to know what happens during the fabrication processes. For this, an image of the topography of the surface is needed, but the nanoworld is not accessible via classical microscopy due to the Abbe limit. To overcome this problem, scanning probe microscopy was developed. In particular, atomic force microscopy can be used to inspect sample quality or investigate intramolecular forces [24] or samples down to the atomic range [25].

The atomic force microscope (AFM) consists of a cantilever equipped with a tip and is able to measure forces in the sub-piconewton range [26]. To measure these forces, the cantilever, which acts as a small leaf spring, is brought into contact with the surface and a small force is applied to preload the cantilever (see figure 2.1). Then the sample is scanned in the x- and y-directions and the change of topography leads to bending of the cantilever. When the deflection of the cantilever is held constant with a z-feedback loop, the feedback signal matches the topography. This basic principle has been developed further over the last decades for modern micro- and nanotechnology.

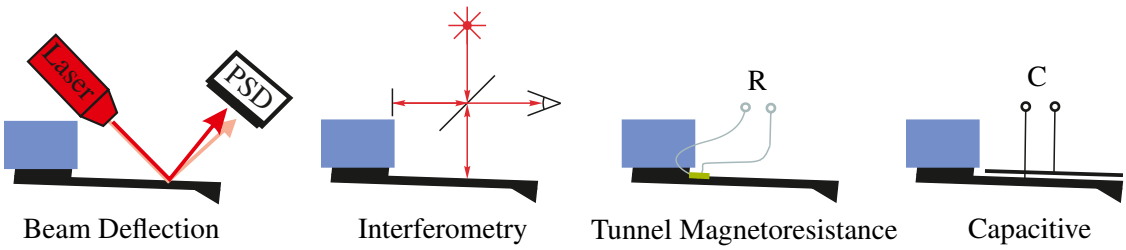

Figure 2.2: Variations of readout methods. Adopted from [22].

2.1.1 Readout Method

Optical deflection readout

Different approaches can be found in the literature to measure optical deflection, . These are depicted in figure 2.2. Whilst most commercially available AFMs use the beam deflection read-out, there is no solution which fits all needs. The optical deflection read-out is a method with high sensitivity, but it lacks compactness due to the macroscopic elements. This leads to slow z-feedback due to the large mass, because either the whole sample has to be moved in the z-direction or the complete readout system including laser and photodiode. Additionally, the bulky AFM head, which consists of the readout and alignment mechanism, prevents easy access to the sample. This is the main reason for the lack of AFMs which include advanced optic methods like fluorescence microscopy. Some approaches combine both methods, but only allow the inspection of transparent samples from the bottom while the AFM operates from the top. Before taking a measurement, the laser has to be aligned to be focused on the cantilever and afterwards the split photodiode has to be aligned so that the reflected laser hits the center. This step has to be performed whenever the environment changes, due to the change of the refractive index.

Interferometric readout

The interferometric readout is the second method that uses a laser. The sensitivity is the same as for the beam deflection readout [27], but it is only possible to measure the deflection of the cantilever in one direction so that the lateral deflection cannot be distinguished from the deflection along the cantilever. Here, a laser beam is reflected by the cantilever and interferes with a reference beam, as in a Michelson interferometer. Different setups have been proposed. Schöneberger and Alvarado [12] reported the first interferometric readout. Rasool *et al.* [10] proposed a read-out by using an all-fiber Fabry-Pérot interferometer, so no optical lens system is needed. It is a simple setup, but the alignment is hard to perform, since the fiber has to be positioned with micrometer precision. Therefore, a piezo ring actuator is utilized. Since the same fiber is used for coupling the light in and out, the input has to be split to allow the connection of the laser and the photodiode. This can be done by a classical 3 dB 2×2 coupler, which has to be passed two times and thus leads to a loss of a factor of four, or it is possible to use an optical circulator. The circulator is a three port device and is designed so that light which enters one port, exits from the

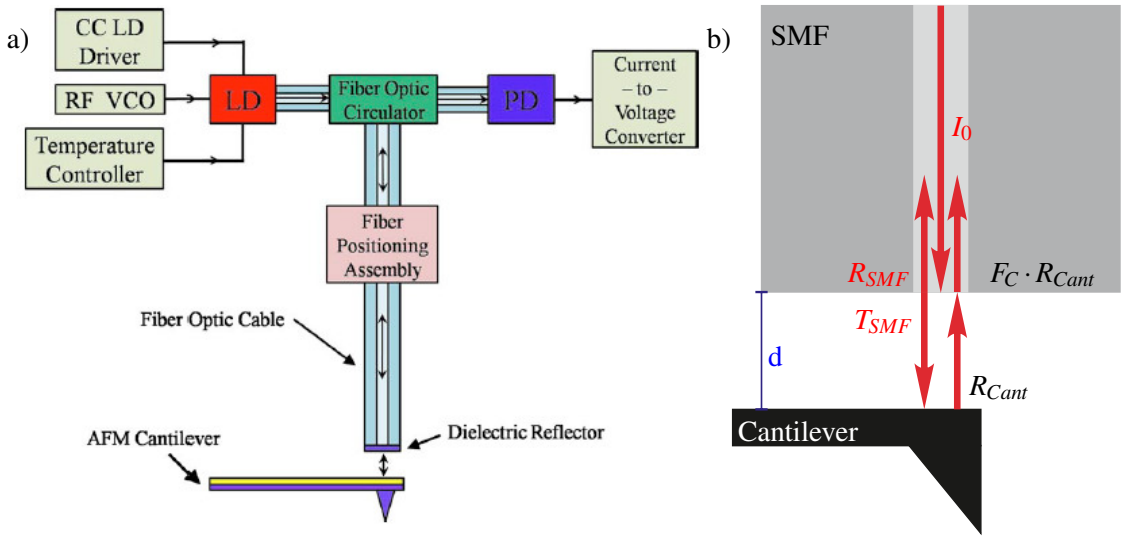

Figure 2.3: Interferometric distance readout concept of a cantilever with fiber optics. **a)** The experimental setup proposed by Rasool *et al.* [10]. **b)** Light transmission and reflection of this setup. The light is partly reflected on the fiber facet and on the cantilever and interferes depending on the distance d between the fiber facet and cantilever. Adopted from [22].

next. Thus, when coupling the laser into port 1, the light is guided into port 2, were the readout fiber is connected. The reflected light, which couples into port 2 is then guided to port 3, where the photodiode is connected to convert the light into a photo current, which is then converted, by a transimpedance amplifier, into a voltage which can be fed into the AFM controller. To prevent laser light from being partly reflected back into port 3, which would be guided to port 1 with the laser connected, a Faraday insulator is used.

Since the interferometric distance readout is mainly used in this work, it will be discussed in more detail. The optical cavity depicted in figure 2.3 is formed by the facet of the single mode fiber (SMF) and the cantilever. The cantilever acts as one side of the mirror, whereas the facet acts as the other side. Light is partly reflected on the fiber-air interface and can be used as a reference beam. At the cantilever, a part of the transmitted light is reflected back and couples with a coupling efficiency F_C back into the fiber core. Assuming similar reflective indices for the fiber end R_{SMF} and the cantilever R_{Cant}, a monochromatic laser and high order reflections, it is possible to describe the reflection at the cavity with the well-known Fabry-Pérot-Etalon formula [28] in which the intensity at the photodiode is given by

$$I^{(r)} = \frac{4R\sin^2\frac{\delta}{2}}{(1-R)^2+4R\sin^2\frac{\delta}{2}} I^{(i)} \tag{2.1}$$

with the phase shift

$$\delta = \frac{4\pi}{\lambda_0} nd \tag{2.2}$$

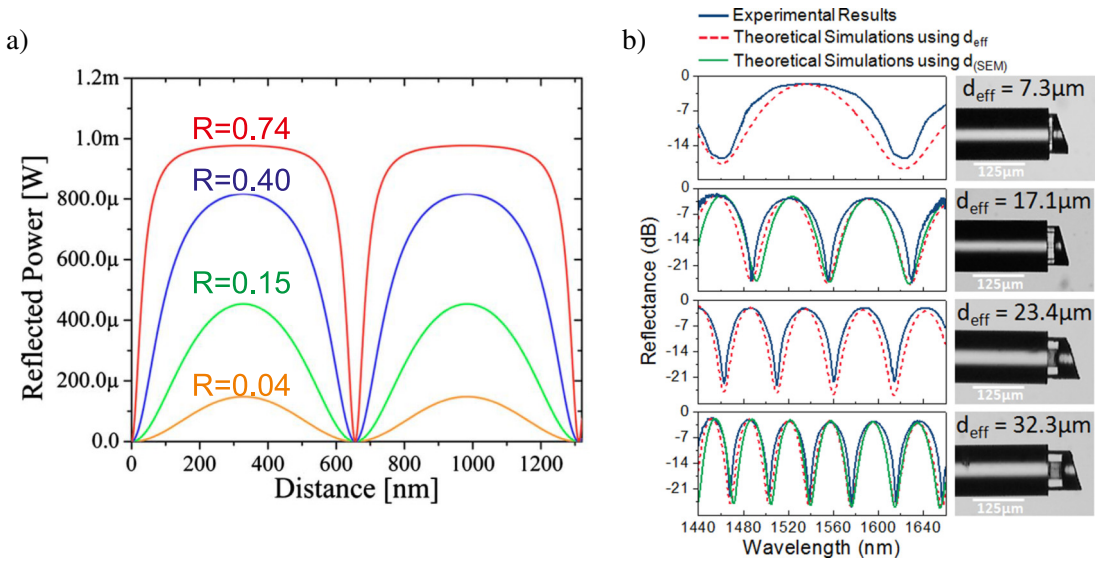

Figure 2.4: **a)** A simulation of the reflected power for a wavelength of 1311 nm and different reflectivities. **b)** Measurements of different cavities with fixed length and a tune of the wavelength. The cavities are produced with 3D printing. Adopted from [22].

and the incident intensity $I^{(i)}$, the reflectivity $R = 1 - T = R_{Cant} = R_{SMF}$, the refractive index n of the medium in the cavity and the vacuum wavelength of the laser λ_0. Maxima of the intensity are shown by

$$m = \frac{\delta}{2\pi} = \frac{2nd}{\lambda_0} \qquad m \in \mathbb{N}. \tag{2.3}$$

The calculation of the mode field overlap of the light reflected at the cantilever and the mode field of the SMF can be simplified by the Gaussian approximation [29]. For a perfectly aligned fiber and a cantilever parallel to the fiber facet, only the distance d causes the mismatch and thus the optical signal can be used as a method for measuring the distance. The coupling efficiency F_C of the light which is transmitted at the fiber facet and couples back into the SMF can be calculated by the Gaussian field approximation [10, 28]

$$T = F_C = \left[1 + \left(\frac{d}{2ks^2}\right)^2\right]^1 = \left[1 + \left(\frac{d}{z_r}\right)^2\right]^{-1} \tag{2.4}$$

with the wavenumber in free space k, the mode field radius w, the spot size of incident beam $s = \sqrt{2}w$ and the Rayleigh length

$$z_r = \frac{\pi n w}{\lambda_0}. \tag{2.5}$$

This leads to an effective reflective index of the mirror of

$$T_{eff} = F_C \cdot R_{Cant}. \tag{2.6}$$

Thus, using equations 2.1 - 2.3 it is possible to match R_{eff} of the cantilever to the air-SMF interface when changing the distance d or the wavelength λ_0. The equations do not match perfectly,

since they consider high order reflections, which is not the case in this setup, due to the low refractive indices of the fiber and cantilever surface, and the equations do not take the coupling losses into account. In figure 2.4 a simulation of the reflected power of a distance sweep for a fixed wavelength of the laser $\lambda_0 = 1311\,\text{nm}$ and different reflectivities is depicted, as well as measured wavelength tunes for different cavity lengths. The cavities were written via direct laser writing on an SMF to demonstrate the influence of the distance d. To measure the distance between the cantilever and the fiber facet, the wavelength λ_0 is kept constant. When, during the measurement, the cantilever bends and thus changes the length of the cavity, a change of the intensity on the photodiode is induced. This leads to a change of the photo current and thus to a change of the voltage produced, which is used as a feedback signal. Since the intensity for different distances has the shape of a sine wave for low reflectance, the sensitivity depends on the wavelength and distance. For this reason, a laser that has an external cavity and is tunable between 1520 nm to 1620 nm is used to select the wavelength with the highest sensitivity. For classical setups the alignment procedure is similar in complexity to the one with the deflection readout but can be more complicated due to the small distance between the fiber and the cantilever [30]. New approaches produce the cantilever directly on top of the SMF, which makes alignment unnecessary. However, the fabrication relies on a complex process of laser processing, carving and focused ion beam milling [13, 14, 31].

Self Sensing Approaches

In addition to readout methods using a laser, other approaches have been developed, such as using a quartz tuning fork [32, 33], piezoresistive cantilevers [8, 34], piezoelectric sensors [35] or capacitive sensors [36]. However, practically all htese methods suffer from cantilever mass production issues [37]. Due to the increasing demand for highly efficient and low-cost magnetic hard disks for data storage, magnetic tunneling junctions can be used in state of the art read-heads in hard drives [38, 39]. Including the miniaturization opportunities [40], this effect can be used for self-sensing cantilevers when they are adapted for high strain sensitivity [41]. These sensors are used in this work, which is why they are further discussed.

The anisotropic magnetoresistive effect was discovered in 1856 [42] and led to the discovery of the giant magnetoresistive effect (GMR) in 1986 [43] (Nobel prize in Physics 2007 to Albert Fert and Peter Grünberg), the development of aluminum oxide tunnel junctions [44, 45] and magnesium oxide tunneling junctions [46, 47], which together led to an increase in strain sensitivity.

The sensors consist of up to ten layers, but can be schematically explained with only three layers; a ferromagnetically pinned reference layer, a thin dielectric insulaton layer and a third ferromagnetic layer. The insulaion barrier is thinner than a few nanometers, which enables electrons to

tunnel through, which is why it is called a tunnel barrier. The full quantum mechanical current can be calculated by Simmons' expression from 1963 [48]

$$I(U) = \varphi(t_b)\left(\left(\Phi - \frac{U}{2}\right)\exp\left(-1.025\sqrt{\Phi - \frac{U}{2}}t_b\right) - \left(\Phi + \frac{U}{2}\right)\exp\left(-1.025\sqrt{\Phi + \frac{U}{2}}t_b\right)\right) \tag{2.7}$$

with the current I as a function of the barrier height Φ, the applied bias voltage U and the barrier thickness t_b.

The electric current in the electrodes is split into two partial currents since they are conducted in two sub-bands, one with spin-up N↑ and one with spin-down N↓. The electron spin must be conserved during tunneling, which only allows tunneling between two sub-bands with the same spin polarization. When both electrodes are in parallel magnetization, which means a magnetization in the same direction, the sub-bands of both electrodes are equal. However, when the magnetization is different, a mismatch between the sub-bands is introduced, which leads to a decrease in current. In figure 2.5 the concept is explained schematically. This means that the conductance G between both layers can be expressed by the angle α between the magnetization of the electrodes by

$$G(\alpha) = \frac{1}{2}(G_p + G_{ap}) + \frac{1}{2}(G_p - G_{ap})\cos\alpha \tag{2.8}$$

where G_p and G_{ap} are the conductance in parallel and antiparallel state. This effect is used for high sensitivity magnetic field sensors, which are often used in read-heads of hard drives [49]. When using magnetostrictive materials in the electrodes with one electrode magnetically pinned, the TMR-junction can be used as a strain sensor, since the magnetization of the unpinned electrode rotates when strained [50], due to the inverse magnetostrictive effect [51].

2.1.2 Tip-Sample Forces

The tip is sensitive to various forces from the sample and the surrounding medium. These might be attractive or repulsive, depending on the distance, material or charge of the sample and tip. There are large differences between measurements in water and vacuum due to damping properties and capillary effects. The forces cannot be separated since they add up vectorially. It is important to know which force is dominant during the measurement to prevent a hopping between the regimes. The most important ones are listed below.

Van der Waals Force

Different kinds of interacting forces between molecules are important and depend on the character of the polarization of the molecules themselves. The London dispersion force can be described as Van der Waals force in a narrower sense [53]. This force describes the spontaneous formation of electric dipoles even in non-polarized materials. These dipoles interact with other charges in

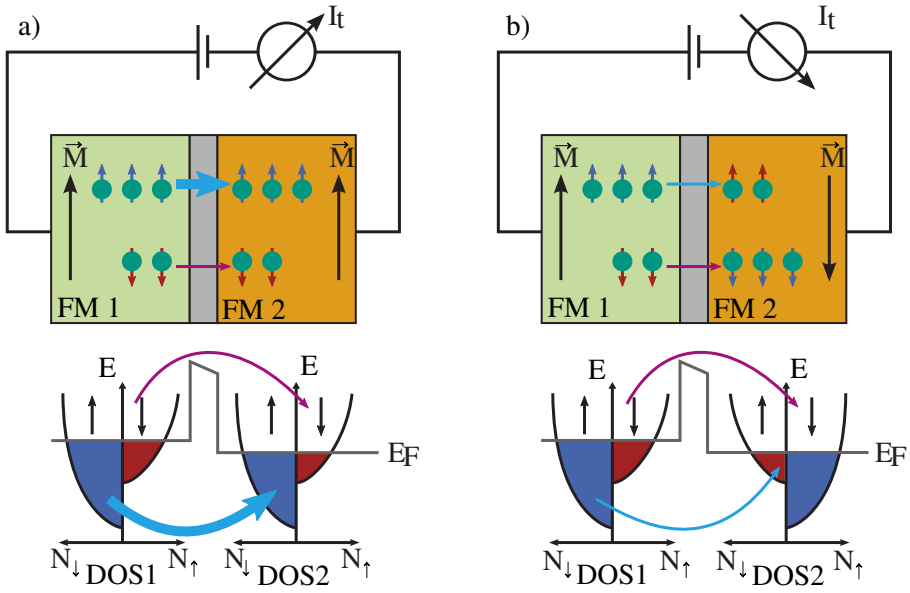

Figure 2.5: Principle of tunnel magnetoresistance sensors. Two ferromagnetic (FM) layers are divided by a thin insulator. When changing the magnetization of the layers, the densitiy of states (DOS) is shifted, which leads to the formation of different sub-bands. Since the electrons conserve their spin when tunneling from one layer to the other, the conductance is proportional to the product of the Fermi level of spin polarized sub-bands of the electrodes. This leads to a change of the conductance, when changing the magnetization of one layer. **a)** The schematic of a parallel configuration with high conductance, and **b)** an antiparallel configuration with low conductance. Adopted from [52].

a molecule and induce polarity [54, p. 145ff], which leads to an attractive force with a potential in the form

$$U_{VDW} = -\frac{C_{VDW}}{r^6} \tag{2.9}$$

with the interaction constant C_{VDW} of the Van der Waals force and the distance r between the dipoles. This dispersion force is always present in contrast to induction or orientation forces, which makes it one of the most important forces in AFM. It typically dominates the distance range between sample and tip of 0.2 nm to 10 nm [53, p. 107]. Due to this large range one has not only to consider the molecule or atom at the top of the tip when calculating the force, but to take the tip itself into account. Typically, this is done by assuming the tip as a half-sphere with radius R. The interaction energy for a large sample can then be approximated by

$$U_{VDW} = -\frac{HR}{6z} \tag{2.10}$$

which leads to the force

$$F_{VDW} = -\frac{HR}{6z^2} \tag{2.11}$$

with the Hamaker constant H [55] with values around $1 \cdot 10^{-19}$ J [56] and the tip-sample distance z. The negative sign indicates that the force is attractive. As the forces are proportional to z^{-2} they are considered as long range forces. For distances below 10 nm they are in the range of 0.1 nN [57].

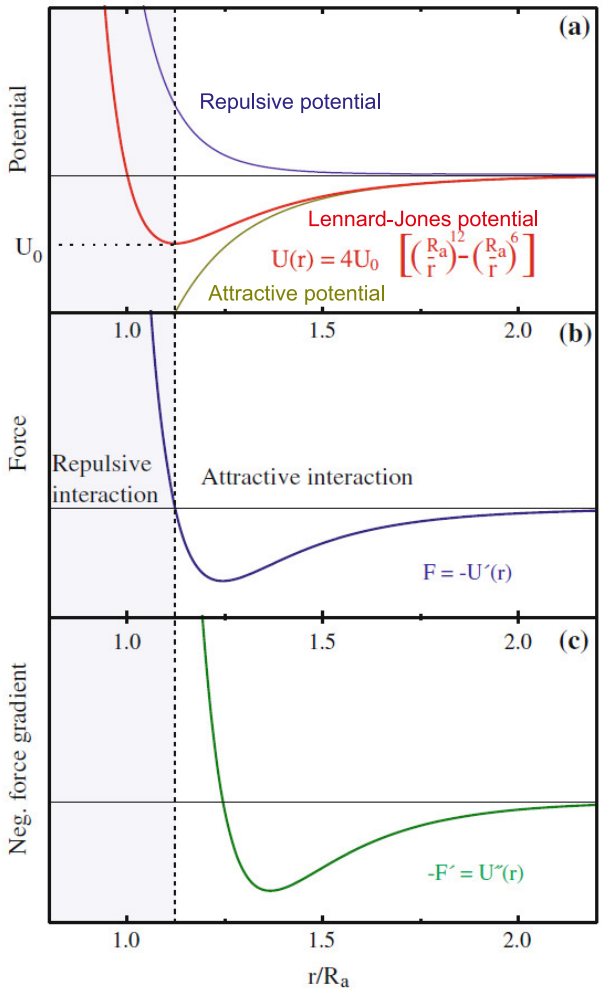

Figure 2.6: Plot of the Lennard-Jones potential in red, the calculated force in blue and the force gradient in green. At $r = R_a$, the potential is set to be zero and at the equilibrium state, where no force is acting, the potential is U_0. Adopted from [22].

Pauli Repulsion

The force that keeps atoms from penetrating each other was postulated by Wolfang Pauli in 1925. The Pauli exclusion principle inhibits a significant overlap of the quantum mechanical state of the charge clouds of two electrons [58, 59]. George Uhlenbeck and Samuel Goudsmit were inspired by this work and introduced the spin of electrons [60] which increased the quantum numbers from three to four [61]. This force is responsible for the repulsion of the tip from the sample. It is purely quantum mechanical and the potential can be approximated by r^{-12} [56, p. 147].

Lennard-Jones Potential

Adding the Van der Waals and the Pauli potentials results in the Lennard-Jones potential, which describes the potential of neutral atoms. It can be written as

$$U_{LJ}(r) = 4U_0 \left[\left(\frac{R_a}{r} \right)^{12} - \left(\frac{R_a}{r} \right)^{6} \right] \tag{2.12}$$

were U_0 is the potential well depth, r the distance between the atoms and the equilibrium distance R_a.

Figure 2.6 shows the course of the potential as well as the force and the force gradient. This potential is calculated for single atoms, but in AFM the sample as well as the tip are not single atoms but ensembles of atoms, which causes additional effects such as elastic deformation.

Electrostatic Force

The Lennard-Jones potential describes the force between atoms for small separations. For larger separations, other forces such as electrostatic force, become dominant [57]. For a difference in potential ΔV, the electrostatic energy is given by

$$U_{el} = -\frac{1}{2} C(z)(\Delta V)^2 \tag{2.13}$$

with the capacitance C between sample and probe. This leads to the force in the form of

$$F_{el} = -\frac{1}{2} \frac{\partial C}{\partial z} (\Delta V)^2. \tag{2.14}$$

For a potential of 1 V, a tip radius of 50 nm and a distance $z = 1$ nm between sample and tip, a force of approximately 1 nN can be calculated. This is smaller than the Van der Waals force [56, p. 149]. For distances larger than 10 nm, electrostatic forces become stronger than the Van der Waals force.

Capillary Force

In addition to the inherent forces between the atoms and molecules, other effects can disturb AFM images. One of them is capillary forces. Due to the humidity at room temperature and pressure, a thin water layer or droplets are always present on top of the sample. The thickness and size of the droplets depends on the humidity as well as on the sample. In particular, water is always present on titanium and graphite samples [63]. When the tip touches the water layer, a meniscus develops which attracts the tip. It can be calculated by

$$F_w = \frac{4\pi R E_1 \cos\theta}{1 + z/d} \tag{2.15}$$

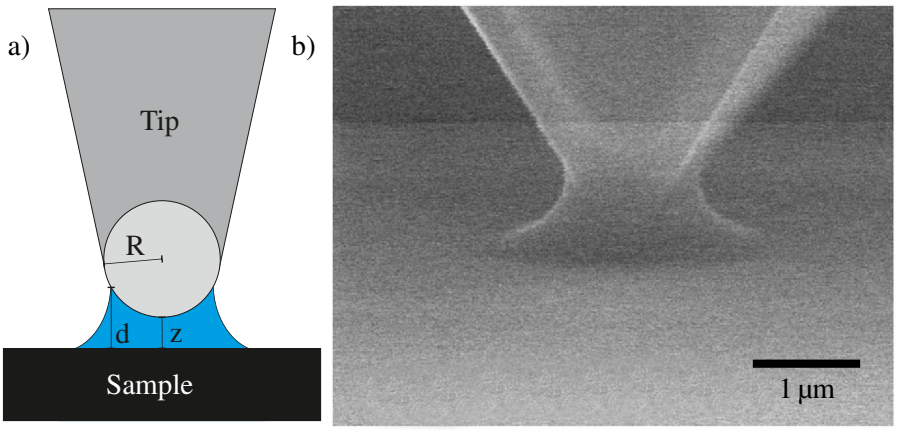

Figure 2.7: **a)** Schematic of a water meniscus formed between the sample and the tip. Adopted from [22]. **b)** An environmental scanning electron microscope image shows such a meniscus. Adopted from [62].

with the radius R of the probing tip, the surface energy E_1 of the liquid film (72 mJ for water) the distance z between tip and sample and the height d of the meniscus. This can lead to forces in the region of 0.1 nN [64] and can cause different artifacts when scanning a sample in non-contact mode. In this case, the tip can penetrate the water layer for high amplitudes or scan along the water layer for small amplitudes or low applied forces. To overcome this problem, it is possible to measure in low vacuum (vapor pressure of water at room temperature is 32 mbar [65, p. 6-10]) or change the environment from air to water and fully immerse the sample.

2.1.3 Modes of Operation

Over the decades, different modes of operation have been developed. Besides the topography, practically all physical properties such as Young's modulus [66], thermal conductivity [67], piezo activity [68] or surface potential [69] can be measured. Depending on the property of interest, certain modes should be chosen. In this work different modes, which are presented below, are used.

Contact Mode

There are two possible modes for contact mode. Both use the repulsive force when the cantilever is brought into contact with the sample to measure topography as well as friction. It is possible to leave the sample at the original z-height and just use the change of the deflection of the cantilever to acquire the topography of the sample. For this the relation δ_{cal} between the cantilever deflection and the measured photo current has to be calibrated by a force distance curve (see section 2.1.4). This mode is only possible when the area scanned is small and has a low profile topography. Additionally, the force F_z which equals

$$F_z = k_z \cdot \Delta z \tag{2.16}$$

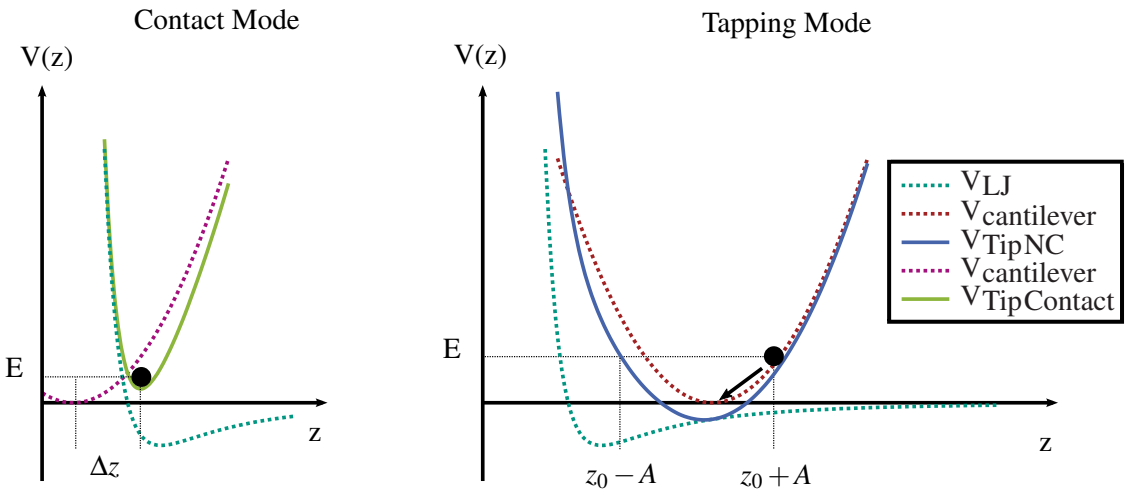

Figure 2.8: Potentials for contact and non-contact (tapping) mode. To have a stable measurement, the tip is pressed against the sample until the repulsive force becomes dominant. In tapping mode, the cantilever is driven at its free-air resonance frequency. When the tip approaches the sample, long range forces disturb this potential which leads to a shift in resonance frequency and phase. Adopted from [52].

also known as Hooke's law, where k_z is the spring constant of the cantilever and Δz the deflection, changes with the topography, which can lead to artifacts.

The second contact mode features a feedback in z-direction. When the sample is scanned, a feedback loop controls the sample's height to keep the deflection of the cantilever constant. This way it is not necessary to know the calibration factor δ_{cal} of the readout system but rather the traveled distance Δz has to be known. For small actuations the piezo is linear enough to have a travel proportional to the applied voltage, but for larger ones a strain gauge should be used.

The cantilever's deflection can be modeled by the interplay of the Lennard-Jones potential and the harmonic oscillator potential [70]

$$V_{spring}(z) = \frac{k}{2}(z - z_0)^2 \tag{2.17}$$

which is responsible for the force calculated by formula 2.16. Figure 2.8 shows the plotted effective potential, which shows a single minimum.

Intermittent Contact Mode

The intermittent contact mode or tapping mode is a dynamic mode. In this mode, the cantilever is driven near its resonance frequency. To drive the cantilever, typically a piezo is used, but it is also possible to drive the cantilever optothermally [71] or magnetically [72]. In this mode, the actuation frequency is fixed and the amplitude is used as feedback signal. When forces act on the tip, the resonance frequency shifts, depending on the direction of the force. For attractive forces, the resonance frequency shifts to a lower frequency and vice versa for repulsive forces.

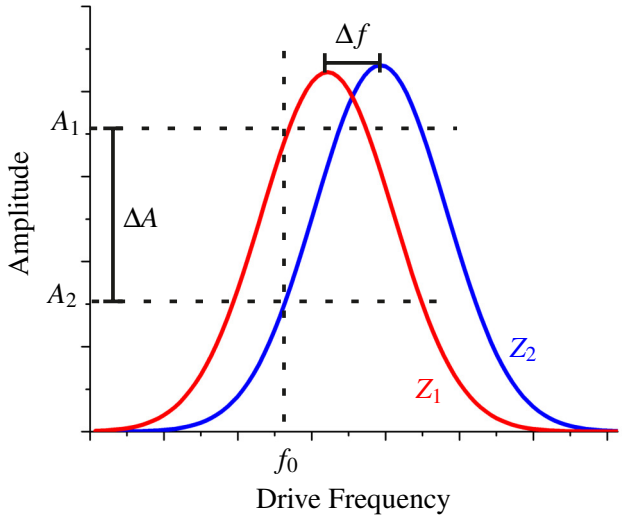

Figure 2.9: Resonance frequency of a cantilever far away from the sample (red) and when repulsive forces act at the tip (blue). When driving at a fixed frequency, the measured amplitude is reduced due to the shifted resonance frequency. Adopted from [22].

Figure 2.9 depicts this situation for repulsive forces. The description of this distorted harmonic oscillator is

$$m\ddot{z}(t)+\frac{2\pi f_0 m}{Q_0}\dot{z}(t)+k_z(z_0-z(t))=\underbrace{A_d K_z\cos(2\pi f_d t)}_{\text{external driving force}}+\underbrace{F_{ts}\left[z(t),\dot{z}(t)\right]}_{\text{tip-sample force}} \tag{2.18}$$

with $z(t)$ as time dependent position of the tip and the parameters k_z, m, z_0 and $f_0=\frac{1}{2\pi}\sqrt{\frac{K_z}{m}}$ as spring constant, effective mass, equilibrium position and the eigenfrequency of the cantilever. The quality factor Q_0 will be further discussed in section 2.1.5. The cantilever is driven with the amplitude A_d at the frequency f_d. The resonance frequency f_0 of the cantilever can be found by tuning the cantilever far away from the surface. Here, the tip-sample forces can be neglected and a steady state solution for the driven-damped harmonic oscillator can be found with the ansatz

$$Z(t=0)=z_0+A_0\cos(2\pi f_d t+\phi) \tag{2.19}$$

with the phase ϕ between excitation and oscillation. It can be used to solve the equation 2.18, which leads to an expression for the amplitude A_0 and phase ϕ

$$A_0 = \frac{A_d}{\sqrt{\left(1-\frac{f_d^2}{f_0^2}\right)^2+\left(\frac{1}{Q_0}\frac{f_d}{f_0}\right)^2}} \tag{2.20}$$

$$\tan\phi = \frac{1}{Q_0}\frac{\frac{f_d}{f_0}}{1-\frac{f_d^2}{f_0^2}}. \tag{2.21}$$

When taking the highly non-linear tip-sample force $F_{ts}\left[z(t),\dot{z}(t)\right]$ into account, an analytic solution becomes complicated. In literature it is proposed to focus on steady state solutions and

expand the tip-sample force into its Fourier series [73], which results in two coupled equations. They have been discussed by Dürig [74] and Sader *et al.* [75] leading to

$$\sin\phi = -\left(\frac{A}{A_0}\frac{f_d}{f_0} + \frac{Q_0\Delta E}{\pi k_z A A_0}\right) \tag{2.22}$$

where ΔE is an expression for the dissipated energy. Therefore, the phase can be used to measure energy dissipation on different materials, even if there is no topographical difference between them [76].

Multi-Frequency Mode

In tapping mode one has to estimate the topography of the sample and select an adequate amplitude. For high topographies, high amplitudes should be chosen to ensure that the cantilever is always able to overcome high areas to prevent tip degradation and to have a stable feedback. But this comes at the cost of higher noise levels and lower sensitivity for short-ranging forces [77, 78]. The multi-frequency mode is able to combine both advantages by using one harmonic of the cantilever for the topographical feedback and another harmonic with a small amplitude for high-sensitive scanning [79]. The setup of this mode is basically the same as for the tapping mode in terms of feedback, but an additional eigenmode is actuated with constant oscillation energy and frequency. Since both signals are filtered through a lock-in amplifier, they do not disturb each other. During the measurement two additional channels can be displayed with the phase and the amplitude of the higher harmonic oscillation, both with high sensitivity for mechanical or electromagnetic properties [80].

2.1.4 Force Distance Curves

All sensors that measure the distance return a position signal either directly in a voltage or in another form like current, resistance or capacity, which has to be converted to a voltage through an adequate amplifier or circuit. Whereas the gain of the amplifier or circuit is known due to the design, the conversion of the position signal to the distance in meters depends on many factors. For the classical deflection readout on which a laser is focused on the tip and the reflected light is directed to a split photodiode, the voltage produced by a differential transimpedance amplifier highly depends on the coating of the cantilever, the position of the focus point and the size or even the form (triangular or right angular shaped) of the cantilever. The same applies to TMR sensors where the conductance as well as the rotation of the magnetization of the strain sensor highly depends on size, form, magnetization and purity of the layers. It is important to know the sensitivity to be able to estimate the applied forces during measurement, calculate the topography in non-feedback modes and to determine the overall performance of the readout system. To determine the sensitivity, the tip can be deflected by a known distance and the sensor signal recorded. When the sensor signal is plotted over the traveled distance, the plot is called a force distance curve.

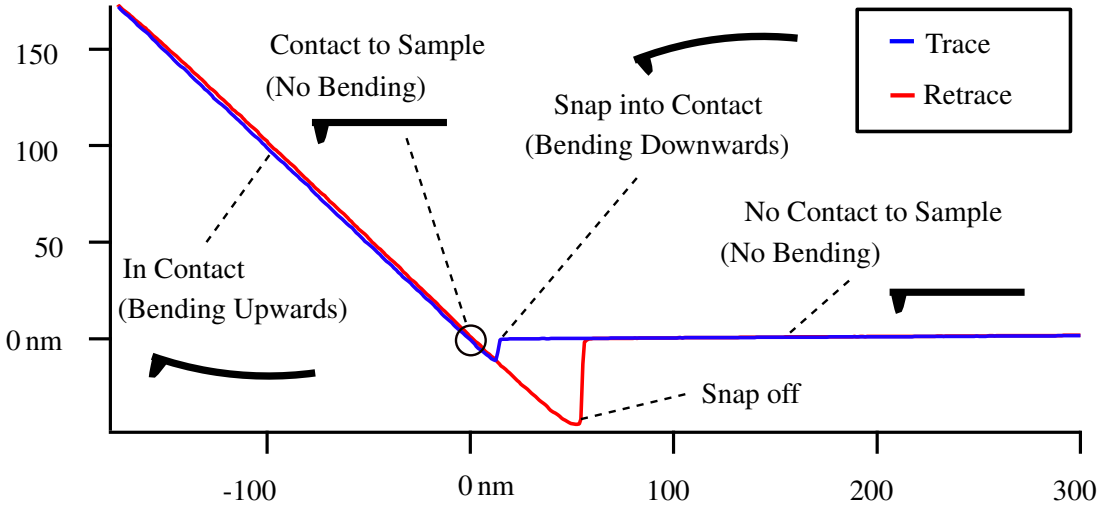

Figure 2.10: Typical force distance curve acquired with the Asylum MFP3D AFM. When approaching the sample, the cantilever snaps into contact when attractive forces are stronger than the restoring force of the cantilever. This leads to a down bending of the cantilever. Further movement leads to a straightening of the cantilever and finally to an upbending. When withdrawing the cantilever, it bends down and even further downwards then when approaching due to the formed water meniscus and other additional adhesion forces. When the restoring force of the cantilever is larger than the adhesion, the cantilever snaps off.

In figure 2.10 a force distance curve is plotted. It contains a trace and a retrace plot. When approaching the surface with the cantilever on an actor, such as a piezo, the cantilever is straight until the Van der Waals force attracts the tip. Then the tip snaps onto the surface. When the piezo further elongates, the cantilever stays at the surface and starts to bend back until the cantilever is straight. This point is defined as zero. After this point, the cantilever starts bending upwards and the deflection signal increases. For a linear sensor, which means that the signal output is proportional to the traveled distance as in the classical deflection readout, the slope equals the sensitivity. For a non-linear readout, such as the interferometric readout, the sensitivity changes while the cantilever is deflected. Therefore, the laser should be set to a wavelength in which the cantilever operates in a linear regime. When retracting the sample surface from the cantilever, it starts to relax until it bends downwards due to adhesion. When the restoring force of the cantilever becomes bigger than the adhesion forces, it snaps off the surface. The adhesion force includes the capillary force from the water meniscus as well as other forces like stickiness [81] or chemical [82] or biological bonds [83].

2.1.5 Properties of Cantilevers

The cantilever with its tip is the most important part of the AFM and is typically the limiting factor for lateral resolution. It is crucial to choose a cantilever with the right properties. For instance, a cantilever for contact mode has to have a spring constant way below the one for a cantilever for tapping mode to reduce the force on the sample.

Cantilevers are available in two forms, V-shaped cantilevers for contact mode and rectangular ones, which are suitable for dynamic and contact mode, depending on the dimensions. Whereas

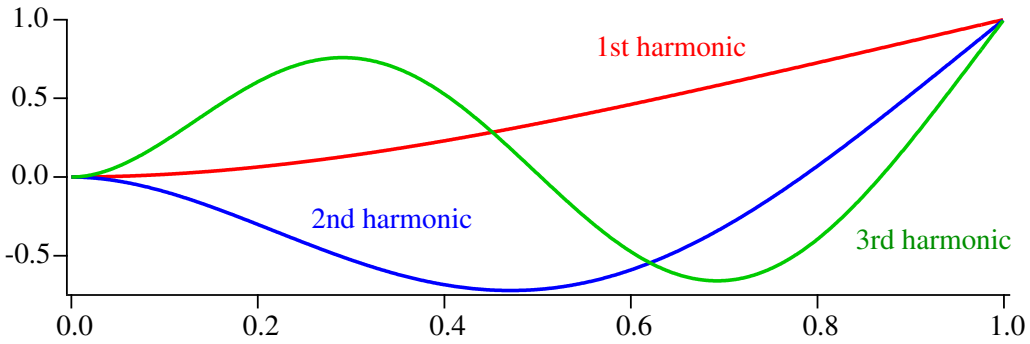

Figure 2.11: Plot of the first three mode shapes of a cantilever beam with one fixed end on the left and one free end on the right.

in contact mode, the cantilever mainly acts as a spring to ensure that the tip stays in contact with the sample, the dynamic mode requires further calculations. The spring constant k of a rectangular cantilever with a constant cross section can be calculated by

$$k = \frac{EWH^3}{4L^3} \tag{2.23}$$

with the Young's modulus E, width W, length L and height H of the beam. Formula 2.23 can only be used for rectangular cantilevers. The calculation for other forms is proposed in literature [84]. For vibrational modes the form of the cantilever is as important as the resonance frequency. The form of a cantilever normalized to 1 with one clamped and one free side is given by [85]

$$h_n(x) = \frac{(-1)^n}{2}\left[\cos\kappa_n x - \cosh\kappa_n x - \frac{\cos\kappa_n + \cosh\kappa_n}{\sin\kappa_n + \sinh\kappa_n}(\sin\kappa_n x - \sinh\kappa_n x)\right] \tag{2.24}$$

with the mode number n and the wavenumbers κ_n, which are the solution of the equation $\cosh\kappa_n \cos\kappa_n = -1$

$$\kappa_n \approx 1.875,\ 4.694,\ 7.855,\ \pi(n-0.5) \qquad \text{for} \quad n = 1,2,3,\geq 4. \tag{2.25}$$

It is important to note that the deformation of a cantilever is different for a dynamic oscillation and for a static force acting at the tip. Since the calibration of the cantilever is done in a static mode with a force distance curve, it is not possible to directly use the fitted calibration factor to convert the sensor signal in the amplitude of the tip. For a classical beam deflection readout literature proposes a correction of 9 % [86]. The frequency of the modes can be calculated by

$$f_n = \frac{1}{2\pi}\kappa_n^2 \frac{H}{L^2}\sqrt{\frac{E}{12\rho}} \tag{2.26}$$

with the length L of the beam, the elastic modulus E, the density ρ and the height H of the beam. When the cantilever is driven at its resonance frequency, energy is stored in the oscillation. The quotient $Q_0 = \frac{2\pi E_0}{\Delta E}$ is called the quality factor; E_0 is the stored vibrational energy and ΔE is the total energy loss per vibration cycle, which equals the added energy when the oscillation is in steady state. The loss, and with it the quality factor, mainly depends on clamping loss, thermoe-

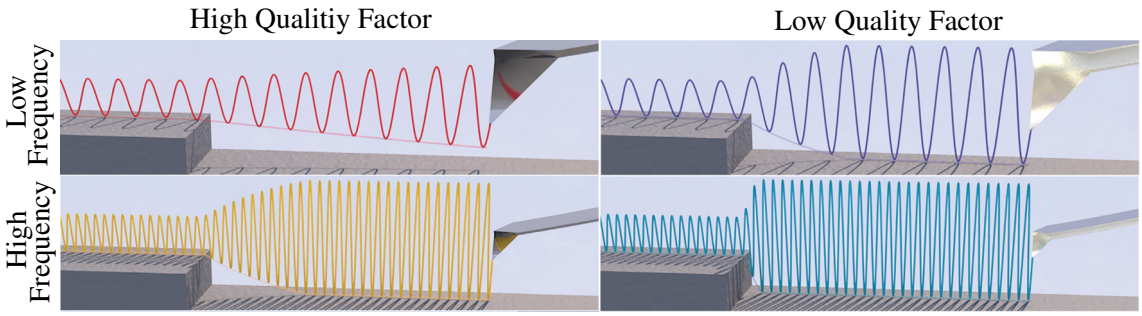

Figure 2.12: Scheme of the behavior of a cantilever in dynamic mode on a topography with a step. The higher the resonance frequency and the lower the quality factor, the faster the cantilever settles to the new state. Adopted from [87].

lastic dissipation, bulk internal friction and other surface effects [88]. For polymer cantilevers, the dominant source of damping is the thermoelastic dissipation which results in a quality factor more than one order of magnitude lower than when using silicon or silicon nitride [87]. The quality factor in combination with the resonance frequency has significant influence on the scanning speed of the AFM since the sensitivity is limited by the 3 dB roll-off at the frequency $f_{3dB} = \frac{\omega_0}{2Q}$ [89]. The situation for all combinations of high/low resonance frequencies and high/low quality factors are depicted in figure 2.12.

2.2 Optical Scanning Near-Field Microscopy

Besides the physical properties that can be gathered with AFM, laterally resolved optical information is also of interest for research and industry. With this information, the mode field of lasers or fibers can be calculated or in biology, the light of fluorescent tracers can be tracked [90]. The resolution of the far-field is limited due to the Rayleigh diffraction limit

$$d = 0.61\frac{\lambda_0}{\mathrm{NA}} = 0.61\frac{\lambda_0}{n\sin\alpha} \tag{2.27}$$

with the minimum resolution d, the vacuum wavelengths λ_0 and the numerical aperture NA with the refractive index n of the medium between sample and objective ($n = 1$ for air to $n = 1.52$ for immersion oil [91]) and the maximal half-angle of the light cone accepted by the objective α. However, this limit is only present when using the far-field of an object. In the near-field, exponential decaying waves exist, which are not resolution limited. The origin of those waves can be calculated by rewriting the dispersion relation, which is the solution of the Helmholtz equation

$$k_z = \sqrt{(\omega^2/c^2) - (k_x^2 + k_y^2)} \tag{2.28}$$

with k_x,k_y,k_z being the components of the wave vector $\vec{k}$, the angular frequency ω of the light as well as the vacuum speed of light c, when the second part under the square root becomes larger than the first part, which results in a negative radicand. This happens especially for transitions

from higher n_1 to a lower refractive index n_2 for supercritical internal reflections with an angle above the critical angle $\sin\theta_c = \frac{n_2}{n_1}$. The solution then is in the form of

$$E(r,t) = \mathrm{Re}\left[E_0 e^{(\pm i(k_x x + k_y y))} - i\omega t)\right] e^{(\mp |k_z| z)} \tag{2.29}$$

which results in evanescent waves near the surface. Those waves can be measured by guiding them from the surface, either by a metal tip on which plasmons can oscillate and stimulate light emission (the so called scattering SNOM) or by tips with aperture. These tips are produced by a manual pulling process, where metal coated fibers are thinned by a melting or etching process [92]. It is important to note that with the immersion of the tip into the evanescent waves, an interaction occurs that can change the evanescent waves, which results in artifacts [93, p. 122].

2.2.1 Theory of Operation

For a SNOM measurement the tip has to be kept a few nanometers above the surface, while the sample is scanned under the tip with a scanner similar to the AFM. A classical SNOM setup consists of a tuning fork, with the fiber glued on one prong so, that the fiber is parallel to it. A phase-locked-loop control system actuates the tuning fork at its resonance frequency. Then, the

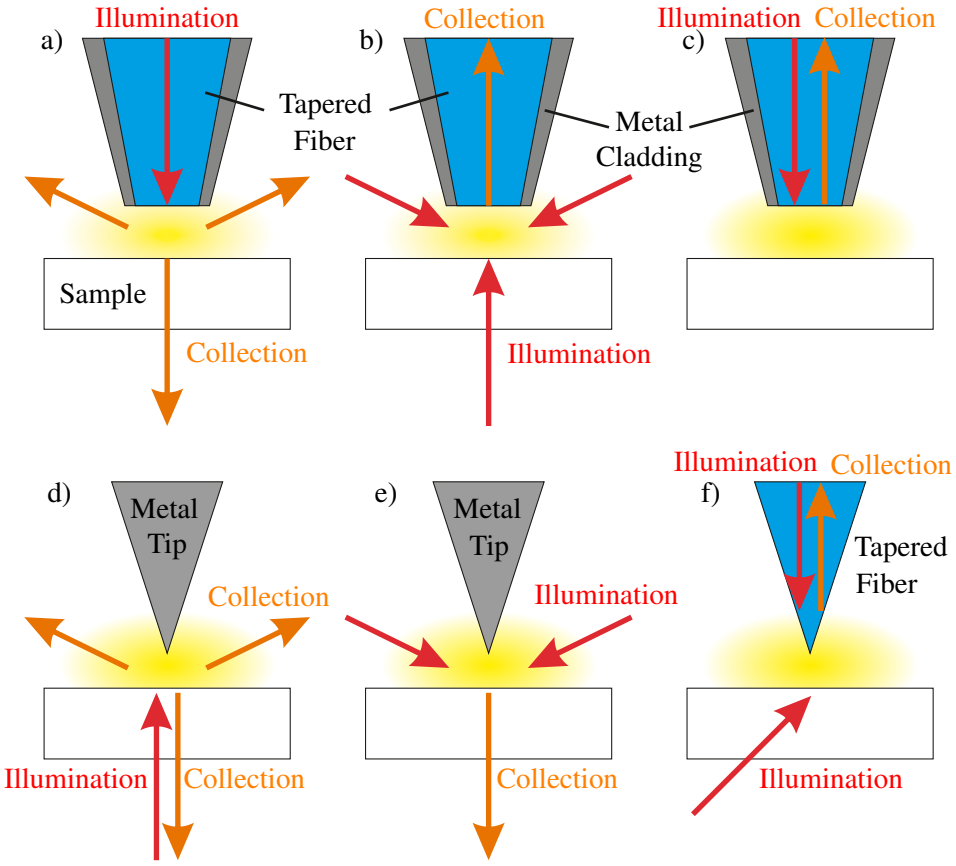

Figure 2.13: **a)-c)** Various SNOM configurations for aperture probes and **d)-f)** apertureless probes used for scattering SNOM with different illumination schemes. Adopted from [22].

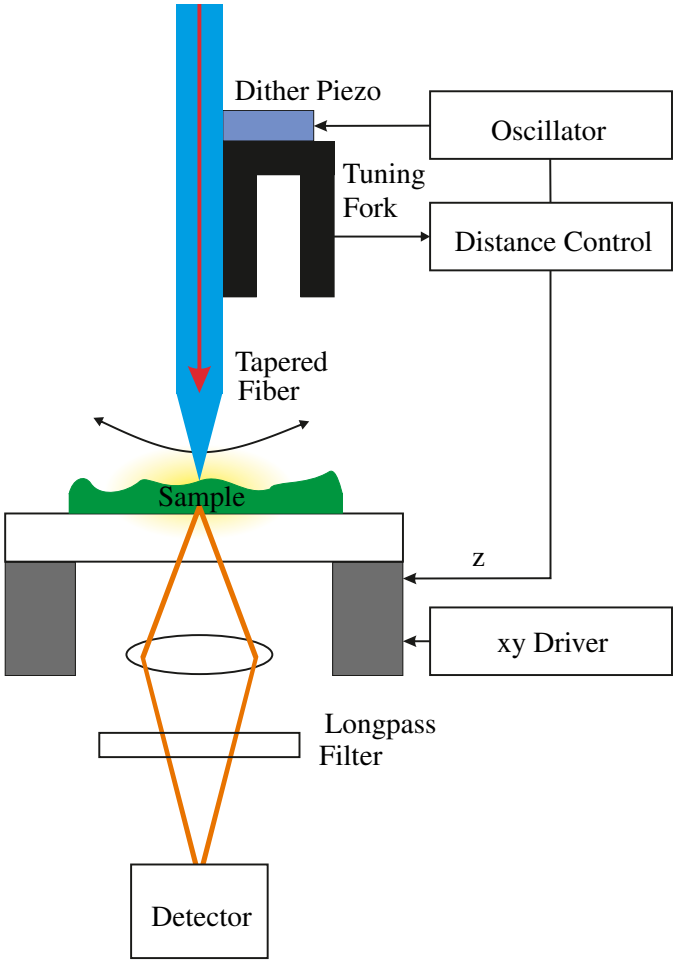

Figure 2.14: Schematic of a complete SNOM setup. The fiber oscillates vertically above the sample via a tuning fork and the changing resonance frequency is used as topography feedback. The sample is scanned under the tip to obtain the topography and the optical signal space-resolved. Adopted from [22].

tip is approached to the surface. When the tip is in small distance to the surface, forces act on it, which results in a change of the resonance frequency just as in the tapping mode in section 2.1.3, but here the tip does not oscillate vertically, it oscillates laterally to the sample surface, which makes a feedback more complicated. This mode is called 'shear force mode' and is typically used for aperture probes. Optical resolutions in the sub-20 nm range have been reported [94]. For the feedback it is also possible to employ a quartz tuning fork [95] which immediately delivers a sensor signal. Another approach is also presented in literature where a configuration similar to tapping mode was used. The fiber was glued on a big tapping cantilever which was driven by a piezo actuator [96]. Due to its size, the resonance frequency was in the range of 5 kHz only, which inherently limits the bandwidth.

Another approach than aperture probes is to use metal coated tips. The setup is similar to a non-contact AFM setup, but also includes macroscopic optics for illumination and collection of the stray light. Here, with the help of an interferometer, the modulation of the phase signal caused by the sample tip interaction is measured and results in a resolution of 10 Å [97]. Most setups so far have in common the use of macroscopic optics and limitations in sample properties. Since

the tuning fork for aperture SNOM or the AFM head with its laser for apertureless SNOM are bulky and typically completely cover the sample from above, it is only possible to illuminate the sample from below. This means that the sample has to be at least semitransparent. The same applies when the tip is used for illumination and the stray light has to be collected from underneath. As a third method it is possible to illuminate and collect the light through the same aperture. But due to the high coupling loss this is only suitable for tip-sample distances smaller than 5 nm [98]. More exotic setups illuminate from all sides [99].

2.3 Two-Photon Polymerization Lithography

In the last few decades, atomic force microscopy nearly exclusively utilized silicon or silicon nitride cantilevers which were etched out of a wafer. This results in little customization possibilities and high variances. 3D printing however, offers high precision and vast customization options. Moreover, 3D printing is able to fabricate the desired structure on the target area with submicrometer precision. This prevents the necessity of adjustments after production. The so produced cantilevers can be used directly.

2.3.1 Overview

With the help of two-photon polymerization (TPP) it is possible to polymerize a resist with photons having only half of the energy normally needed to crosslink the polymer. In linear absorption the absorbed photon matches the energy between the occupied ground state S_0 and a higher energy state S_1 whereas in non-linear absorption of TPP two photons are needed to lift the electron with the help of the short-term existing virtual state S_i to the higher state S_1. Due to the short lifetime of approximately 1 fs [100, ch. 1.3] of the interstate S_i, it is necessary to have a high density of photons in the area. This is the key to be able to only develop the resist at the point of interest since outside the focus the density of photons is too low, which makes it possible to illuminate through the remaining resist without developing it. The reaction speed of the TPP is proportional to the square root of the photon density. The point-spread function of the photopolymerization is the square of that for single-photon polymerization [101]. This means that the voxel of the TPP has almost the same diffraction limited lateral size of the voxel produced by single-photon polymerization with half the wavelength of the TPP and a smaller longitudinal extent [102]. The form of a voxel is schematically depicted in figure 2.15 and has a higher expansion in z-direction than in lateral direction. To reach a high density, the laser has to be focused with an objective with a high numerical aperture and a pulsed laser has to be used. In the Nanoscribe Photonic Professional GT a femtosecond pulse laser is applied. The intensity can be calculated by

$$I_{Laser} = \frac{P_{Laser}}{A} = \frac{N_{ph} \cdot E_{ph}}{\Delta t \cdot A} \tag{2.30}$$

with laser power $P_{Laser} = \frac{E_{Laser}}{\Delta t}$, the pulse width Δt, the laser energy $E_{Laser} = N_{ph} \cdot E_{ph}$, the number N_{ph} of photons per pulse, the photon energy E_{ph} and the illumination area A. In these formulas, the reason for the use of a femtosecond laser can be found. For very short pulses, the density of photons in this time is way above the density of a continuous laser. The Nanoscribe GT contains a frequency doubled pulsed laser with an emission wavelength of 775 nm. The used resist IP-Dip is transparent for this wavelength, but is absorbing in the ultra-violet regime ($\lambda = \Lambda_0/2 = 388$ nm). The chemical reaction inside the resist can be schematically explained by

Initiation

$$\mathrm{I} \xrightarrow{2\hbar\omega} 2\,\dot{\mathrm{R}} \qquad \text{I: Initiator} \qquad \{1\}$$

$$\dot{\mathrm{R}} + \mathrm{M} \longrightarrow \mathrm{R} - \mathrm{M}\bullet \qquad \text{R: Radical} \qquad \{2\}$$

Propagation

$$\mathrm{R} - \mathrm{M}\bullet + \mathrm{M} \longrightarrow \mathrm{R} - \mathrm{M} - \mathrm{M}\bullet \qquad \text{M: Monomer} \qquad \{3\}$$

Termination

$$2\,\mathrm{R} - \mathrm{P}\bullet \longrightarrow \mathrm{R} - \mathrm{P} - \mathrm{P} - \mathrm{R} \qquad \text{P: Polymer} \qquad \{4\}$$

The resist consists of at least two materials: monomers and an initiator. The initiator is activated by two photons and splits into two radicals. The radicals cut the double bonds of the carbons of the monomers and oligomers, which then in turn creates new radicals at the end of the monomers and oligomers. This reactions becomes a chain reaction and can lead to large cross linked polymers. A termination reaction occurs when two activated polymers react with each other. An additive is added to index-match the used resist IP-Dip so that it can be used as immersion fluid [103].

2.3.2 Printing Setup

The printing setup is depicted in figure 2.15. For writing in all three dimensions the model is sliced into small layers with heights in the range of 50 nm to 300 nm. To write this layer, the laser is reflected by two galvo mirrors, one for x- and one for y-direction. With these mirrors, the laser can be moved through the objective over the whole visible area. Additionally, the laser can be switched on and off to be able to write parts of the layer which do not touch each other. To write the next layer, the whole sample is moved in z-direction. With this technique it is possible to write arbitrary forms as long as the higher layer has enough contact to the layer underneath. Effects like shrinking of the developed resist theoretically further improve the resolution but also lead to problems like upbending, which is investigated in chapter 5.1.5. The size and resolution of the structure depends on the magnification of the objective and the wavelength. In this work, an objective with a magnification of 40X and a numerical aperture (NA) of 1.4 is used, as well as

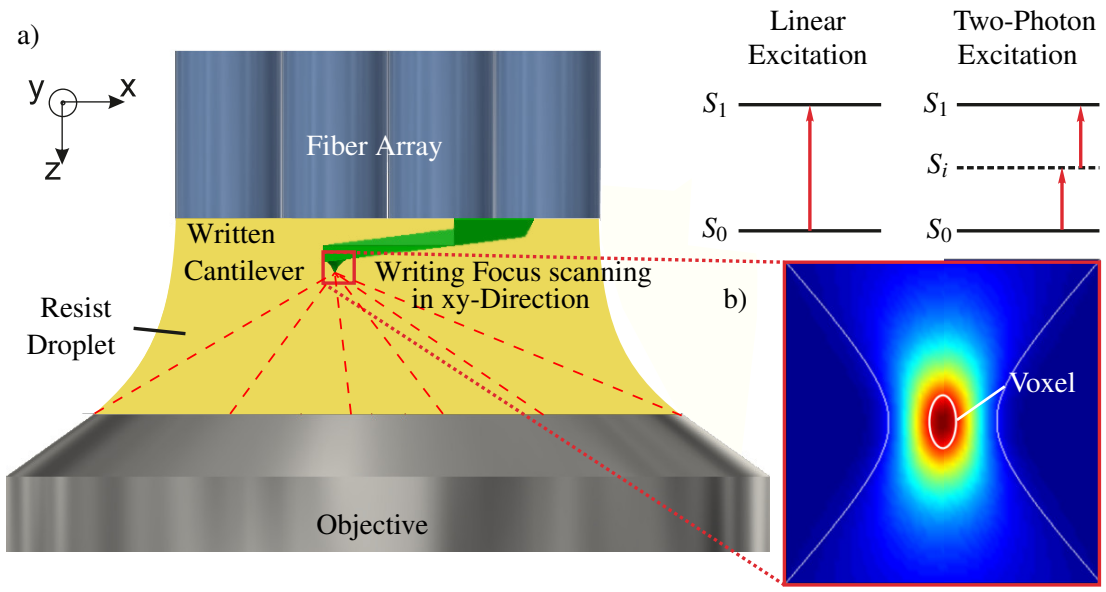

Figure 2.15: **a)** Schematic drawing of the writing process. The objective is covered with resist which also acts as immersion liquid to increase resolution. The laser is focused and the area on which the power is high enough to allow two-photon polymerization is marked, which results in a written voxel schematically depicted in **b)**. Adopted from [22].

an objective with a magnification of 63X and an NA of 1.4. It is possible to write objects bigger than the lens coverage by stitching.

3 3D Printed Polymer Tips

3.1 Introduction

In recent times 3D printing became a versatile tool for rapid prototyping. This chapter presents a new application for 3D printing.
To investigate a fine-structured sample with regard to topography and mechanical properties, the method of choice is typically atomic force microscopy (AFM). Besides its wide popularity in material science and its easy accessibility for researchers, the AFM itself offers multiple approaches to investigate sample surfaces.
Dependent of the sample structure and AFM mode, the proper cantilever has to be selected. Despite major criteria like spring constant and resonance frequency, the performance of an AFM depends on the size, shape and composition of the probing tip [104, 105].

Whereas the tip radius itself is the limiting factor for lateral resolution, the overall shape of the tip is also important [106]. To measure deep trenches or high aspect ratio features, the width and the height of the tip are of high importance. Some more specific tasks, like surface structures on sidewalls, require even more advanced tip designs [107].

Various fabrication methods and materials such as diamond [108], carbon [109], polymers and metals [110] have been introduced to obtain different functionalities. Kim and Maramatsu have presented polymer tips in order to obtain hydrophobic tips [111, 112]. Tip sizes down to 100 nm have been reported, as well as tips with reduced adhesion forces. This radius is already good to measure samples with scan sizes in the range of multiple micrometers, because it is not possible to resolve lateral features smaller than 100 nm due to the convolution of tip radius with a sample feature. Jung *et al.* [113] have decreased the radius by subsequently O_2-plasma ashing the tip down to 15 nm. Lee *et al.* [114] have attached hydrogel probes by using mold inserts.

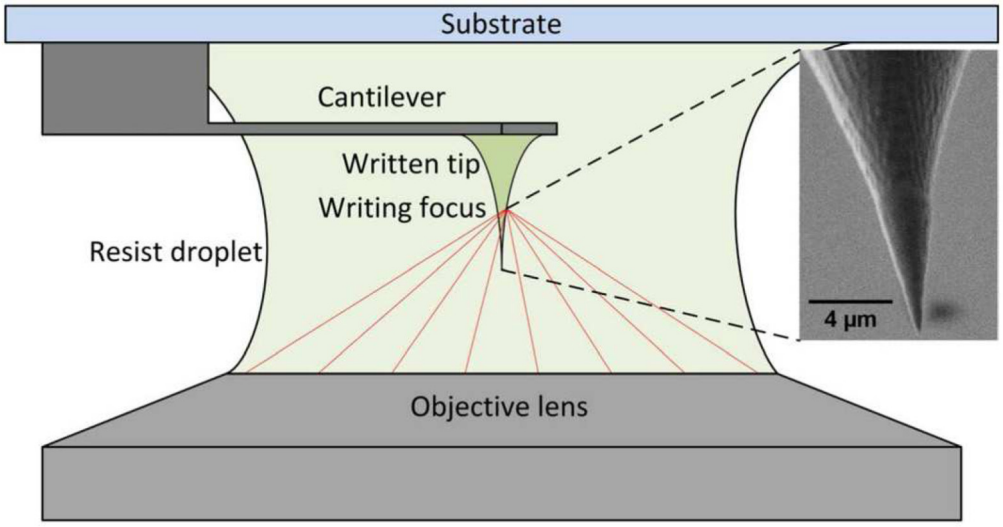

Figure 3.1: Schematic drawing of the 3D printing process. A tipless cantilever is fixed on a substrate. The objective focuses the infrared laser within the resist, which also serves as immersion-medium. Adopted from [115].

3.2 Proof of Concept

For the written tips, a commercial 3D printer is utilized (Photonic Professional GT, Nanoscribe GmbH) and as resist the Nanoscribe IP-Dip. The resist is an ultraviolet light curable resist, which is exposed to a tightly focused infrared femto-second light source. To fabricate the tip, a tipless cantilever is mounted on a substrate and immersed in resist. The laser beam is directed in the lateral direction with galvo mirrors to expose a layer of the tip. After the layer is finished, the focus is brought to the next layer and scanned again. Those steps are repeated until a sharp tip is completed on the cantilever.

In figure 3.1 the writing process is depicted. As objective a 63x, NA=1.4 was used. The writing speed was chosen to be 20 mm/s and the slicing and hatching distance for the layers was set to 100 nm. In order to obtain a tip that is as sharp as possible, the last 5 µm of it were sliced in 50 nm layers and the writing speed was reduced to 1 mm/s. The SEM inset in figure 3.1 shows a clear transition between both stages.

To test the cantilever with the polymer tip, a home build 800 µm scan range AFM was used, which consists of a commercial controller (ARC2, Asylum Research) and related software as well as a 800 µm piezo stage for lateral scanning, which also hosts a 30 µm z-piezo.

To test the performance of the tip, the two most common AFM modes, contact mode and intermittent contact mode, were used. Both modes are further discussed in section 2.1.

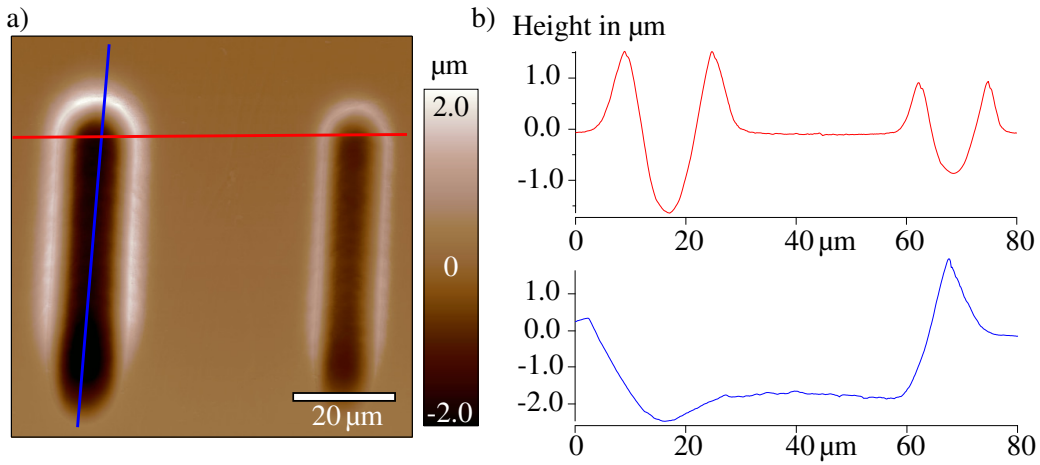

Figure 3.2: **a)** Measured topography of two trenches produced with different forces applied. **b)** Cross sections of the topography of one trench in x- and y-direction.

3.2.1 Polymer Tip in Contact Mode

In contact mode not only the vertical forces acting at the tip are high, but also the lateral ones. Here, the cantilever tip is sliding along the surface. To reduce damage on the tip, a cantilever with a significantly lower spring constant than for intermittent contact mode was chosen. A tipless V-shape cantilever with low spring constant ($< 0.1\,\mathrm{N/m}$) was selected and a polymer tip was added. As sample a soft material was used onto which trenches were scraped in with different forces; this is presented in figure 3.2. This was a pretest for very deep trenches on which normal cantilevers with tip lengths in the range of 10 µm cannot touch the surface at the bottom since they are too short. Both trenches were resolved well and no artifacts were visible. To further investigate the polymer tips, a new measurement was performed with an additional test grid.

The TGT1 test grid (NT-MDT), which consists of an etched array of sharp silicon tips was also measured in contact mode. When measuring with typical forces in the range of 5 nN to 100 nN, the topographical images were identical to the one in section 3.2.2 acquired in tapping mode. But with increasing forces, the sharp tips of the TGT1 grid became misshaped. In figure 3.3 the measured topography with an applied force of $340\,\mathrm{nN} \pm 10\%$ is depicted on the left side. To highlight the artifact, on the right side an additional image is shown. In this image, the data is divided into two groups, one with topographical values equal or smaller than 470 nm, which are displayed white and one group with values higher than 470 nm. If the data points are presented in this way, they reveal a clear 'double-tip'. Considering the fast scan direction, this can be explained by a slipping of the polymer tip around the silicon tips of the grating. This effect only occurs when measuring high features with large forces in contact mode. Even if this is not a typical experimental setup, this should be kept in mind to be able to recognize and interpret artifacts.

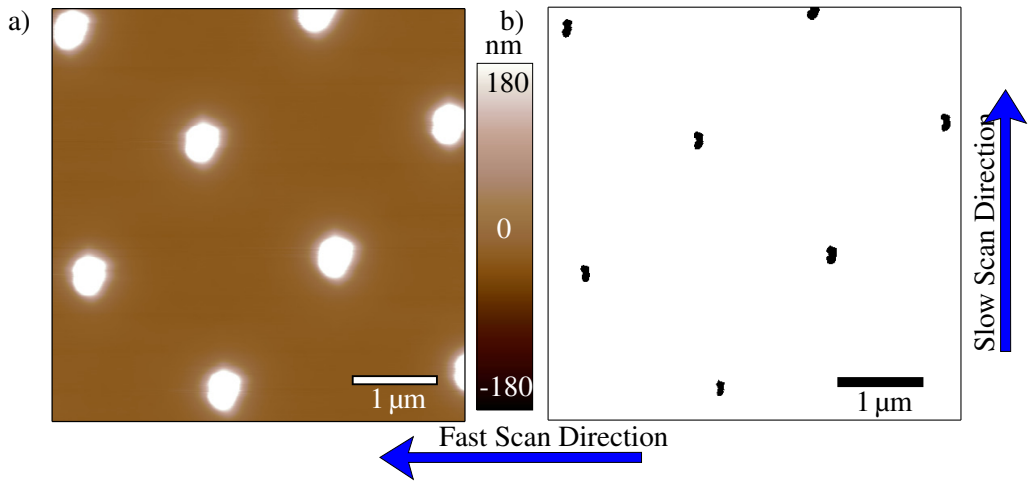

Figure 3.3: **a)** Topographical image of the TGT1 grid measured without artifacts in contact mode. **b)** Vertically cropped image of a measurement with high loading force. If a data point is higher than 470 nm it is represented in black, otherwise in white. A deformation of the tip is visible.

3.2.2 Polymer Tip in Intermittent Contact Mode

The forces between the tip and the sample are 50 to 500 times smaller in intermittent mode [116]. Since this is one of the most common modes, further tests were performed in this mode.

Although the resist has a Young's modulus of 2.34 GPa and thus should be sufficient for imaging, there existed only little experience [111] with the behavior of such a tip.

As a test, two well defined test samples were measured. For general performance a standard calibration grating with 10 µm pitch, 200 nm depth and a structure size of 5 µm was used (Digital Instruments P/N 498-000-026). To determine the tip radius, the TGT1 grating from NT-MDT was surveyed.

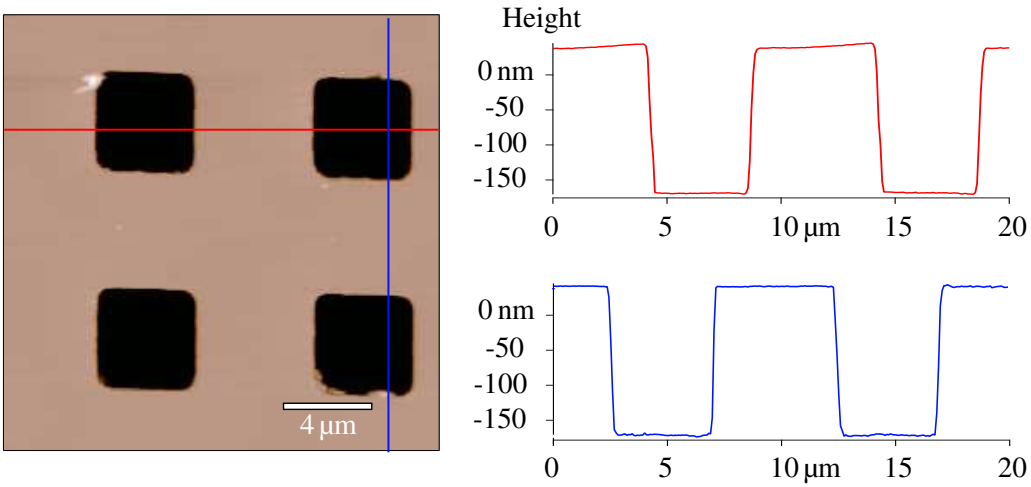

Figure 3.4: Topography and cross section of the Digital Instruments grating. Steep edges are visible.

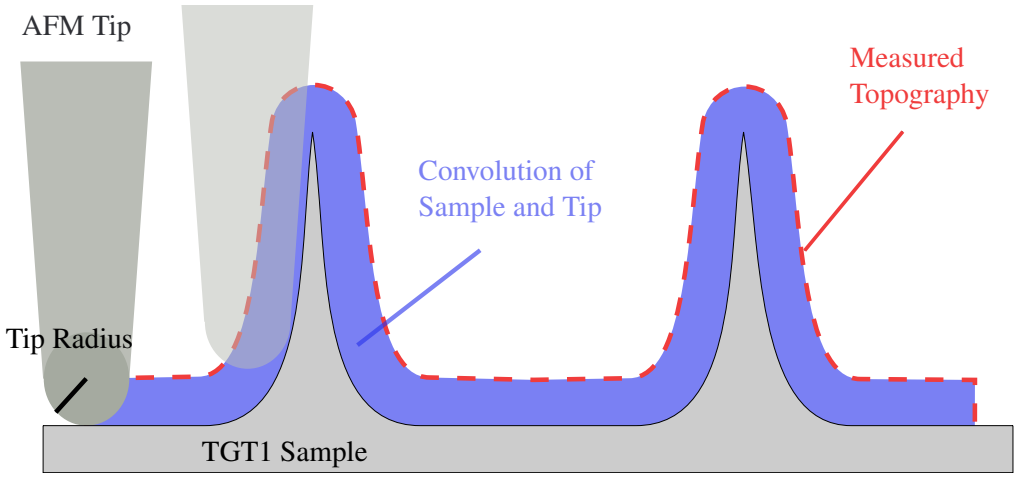

Figure 3.5: Schematic of the convolution of the tip and sample. When the sample features are smaller than the tip, the shape of the tip becomes the dominant shape in the measured topography.

Steep patterns are generally good for calibration and measuring some effects like overshoots in the control loop. Since the pattern is well defined, any conspicuities caused by the polymer tip can be detected.

Figure 3.4 shows the obtained topography as well as two orthogonal, lateral cross sections. The cross sections shows no additional artifacts like sloped edges or other unwanted effects. The size and form of the tip is no problem for such big structures.

3.3 Sharpness of the Tip

The tip radius is important for small featured samples. The grating used is densely covered with an array of sharp silicon tips with radii smaller than 10 nm. These tips have a smaller tip radius than the written polymer tips, thus the obtained topography gives information about the form and size of the polymer tip due to the higher contribution of the polymer tip to the measured topography. In figure 3.5 this convolution process is depicted.

The surveyed topography is the convolution of the sample and the tip. This means, that the topography is dominated by the largest shape of the tip-sample interaction. A large, blunt tip will always give a blunt topography even if the specimen has small, sharp-edged features. A schematic of the measurement process is shown in figure 3.5. An example for such a kind of convolution is a so called 'double-tip' artifact [117]. By scanning with a tip with a deformation or a dirt particle, which essentially forms a second contact zone with the sample, the measured topography will appear as an image which contains additions to the topography looking like the same image with a small lateral shift [118].

As shown in figure 3.6, none of those unwanted effects are visible. Only a pattern of sharp spikes is depicted. This means that the data from the measurement can be taken to determine the tip radius and shape.

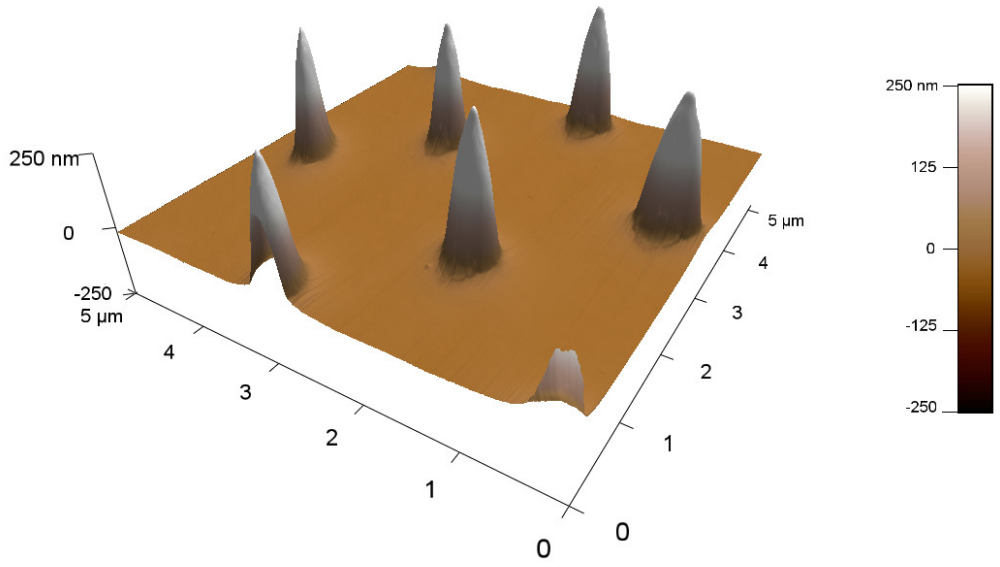

Figure 3.6: Topography of the TGT1 grating (NT-MDT) measured in tapping mode with a polymer tip. The shape of the measured tip apex is similar to the polymer tip apex due to convolution.

The deconvolution of the obtained topography and thus the radius of the polymer tip is calculated with the deconvolution software Deconvo2 (NT-MDT). This led to a radius smaller than 25 nm. This technique can further be used to survey the size and shape of a voxel written by two-photon polymerization.

Figure 3.7 shows the cross section of the calculated tip.

The tips of the TGT1 grating are specified with radii of smaller than 10 nm. The used software Deconvo2 does not know about this specification of the grating. Basically, the software looks for the finest resolution in the image for every direction. It is also possible to scan over small nano-particles with sharp edges. This means, that the smallest possible calculated tip size will be in the range of the 10 nm of the tips of the TGT1 grating. This would be the case for a δ-peak-like tip, an infinitesimal small tip. Since the tip has a non-zero size, a value larger than 10 nm is expected.

The software Deconvo2 plots a two dimensional image of the calculated tip. Figure 3.7 shows the topographical information as a heat map as well as a cross section. In the cross section a circle with a radius of 25 nm is plotted. The curvature of the tip and the circle match excellently. As already mentioned, this means a tip radius smaller than 25 nm is realized since the measured tip is a convolution of the topography of the TGT1 grid and the tip.

3.4 Tips on Self-Sensing Cantilevers

Whereas it is possible to buy common cantilevers with tips, most self-sensing cantilevers based on piezoelectric [7], piezo resistive [8, 9] or tunnel magnetoresistive (TMR) [119, 120] sensors

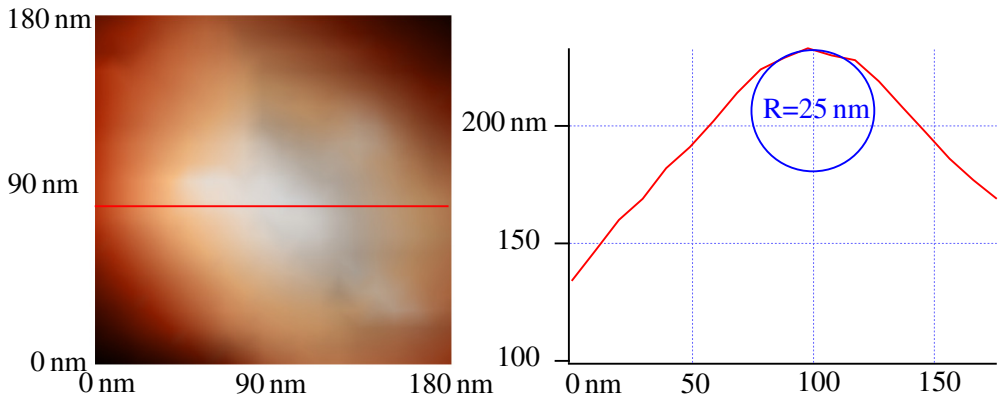

Figure 3.7: Topographical structure of the polymer tip used to scan the TGT1 grating (NT-MDT) processed with the software Deconvo2 (NT-MDT). In the cross section a circle with a radius of 25 nm is plotted.

do not provide a tip since this would add extra steps in the etching process. To overcome this problem, a typical solution is to manually glue a sphere with a diameter in the range of 5 µm to the end of the cantilever [121]. Self-sensing cantilevers are mostly time-intensively fabricated individual items. For unskilled people it is quite difficult to attach a sphere with a diameter of 5 µm to the end of a cantilever with widths typically smaller than 50 µm, so this process does not provide a high yield. Furthermore, a sphere in this size is not an ideal tip. The topography obtained is a convolution of the tip and the sample. A steep edge thus is imaged as round edge with a radius of 2.5 µm, which is only suitable for large images.

As example, a self-sensing TMR-cantilever was equipped with a copper sphere with a diameter of 5 µm. With this tip, a carbon fiber sample ('SThM Test Sample', Bruker) was measured in multifrequency dynamic mode (see chapter 2.1.3). The sample consists of carbon fibers embedded in epoxy. This composite was cleaved and polished to have a flat surface consisting of two different materials. As scan size 100 µm were chosen, which is the typical upper limit of commercial AFMs. In multifrequency mode the cantilever is simultaneously driven at the first and a higher harmonic. The first harmonic is used for the topographical feedback whereas the higher harmonic is driven at a smaller amplitude and thus more sensitive to force gradients [77, 78, 122]. The measurement is depicted in figure 3.8. The topography shows a relatively flat image but it is possible to distinguish between both materials due to their different abrasion when polishing. At the first harmonic, the amplitude is used as feedback, so for an ideal control loop this signal would be at the chosen setpoint for the cantilever amplitude. When the control loop is too slow, the amplitude differs from the setpoint and a variation in the amplitude always means an error. This is why this image is also called 'error image'. The phase in the first harmonic is effected by the energy dissipation from the cantilever to the sample [123]. This helps to distinguish between different materials. In figure 3.8 it is already possible to spot the circular fibers with a diameter of around 6 µm.

The second harmonic frequency is driven with a constant amplitude at the shake piezo and the cantilever deflection signal is recorded. Since there is no control loop, also the amplitude changes

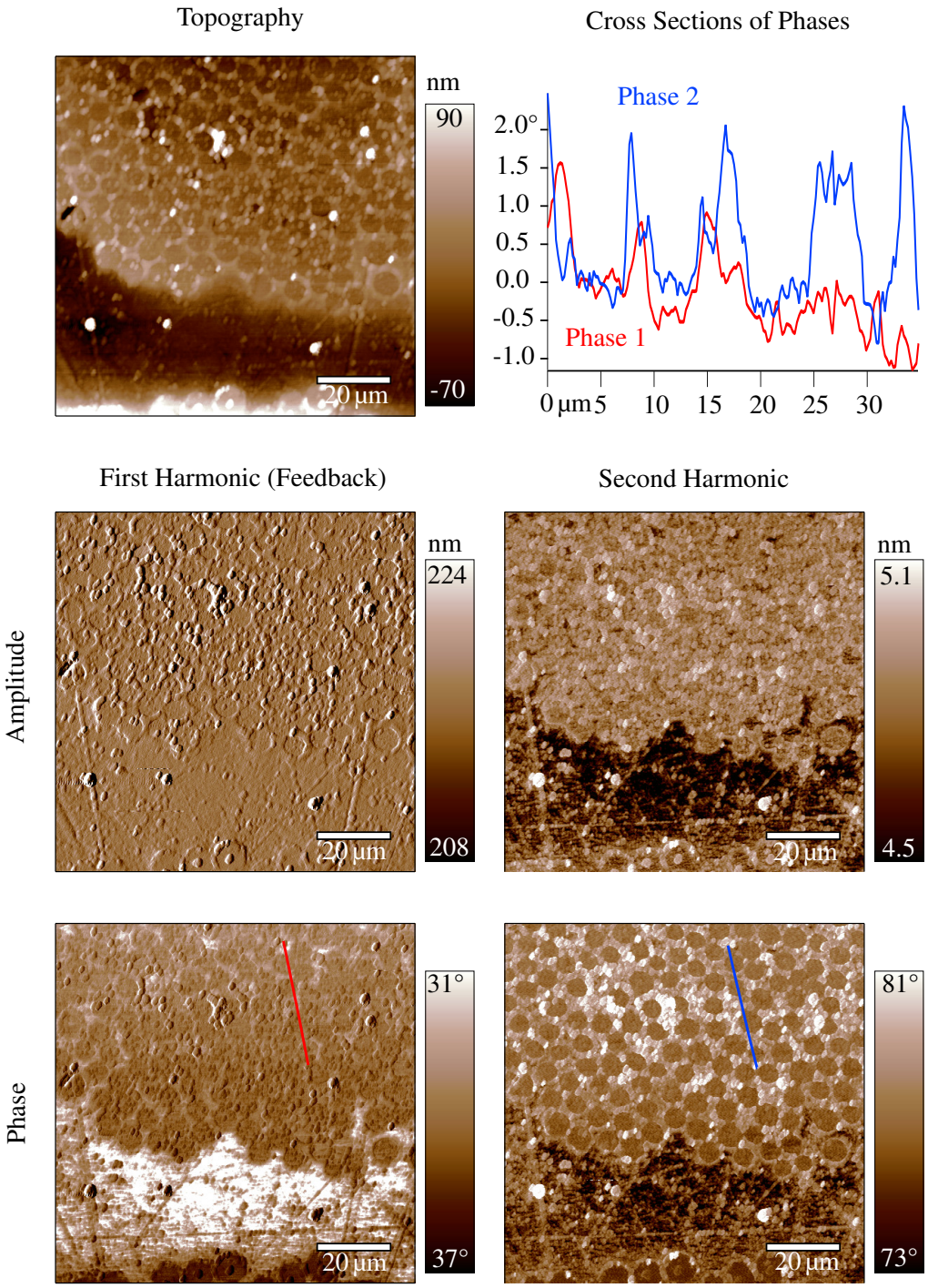

Figure 3.8: AFM images of carbon fibers embedded in epoxy obtained with a self-sensing TMR-sensor in multifrequency mode. Left images are obtained with the first harmonic of the cantilever, which was used for the feedback. The oscillation of the higher harmonic driven with a piezo with fixed AC-voltage was recorded. On the top right a cross section of the first and second harmonic phase (marked red and blue in the phase images) is shown. The higher harmonic phase reveals higher contrast. This images were recorded with a copper sphere as tip with a diameter of 5 µm. This large tip radius leaves circle-like structures well observable in the second harmonic and at the dirt particles in the topography.

with the energy dissipation due to different materials. This is why this image has more similarities to a phase image than the amplitude image of the first harmonic.

Although a big scan size was set, it is possible to spot circle-like structures, especially in the second harmonic. The dirt particles in the topography show the same effect. This results from the convolution of the spherical tip and the sample.

Measuring small features on samples requires more effort than just manually attaching a sphere on the cantilever. One solution is to add a tip by focused ion beam deposition [119]. This gives small, hard tips in the range of 25 nm [124] but is only practicable for individual cantilevers or leads to a high-cost manufacturing process [125]. Here too, polymer tips written with two photon absorption provide a fast and easy solution. The Nanoscribe machine can be used without any tuning. To show the improvement of a polymer tip over a copper sphere, a similar TMR-sensor used for measuring figure 3.8 was outfitted with a 3D printed polymer tip. For the writing process of the tip for the TMR-cantilever, the fully etched wafer, containing 128 sensors, was mounted onto the Nanoscribe machine. The writing process itself took only about 1.5 min for one tip as presented in section 3.7. After cleaning the wafer, the TMR-cantilever was ready for measuring.

In figure 3.9 a lymphocyte was measured with the same multifrequency mode as in figure 3.8. The lymphocyte offers a good opportunity to show the fine resolution of the tips, since it has a size of about 7 µm [126], but as a biological cell it has structures down to the nanometer range. The scan range of the image was 11 µm. The lymphocyte has a high topography up to 1 µm which means that it is not possible to show fine topographical effects in the topography image, which results in a blurry appearing image. Here again, the amplitude of the first harmonic is the error image whereas the phase images and the amplitude of the second harmonic reveal material contrast. In figure 3.9 a zoom image of the phase of the second harmonic is provided. A circle marks a distinct filament with a size in the range of 40 nm. Actually a shift from line to line is noticeable, which indicates that the lower scan size limit of the 800 µm-stage is reached.

3.5 Long-Term Stability of Polymer Tips

It is plausible to suspect that polymer tips cannot withstand the tip-sample forces for a long time since polymer is much softer than conventional silicon tips.

To test the long-term reliability of the tip in the harsher contact mode, a measurement process was developed. In order to get the tip radius over time it was necessary to mix contact- and intermittent contact mode. The intermittent mode gives better resolution for the tips because in contact mode the higher forces lead to small shifts when the polymer tip and the tip from the grating are pressed together. This results in a blunter measurement than in intermittent contact mode.

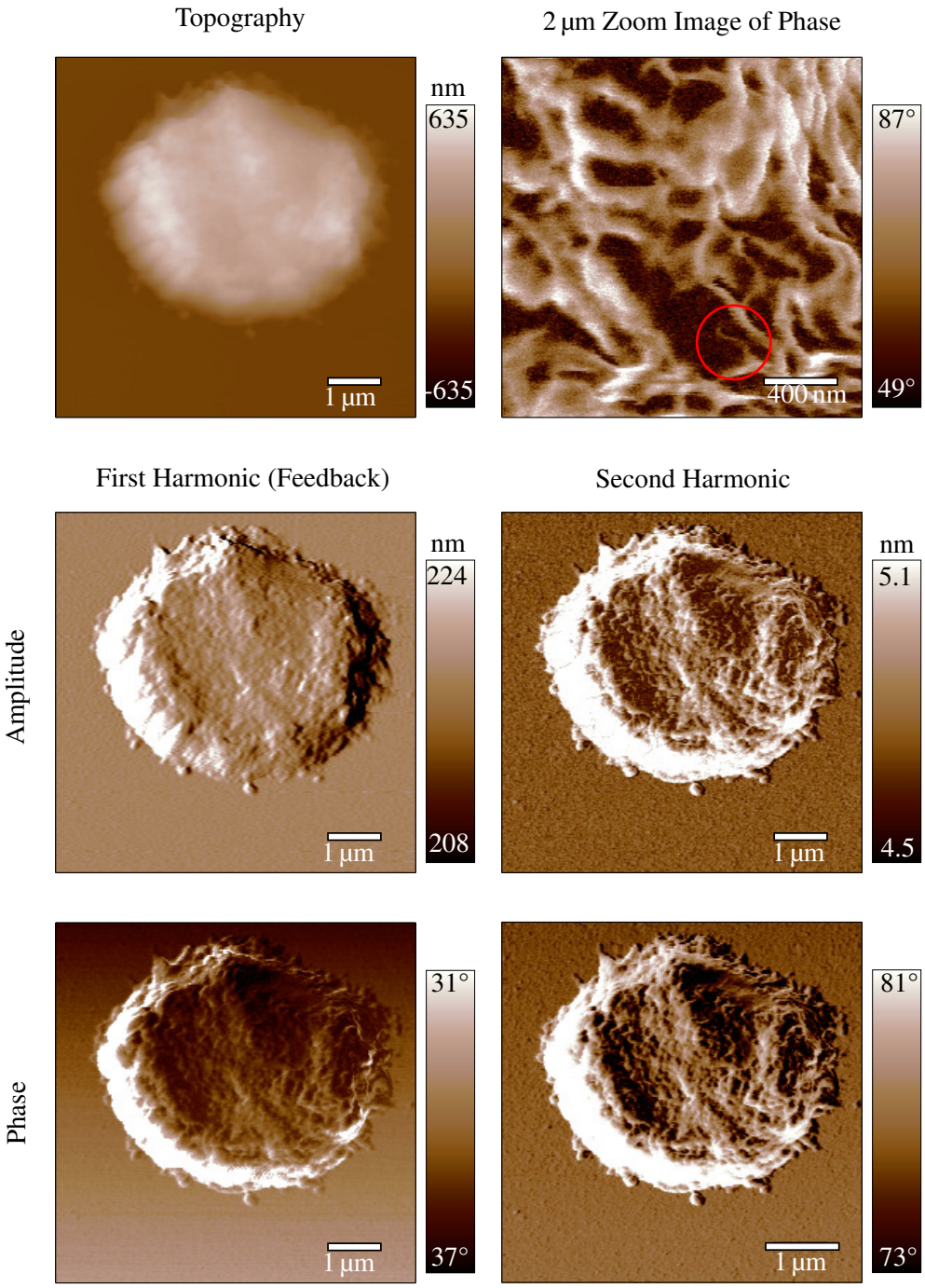

Figure 3.9: Multifrequency mode AFM image of a lymphocyte. The left images were obtained with the first harmonic with the feedback on the amplitude. The second harmonic reveals higher contrast of the structure of the cell membrane. The zoom image of the phase of the second harmonic on top right reveals fine structures with a diameter in the range of 40 nm.

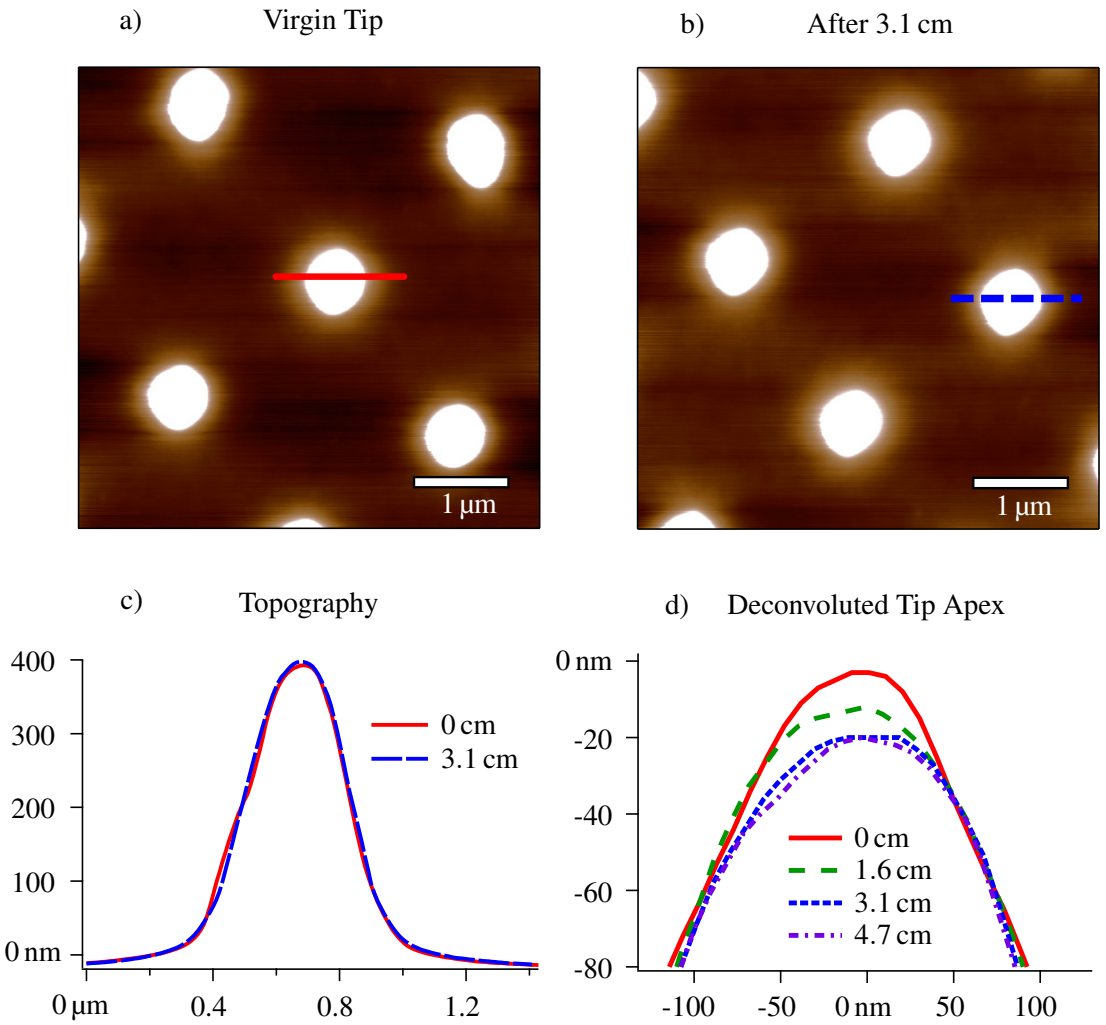

Figure 3.10: Figure **a)** and **b)** show topographical images with a scan range of 5 µm of the TGT1 scanned with a polymer tip. Between those images the tip was scratched hard for 3.1 cm in contact mode. Figure **c)** depicts the two cross sections from **a)** and **b)** with no visible differences. Figure **d)** displays the tip apex after various scratching distances. Tip wear is noticeable, but in an acceptable range.

The common cantilevers for those modes differ in terms of spring constants and resonance frequencies. For contact mode, a soft cantilever with a spring constant smaller than 1 nN/nm is typical, whereas a spring constant of 10 nN/nm to 100 nN/nm is typical for intermittent contact mode.

To measure in both modes, a trade-off between both cantilever types had to be found. For this measurement the AFM probe All-In-One-Tipless (BudgetSensors) was used. It is equipped with four cantilevers, ranging from a soft contact cantilever (spring constant: 0.2 nN/nm, resonance frequency: 15 kHz) to a hard dynamic mode cantilever (spring constant: 40 nN/nm, resonance frequency 350 kHz). It also contains cantilevers used for soft tapping mode with spring constants of 1 nN/nm and resonance frequencies of 150 kHz.

With these cantilevers both modes are realizable, albeit not perfectly. The high spring constant allows to apply forces in the higher ranges than the typically used 5 nN to 500 nN [116] in contact

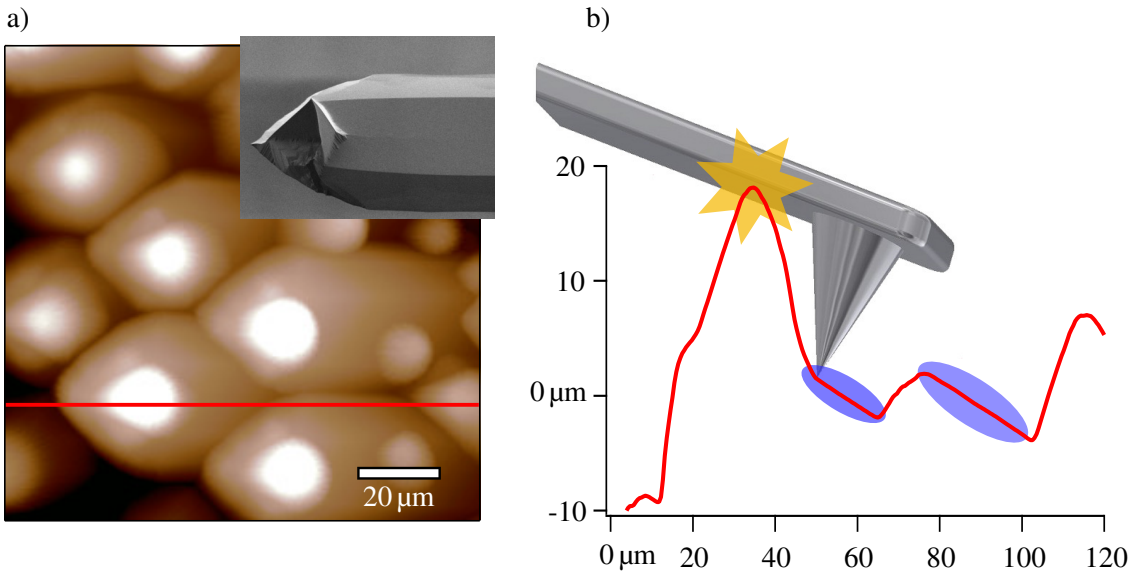

Figure 3.11: **a)** AFM image of a rose petal replica with a tip shorter than the structures of the rose. **b)** On the cross section the origin of the artifact is depicted. The protrusions scan the cantilever which induces an inverted imaging process, so that the topography of the cantilever is scanned. Those artifacts are marked blue in the cross section.

mode, wherein the upper range is not used for topographical imaging, but for lithography in soft material. This process can already start at 10 nN for thin layers [127].

After calibration of the spring constant and deflection of the cantilever with the method by Sader *et al.* [128, 129], a first intermittent contact mode image was recorded. After the inertial image, which was used to specify the unused tip, three additional images were recorded in contact mode. For those measurements forces of 66 nN $\pm$ 10% were chosen. As already stated, this is an untypically high loading force for topographical imaging. The scan size was chosen as 5 µm and as scan speed a tip velocity of 0.5 µm/s. Each scan consists of trace and retrace with 512 lines each. This setup results in an effective lateral scratch distance of 5.12 mm per image. After every third image a scan in dynamic mode was done. These scans are not added to the total scratch distance. After 4.6 cm of scratching in contact mode, a final image in dynamic mode was obtained.

The topography recorded with the unused tip and the topography gathered after 3.1 cm of scratching are optically identical. As proof, two cross sections of one silicon tip were chosen and superimposed. They match excellenttly, thus the abrasion is negligible for standard topographical measurements. To further investigate the abrasion of the tip, all four dynamic mode images were loaded into the Deconvo2 (NT-MDT) software and the shape of the tip was calculated. In figure 3.10 the tip apex is represented with its cross sections after each 1.55 cm of scratching. As expected, tip wear can be observed, but it is in an acceptable range, despite the high loading force.

3.6 Adapted Tips

In some cases, it is not even possible to buy cantilevers which suit the special requirements. When measuring samples with high aspect ratio, the probing tip also has to have this aspect ratio. On many biological surfaces, high wax structures are present. Often they are also optically active, due to their interaction with light. This disqualifies most optical investigation methods like white light interferometry. For the investigation of such structures, e.g. in rose petals, which can be used to improve solar cells [130], those adapted tips can be used to measure these high structures. In this example a replica of a rose petal is measured. The features of rose petals can reach heights of more than 20 µm, as shown in figure 3.12, which means that typical AFM tips with a length in the range of 10 µm to 16 µm are not suitable for the measurement.

When performing such measurements with short tips, the tip cannot reach the bottom of the crevices because the structures touch the cantilever itself and not the tip. This leads to an inverted imaging process, on which the high structures act as tips and scan the cantilever. As artifact this results in the topography of the cantilever instead of deep trenches. As an example, such a measurement was performed. In figure 3.11 this artifact is visible. The high protrusions are dominating the topographical image as long as they are touched by the tip. On the deep trenches, when the protrusions are touching the cantilever, the form of the cantilever is represented. In this image, an NSG10 (NT-MDT) cantilever is used with a specified tip length of 14 µm to 16 µm. The cantilever itself has a triangular shape at the end where the tip is located. This can be seen directly by looking at the image and comparing it with the form of the cantilever.

The cantilever itself is tilted at an angle of about 12° to the sample surface, to ensure that only the tip is getting in contact with the sample. A fit on those two blue marked regions reveal an angle of 13°, which confirms the inverse imaging process.

To overcome this problem, a tip longer than the protrusions and with a higher aspect ratio is needed. For 3D printing this is easy to accomplish. Therefore, a cylindrical tip was designed with a height of 30 µm and a smaller base than the NSG10 tip to ensure a good mapping of the high structures.

As tipless cantilever the tapping type All-In-One (BudgetSensors) was chosen. In terms of spring constant and resonance frequency it is comparable to the NSG10 tapping cantilever with tip used to obtain the topography in figure 3.11. After writing the tip with a writing speed of 20 mm/s (1 mm/s for the last 5 µm), slicing in 100 nm layers (50 nm for the last 5 µm) the rose petal replica was measured again. In figure 3.12 the recorded topography is depicted.

No cantilever-form-like artifact is visible and deep trenches between the high structures are visible. On the plotted cross section between 50 µm and 65 µm a vertical distance of approximately 25 µm was resolved.

Not only are long tips needed for AFM. Various kinds of other shapes are developed for special measurements like adhesion measurements [131], elastic modulus measurements [132] or

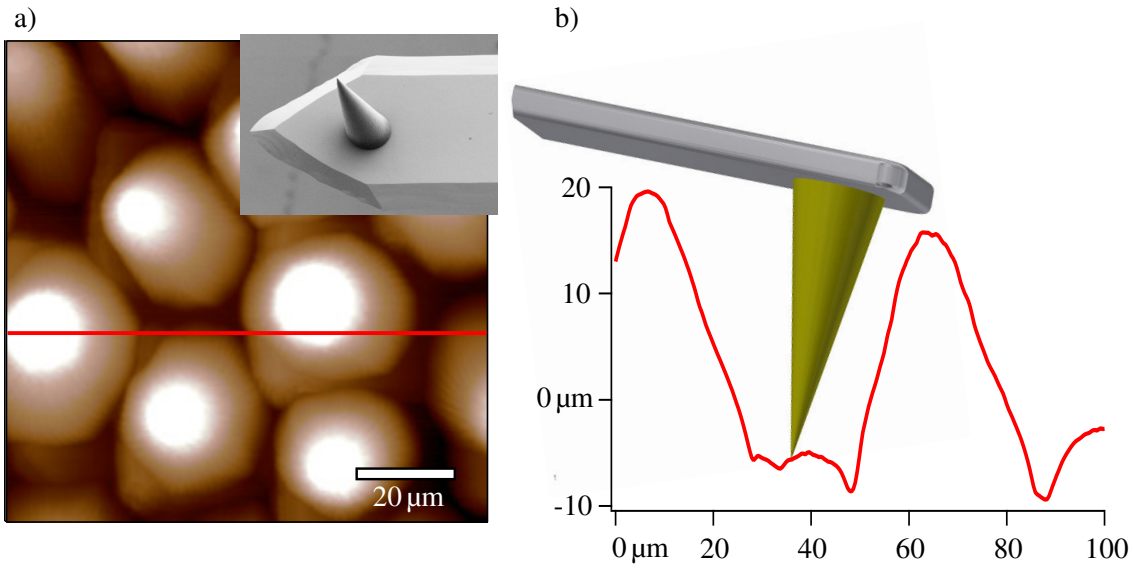

Figure 3.12: **a)** AFM image of rose petals with a long polymer tip. As inset a SEM image of the printed tip is provided. High protrusions and deep trenches with a height difference of more than 25 µm are recorded without artifacts as presented in the cross section **b)**.

protruding tips for optical alignment with respect to the probing position when the AFM has a camera above the sample. In figure 3.14 a collection of SEM images of such tips is provided, as well as a zoom image of the end of a tip. Besides the long or short high aspect ratio tips, a protruding tip is depicted. If a protruding tip is desired, only a few commercial cantilever types are suitable because of the complex etching process.

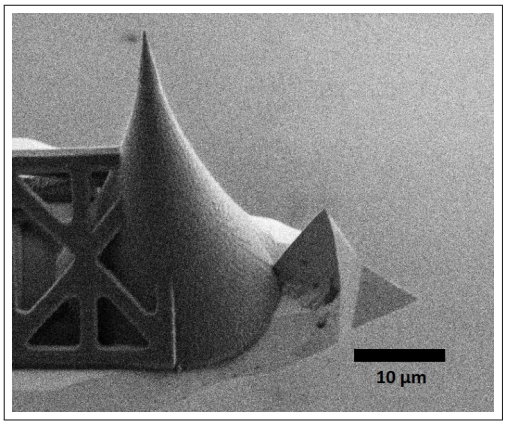

Figure 3.13: SEM image of a polymer tip written over a standard one.

With 3D printing it is possible to choose the favored cantilever and then get the favored tip shape by an easy writing process, even if the cantilever is already equipped with a tip. For elastic property measurements a complex mathematical system has to be calculated because the pressure depends on the indentation depth and contact area of the tip [133]. Different assumptions of the tip shape and the contact process itself lead to different solutions like the Hertz Model [134], in which it is necessary to decide by the acquired data if a cone or sphere-like tip is used, the Derjaguin-Muller-Toporov [135], the Johnson-Kendall-Roberts [136] or the Oliver-Pharr model [137]. To overcome these approximations, different methods like gluing a sphere by hand to the ends of cantilevers was introduced [121]. With 3D printing this is no problem at all. If it helps to simplify the math to have a spherical tip, it is possible to simply write a spherical tip. Despite the free choice of form and size an additional approach can be used. The finished structure can be converted into carbon by a pyrolysis process [138, 139]. Due to the shrinkage of the structure down to 20 % of the original size [140], this allows tips to be smaller

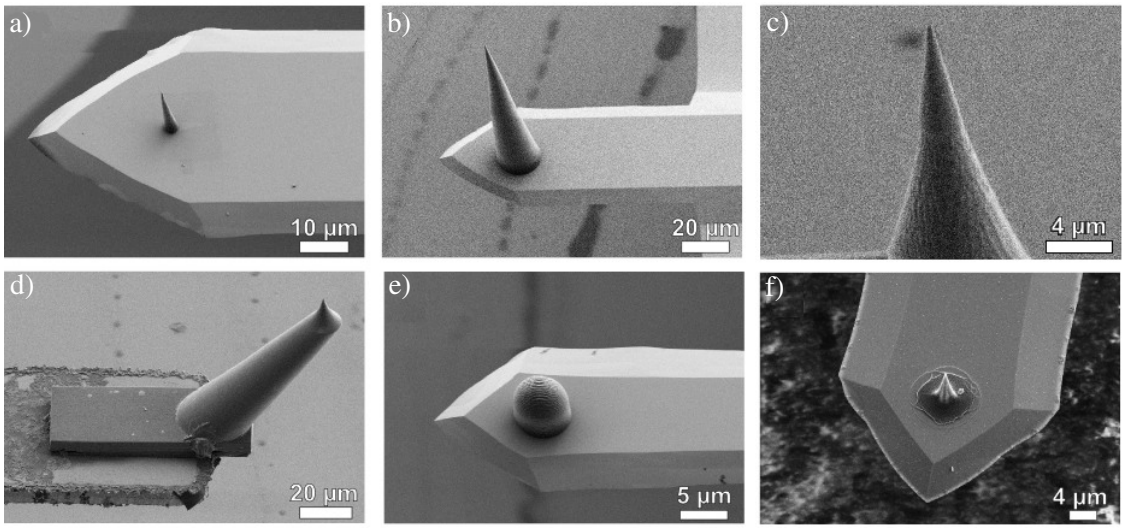

Figure 3.14: A collection of SEM images of different tips. The tips are not only customizable in size **a)-c)**, also some tips are adapted to special functions. For spectroscopy experiments it is necessary to have a protruding tip **d)**, for measuring of elastic properties a sphere like tip is helpful **e)**. Additionally, after a pyrolysis process the carbon tip is harder and can easily be functionalized **f)**.

than the lithography limit. Furthermore this carbonized structures are electrically and thermally conductive, biocompatible, harder and easy to functionalize [141, 142].

3.7 Mass Production Capability

For research and industry, it is of high interest to not only have possibilities to produce tailored probes but also to have the possibility to fabricate them fast and in high numbers. 3D printing offers this possibility. To demonstrate the capabilities, a four inch wafer with TMR-sensors was prepared and etched. The wafer was etched by Dr. Ali Tavassolizadeh from the University of Kiel. The production of one wafer takes more than two weeks of machine time in a clean room. Therefore a failsafe procedure with a realigning of every cantilever was used. The wafer was loaded into the wafer holder of the Nanoscribe printer.

An Excel file containing the coordinates of every cantilever was provided with the wafer. For a big wafer like this some issues have to be considered. Not much of the used resist for the tips should be wasted. Thus, instead of covering the whole wafer with resist, a meniscus of resist was used between the wafer and the objective. The cantilever chips were held in place by two small bridges of under-etched silicon. Fast movements, especially in vertical direction might break those bridges and the chips might be lost. Since the written tips are between 20 µm to 30 µm long (different tip models were used) a small shift of the holder could cause small or non-sticking tips. To overcome this, every cantilever was automatically refocused by varying the focus plane and tracking fluorescence light, which only appears in the resist. To be sure to have found the surface of the cantilever, a small test writing was also performed automatically. The whole procedure took less than 90 seconds per cantilever and thus the whole wafer, equipped with 128 cantilevers

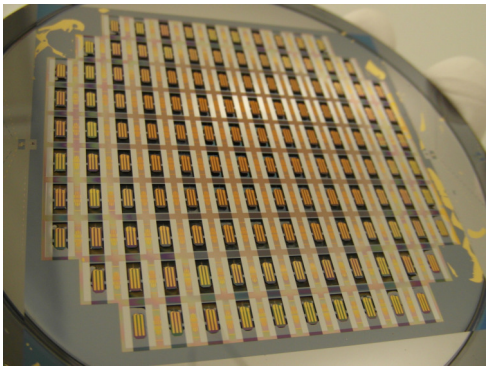

Figure 3.15: Photography of a wafer with etched cantilevers, each equipped with a TMR sensor.

was written in about three hours. A video of the process was recorded and some important snapshots are shown in figure 3.16. For the tips, different sizes and forms were chosen to be able to find the best performing one of self-etched TMR cantilevers. A tilt of the tip by 13°, which is used by the atomic force microscopy holder to ensure that the tip is in contact with the specimen first and not another part of the cantilever, was easily done in the CAD model. After some tests on an already damaged wafer, good parameters were found and the writing process could be performed without any losses.

3.8 Summary and Conclusion

In this chapter the usability of polymer and 3D printing for tips for atomic force microscopy was investigated. 3D printing as process to produce tips is cheap, fast and exact enough for scanning microscopy. This helps on one hand to overcome some artifacts produced by too short tips of commercially available cantilevers and on the other hand to equip non-commercial self-made cantilevers like self-sensing TMR cantilevers with high quality tips with low effort. The commercially available polymer which was used has shown good resistance to wear, fine resolution and some additional useful properties like the possibility to carbonize the tip, which shrinks the tip and gives the ability to functionalize it. To produce conductive tips a coating can be used just as on commercial cantilevers. This offers the opportunity to work in practically every AFM mode, beside the dynamic or contact mode. Further development on the polymer could result in finer resolved or optionally conductive tips without the need of an additional coating.

A shorter version of this chapter was published as 'Tailored probes for atomic force microscopy fabricated by two-photon polymerization', Gerald Göring[1], Philipp-Immanuel Dietrich[1], Matthias Blaicher, Swati Sharma, Jan G. Korvink, Thomas Schimmel, Christian Koos, Hendrik Hölscher: Applied Physics Letters (109), Cover Story and Featured Article (2016)

[1] contributed equally to this work

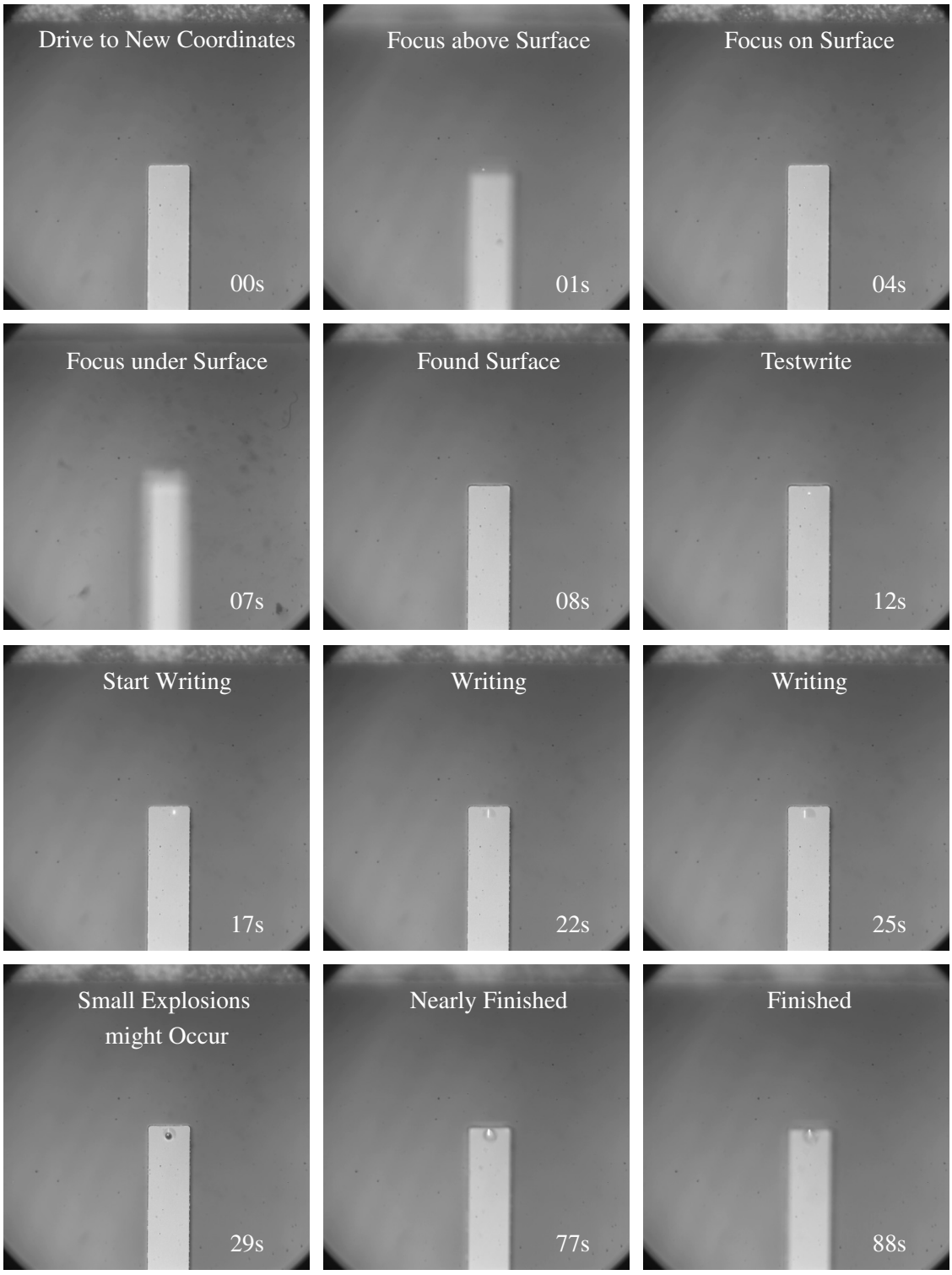

Figure 3.16: Writing process of automated wafer scale tip production. A tip is written in less than 90 seconds. On the right bottom corner of every snapshot a timestamp is provided. The 3D printer drives to the new coordinates and automatically focuses on the surface by tracking fluorescence light. After the surface is found, a test write is performed. When the structure is observable, the writing process of the desired structure starts and finishes within 88 seconds for the whole process. Small detachments of the top layer lead to a sudden formation of gas bubbles in the resist, which looks like small explosions.

4 Rebar Structures on Cantilevers

4.1 Introduction

Apart from the intermittent contact mode and contact mode presented in chapter 2.1.3, there are further modes in atomic force microscopy which allow to gather more information about the sample than simple topography [143, 144]. The oscillation of the cantilever is influenced by attractive as well as repulsive forces. When setting a certain amplitude, a trade-off between a stable feedback with a large amplitude, or higher resolution with a small amplitude has to be chosen. The better resolution is obtained by less noise and higher sensitivity for short-distance forces for small amplitudes [77, 78, 122].

This problem can be avoided by using other techniques, such as bimodal AFM [80]. In this mode, the cantilever is not only oscillated at its ground state, it is also driven at a higher eigenmode. Thus it is possible to use a large and stable amplitude for the topographical feedback and still have a high sensitivity due to the small amplitude of a higher harmonic. There are also other modes which use band excitation, for example to directly measure dissipation energy through the cantilever-sample system's quality factor [145, 146].

In intermittent contact mode the phase signal is an indicator for energy dissipation as calculated in chapter 2.22. This means that even if a heterogeneous sample is completely flat, it is possible to distinguish between the different materials due to the phase shift induced by different material properties. For this modes of operation, the frequency spectrum of the cantilever is of high interest.

The cantilever resonances are given by the geometry and the material the cantilever is made of. Since there are only two common materials for the cantilever, silicon and silicon nitride [104, 105], the main differences are shape and geometrical dimensions. Manufacturers offer cantilevers with different main characteristics like spring constant and resonance frequency but it is impossible to cover all customer needs by a few types of cantilevers. The behavior of higher modes are e.g. not mentioned in the data sheet at all. By using a second material, in this case a polymer, multiple additional degrees of freedom are obtained.

Furthermore, tuning cantilevers leads to the possibility to operate multiple cantilevers parallel in tapping mode. This is typically inhibited due to the large amount of data acquisition channels, all with their own operation frequency. By tuning all cantilevers to the same frequency, basically one lock-in amplifier can be used and the data from all cantilevers can be multiplexed.

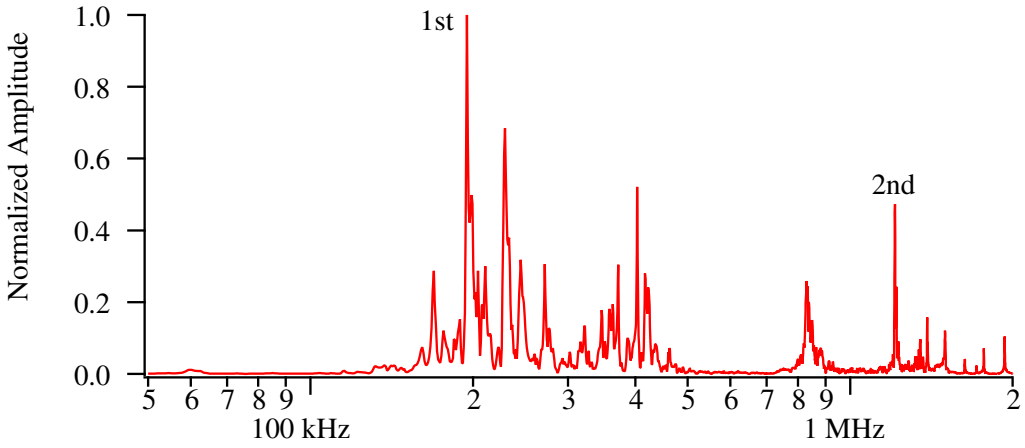

Figure 4.1: Frequency spectrum of a BudgetSensors All-in-One cantilever. Besides the labeled cantilever resonances, there also exist other resonances caused by the AFM itself. The amplitude is normalized to the first harmonic.

This simplifies the setup and data processing considerably. As the frequency spectrum of a cantilever is important for different AFM modes the tuning of this spectrum will be presented in this chapter.

4.2 Suppressing Higher Eigenmodes

Figure 4.1 represents a typical frequency spectrum of a BudgetSensors All-in-One cantilever. To measure the spectrum, the cantilever was mounted in a commercial AFM setup (MFP3D, Asylum Research) and a frequency sweep between 50 kHz and 2 MHz was performed. Multiple spectra of one particular cantilever were recorded while varying laser spot position and multiple unmounting and mounting cycles were performed. All recorded spectra were similar, so figure 4.1 represents the cantilever appropriately.

This figure shows that besides the marked first and second harmonic resonances there also exist lots of other resonances, caused by the cantilever holder, the shake piezo and when measuring in water, some acoustic modes will additionally appear [147].

By employing the absorptive nature of the polymer [148], it is possible to selectively suppress unwanted modes [115]. To suppress higher eigenmodes, it is possible to add a large-area polymer on the cantilever. According to section 2.1.5 this will have different major effects on the cantilever properties. It will:

- Decrease the resonance frequency,
- Increase the spring constant,
- Decrease the quality factor,

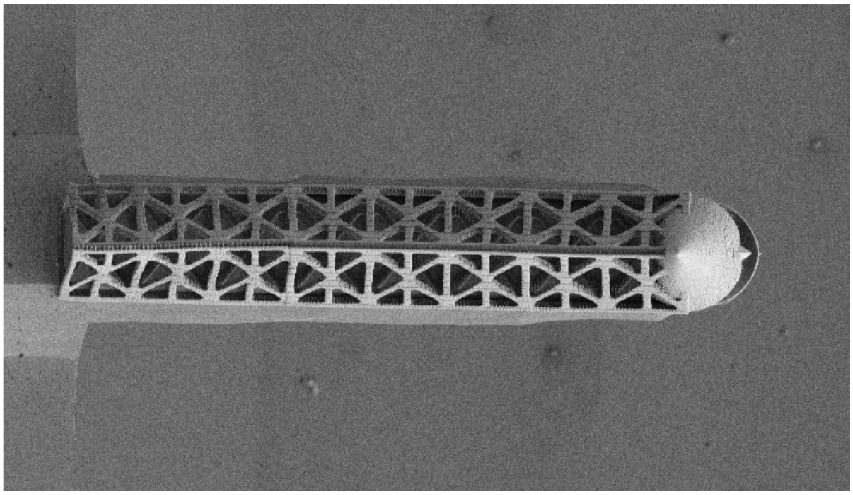

Figure 4.2: SEM image of the truss structure written on the cantilever. This structure is lightweight but absorbs unwanted modes. The framework is approximately 130 µm long and 25 µm wide, a bit smaller than the width of the cantilever (30 µm) to prevent protrusions.

dependent on the thickness of the layer since it will basically put both cantilevers (the silicon one and the polymer one) in parallel. To minimize this effect, it is possible to add a framework structure consisting of triangles, which keeps the stiffness high but reduces the added mass compared to a full layer. This structure is used on cranes and timbered houses for these reasons. The cantilever in figure 4.2 is approximately 130 µm long and 30 µm wide.

In this section, a continuous truss structure with no gaps was chosen. A SEM image of the structure on the cantilever is provided in figure 4.2. This structure stiffens the cantilever in a way that the energy used to form antinodes, on which the cantilever bends the most, is absorbed. Thus the favored frequency is the fundamental one.

For the writing process the cantilever was fixed on a glass substrate. To write the structures, the framework design was sliced in 100 nm layers, the writing speed was set to 20 mm/s and as objective a 63x, NA=1.4 objective was used. Although the cantilever itself is barely visible with the naked eye, the finely resolved framework is written flawlessly.

After the writing and lift-off process, the same cantilever from which the spectrum in figure 4.1 was gathered was again mounted on the cantilever holder of the MFP3D AFM.

Then again, multiple spectra were recorded with different laser spot and cantilever positions. Figure 4.3 represents accordingly the spectrum of the tuned cantilever. As intended, all resonances but the first one were dramatically reduced. The reduction leads to a ratio of the first harmonic to the rest by more than one order of magnitude.

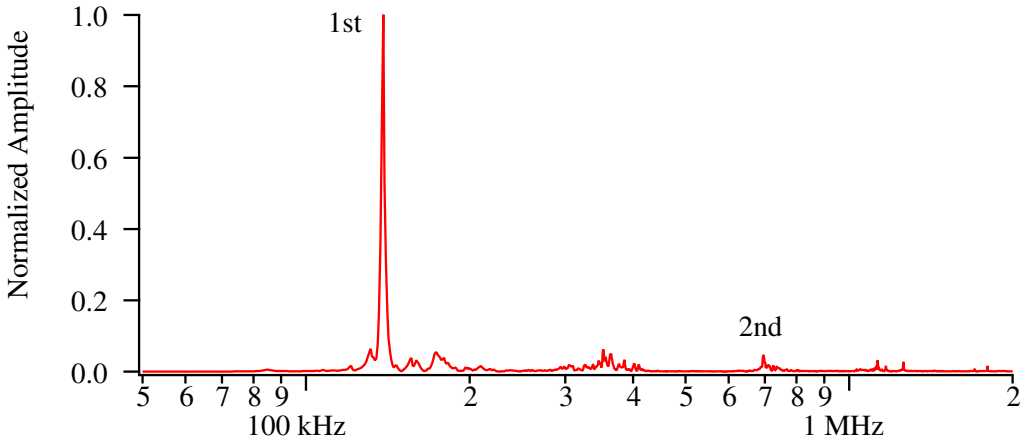

Figure 4.3: Frequency spectrum of a tuned BudgetSensors All-in-One cantilever. Compared to figure 4.1 the first harmonic resonance is dominating. The amplitude is normalized to the first harmonic.

4.3 Enhancing Higher Eigenmodes

For measurements utilizing other harmonics than the first one, it might be of interest to reduce the first harmonic and highlight another one. In this section a structure is proposed which enhances the second harmonic over the first one. In contrast to the ground state, the second harmonic produces an anti-node in the bending of the cantilever. By accenting this antinode, this mode should be favored.

To force an anti-node on the proper place (see section 2.1.5), a gap in the framework can be chosen. This forms a kind of hinge for the mode.

Here again, the same procedure as in section 4.2 was applied to measure the spectrum in figure 4.4. By comparing this spectrum with the spectrum in figure 4.1, a typical problem becomes visible. Even though both cantilevers were from the same batch, the frequency spectrum differs in the ratio of the first to the second harmonic in factor of more than two. Most standard AFM

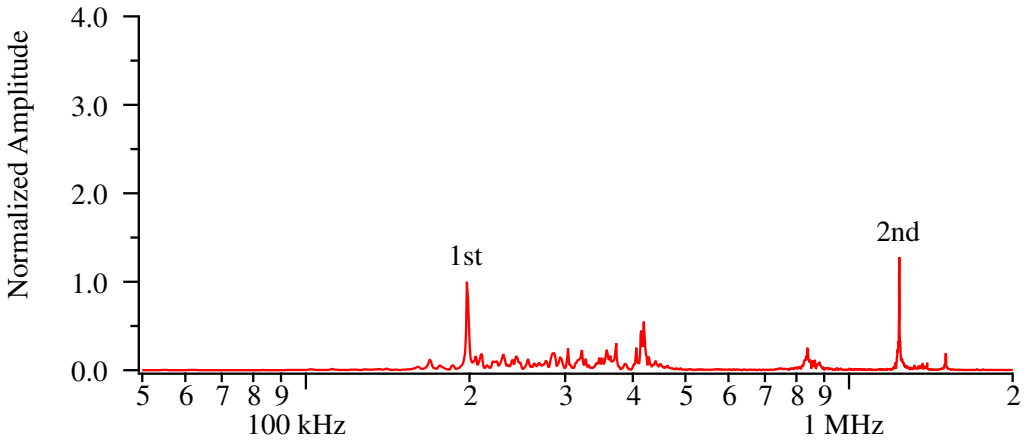

Figure 4.4: Frequency spectrum of an untreated All-in-One cantilever from BudgetSensors. The amplitude is normalized to the first harmonic and the scale was chosen to be the same as in figure 4.5 for an easy comparison.

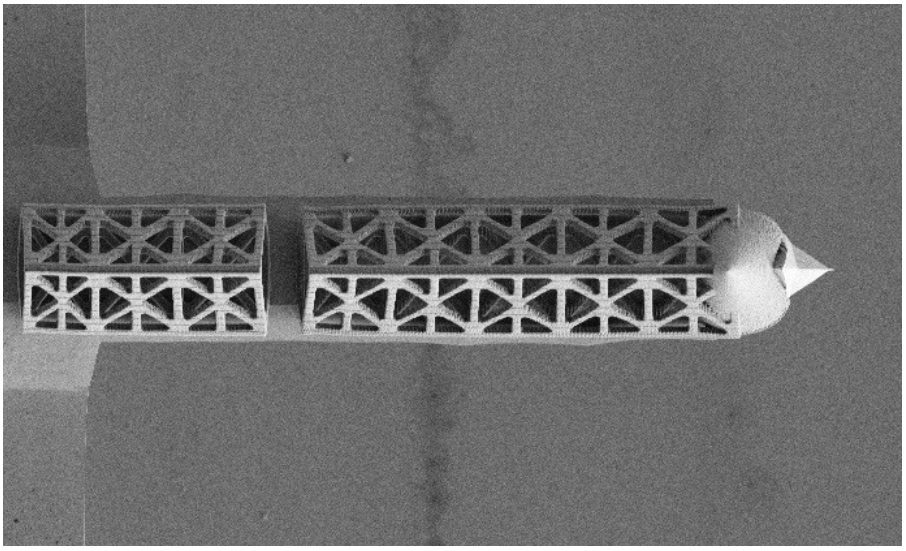

Figure 4.5: SEM image of the tuned All-in-One cantilever. The cantilever is 130 µm long and 25 µm wide. The structure seems a little bit wider compared to figure 4.2 due to the tolerances in the etching process of the silicon cantilever.

users do not care much about higher harmonics, so it is reasonable that fabrication processes are not optimized for this usage.

Post-production tuning of the cantilever helps to have the desired frequency response. In this section, the second harmonic is the mode which will be enhanced. As visible in figure 4.5, the written structure seems to be not as wide as the structure in figure 4.2.

The positioning of the 3D printing itself is very exact, since it is possible to write some test spots and watch polymerization in situ during the same objective the laser is focused through. The movement of the laser is caused by the galvo scanner (compare section 5.5 and section 6.5) which has high repeat accuracy. Here, it is the cantilever which is inaccurate. BudgetSensors, the manufacturer of the cantilevers, specifies the width of the cantilever with: 30 µm $\pm$ 5 µm.

It follows that not the structure itself is inaccurate, it is the cantilever due to the fabrication tolerances.

After the SEM imaging, the cantilever then again was mounted into the cantilever holder of the AFM on which new frequency spectra were recorded. Again, independent from the laser spot position, the spectra were similar with reference to essential features like amplitude and additional oscillations. Exemplary, a spectrum of the tuned cantilever is depicted in figure 4.6.

As intended, the second harmonic is amplified compared to the first one. In addition, compared to the untuned spectrum, all the oscillations caused by the cantilever holder and piezo are also reduced which helps to obtain a stable feedback and will improve image quality due to less noise.

This measurement was performed with a classical AFM setup, where the silicon cantilevers were read out through an optical beam deflection readout as explained in section 2.1.1. One current

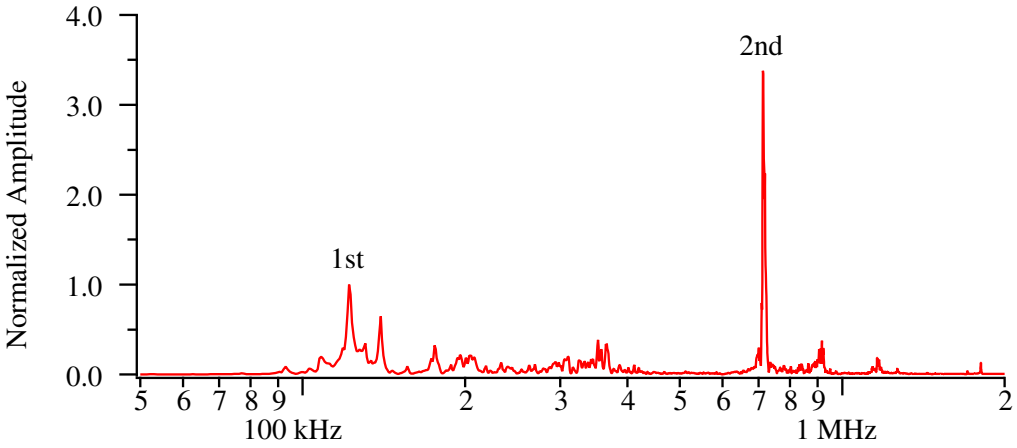

Figure 4.6: Frequency spectrum of the tuned cantilever. As desired, the second harmonic outperforms the first one in amplitude. The amplitude was normalized to the first harmonic.

active field of research is also self-sensing cantilevers which typically have a sensor integrated, consisting of piezo active [7–9] or magnetoresistive layers [119, 120], see section 2.1.1. In those approaches it can help to improve the sensitivity to stabilize the whole cantilever in a way that the highest bending of the cantilever is in the region of the sensor.

In the next section this idea will be pursued.

4.4 Improving Sensitivity of Self-Sensing Cantilevers

Self-sensing cantilevers are a desirable advance in atomic force microscopy [149]. Many approaches like fluorescence microscopy combined with atomic force microscopy are inhibited due to the bulky head of the AFM, or only accessible with restrictions, for instance only transparent samples can be investigated by an inverse fluorescence microscope, while the AFM operates from above the sample [150, 151].

The most intensive strain of the cantilever is at its base and decreases along the way to the tip as simulated in figure 4.9. For this reason, the sensors of the self-sensing cantilevers are attached to the base of the cantilever. This is in contrast to the classical deflection readout, in which the laser is focused on the free end of the cantilever, since this is the area with the highest change in the angle of the cantilever.

To maximize sensitivity, it is of interest to maximize the bending on the sensor. This can be accomplished by stiffening the cantilever between the sensor and the tip. When minimizing the bending of the remaining cantilever, for a fixed traveled distance of the tip the bending of the sensor is maximized.

Here again, the same rebar structure as in section 4.2 is used. This framework provides a high stiffness by low weight. The homemade TMR cantilever is much longer than a commercial can-

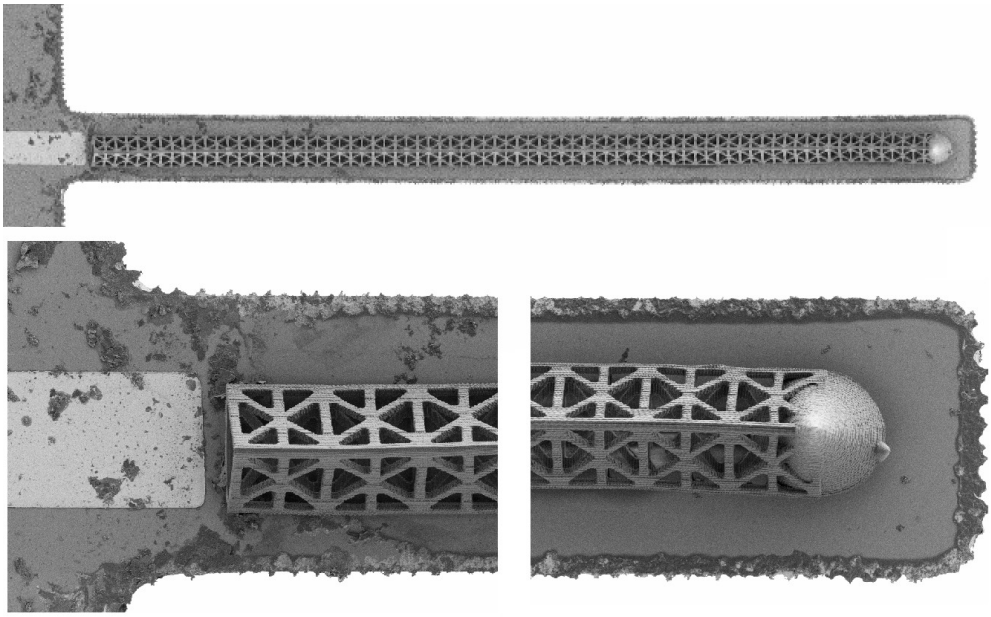

Figure 4.7: SEM image of a TMR cantilever with an additional framework to maximize sensitivity. Zoom-ins of the base and the free end of the cantilever are provided at the bottom. The cantilever is approximately 600 µm long.

tilever in order to have proper characteristics for intermittent tapping mode, while being thicker for fabrication reasons.

To fabricate a structure covering a cantilever of such a length with 3D printing, the writing process is broken down into multiple segments which are done one after the other, the so called stitching.

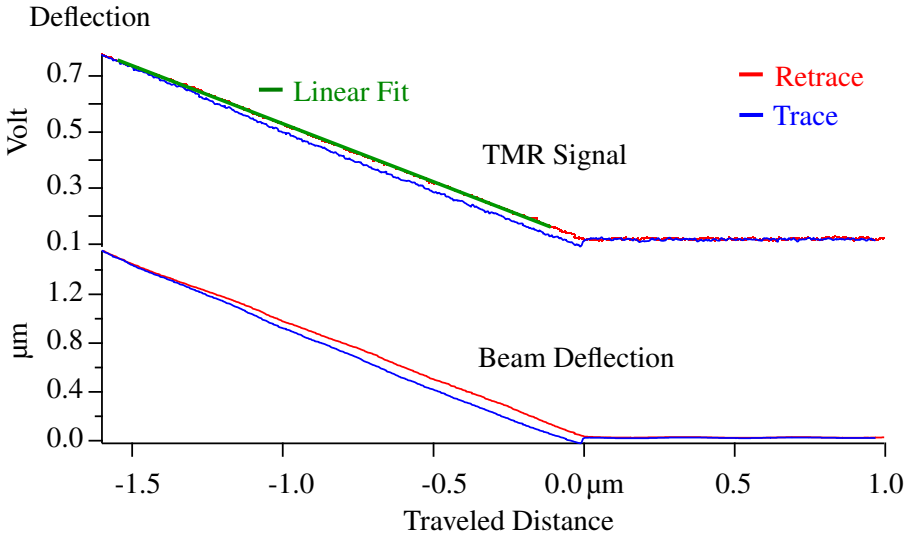

Figure 4.8: Force distance curve of a cantilever with a TMR sensor. The TMR signal was acquired while performing a force distance curve with a conventional deflection readout for the triggering.

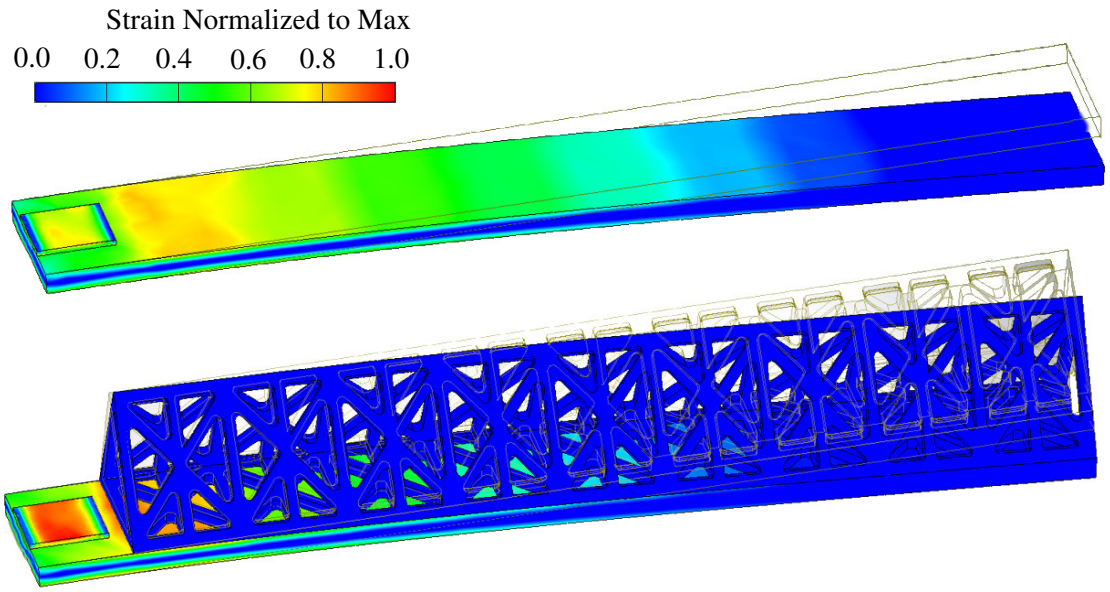

Figure 4.9: Simulation of the strain of a TMR cantilever with and without a framework when moving the end of the cantilever for a AFM typical distance of 250 nm. Both simulations use the same scale. The tip was left out for performance reasons.

To measure the sensitivity of a self-sensing system, force distance curves are acquired (see section 2.1.4). The cantilever tip is a few micrometers above the surface and then pressed against a hard surface for a certain traveled distance of the z-piezo. When the cantilever gets in contact with the surface it begins to bend. Since the traveled distance is well-known due to the z-sensor, the calibration factor to convert the measured photocurrent into a distance can be acquired. When installing a cantilever equipped with a TMR sensor, this procedure can be performed while reading out the TMR sensor on an additional input channel of the controller. Figure 4.8 depicts a typical measurement obtained with the cantilever in figure 4.7 before the structure was written. Such measurements were performed before and after the structure was added. The linear fit resulted in a slope of 415 mV/µm for the virgin cantilever and a slope of 780 mV/µm for the tuned one, which equals an improvement of nearly 90 % in sensitivity.

TMR sensors have a hysteresis in their sensitivity, since the sensitivity is dependent on the magnetization of the sensor layer, which is magnetized before each experiment. This makes a reliable direct comparison of a chosen cantilever before and after adding the framework impossible. Therefore, a simulation was performed with Autodesk Inventor. For the simulation a silicon cantilever with a length of 200 µm, width of 30 µm and a height of 4 µm was equipped with a framework and a sensor with a size of 15 µm $\times$ 15 µm was placed at the base of the cantilever. The TMR sensor is a strain measuring sensor which has a linear behavior for small stresses as in AFM. Therefore, the simulated stress is directly proportional to the measured deflection signal. In the simulation, the sensor side of the cantilever has a fixed constrain since this side is connected to the chip. The other side, where the tip was left out for performance reasons, the cantilever tip was pressed down 250 nm to simulate a typical scenario. The simulation is depicted in figure 4.9.

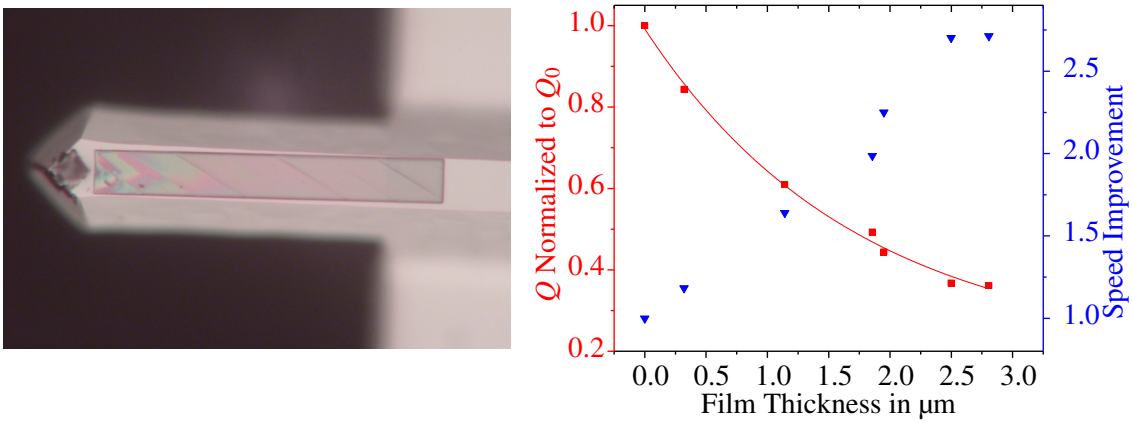

Figure 4.10: Measurement of the quality factor of a 125 µm long cantilever, with polymer films of different thicknesses. The damping of the quality factor improves the scanning speed and the additional mass reduces the resonance frequency, which also has an impact on the scanning speed. The damping effect dominates the speed improvement factor.

It shows that the strain at the sensor from the cantilever with the framework is increased by nearly 50 %. This makes the measured improvement of the sensitivity of nearly 90 % plausible. The simulated improvement depends on the geometry of the cantilever but the framework always increases the sensitivity of the sensor. Note that this is the behavior for a given traveled distance. When applying a force, the structure stiffens the cantilever which results in less deflection, which can nearly annihilate the improvement. So this technique is only applicable when using a strain sensor for deflection readout.

4.5 Enhancing Scanning Speed

The theoretical maximum of scanning speed is determined by the quotient of π times the resonance frequency and the quality factor. To increase the speed, either the resonance frequency can be increased or the quality factor reduced. Increasing the resonance frequency can be reached by decreasing the size of the cantilever. Different solutions have been published but lacked of a high signal due to the low reflective area of a small cantilever [86, 152]. Additionally the readout technique has to be changed fundamentally to be able to process those highspeed data [153, 154]. The quality factor of a cantilever is also a property of the material used. Some techniques have shown to control the quality factor electrically with a complicated feedback or excitation model [155, 156]. Here, simply a layer of polymer on the bottom side of the cantilever was added. The internal damping of a polymer like the used IP-Dip (Nanoscribe GmbH) is higher than that of a silicon cantilever. To test the effect, the quality factors of multiple cantilevers of the same type (NSC15, MikroMasch) were measured and layers of polymer with different heights were subsequently added and finally the quality factor was remeasured. Here, full layers were used instead of frameworks as in the section above. For applications, frameworks are better since they do not change the resonance frequency of the cantilever that much due to their lower weight but for this measurement a framework would prevent a reusage of the cantilever for adding an additional

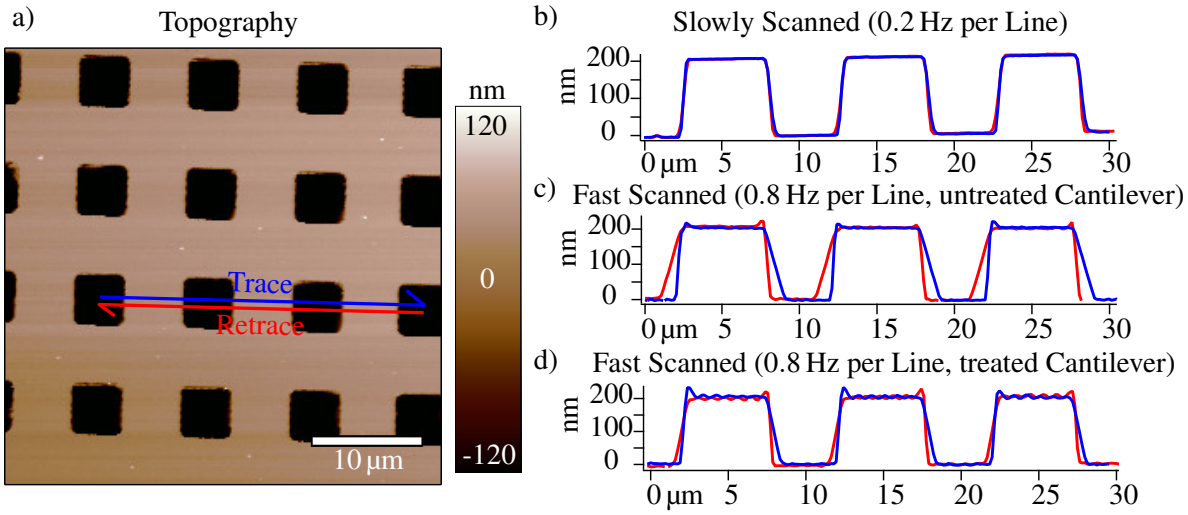

Figure 4.11: **a)** Measurement of a calibration grid. **b)** A cross section of a good measurement for a slow line frequency of 0.2 Hz. Trace and retrace match well. **c)** A cross section with a scanning speed of 0.8 Hz per line. The cantilever needs multiple oscillation cycles to increase its amplitude, which leads to the so called 'parachuting' at steep edges. **d)** When using the same setup with a cantilever with a reduced quality factor, it leads to a reduction of the parachuting effect. Here, the z-feedback is too slow to scan fast enough to obtain the same parachuting effect as with the untreated cantilever and starts ringing.

polymer layer. To measure the film thickness, the reflectometer Nanocalc2000 (Micropack) was utilized. A reflectometer acquires the spectrum of the reflected light, which is modulated due to wavelength dependent interference of the reflected beams from top and bottom of the layer. The refractive index of the resist IP-Dip was taken from literature [157] for this measurement.

The thickness of every cantilever was the mean value of multiple measurements. Figure 4.10 depicts an optical microscope image of a speed improved cantilever. The measurement of multiple cantilevers with different thicknesses before and after the treatment show a decrease of the quality factor by a factor of 3 for a layer thickness of 2.8 µm. An asymptotic fit reveals a reduction of the quality factor of up to 5 for thicknesses bigger than 5 µm. The resonance frequency changes due to the added mass but the effect is negligible (3 % reduction for the thickest layer) compared to the improvement of the speed due to the quality factor. To demonstrate the improvement, a scan was performed with different cantilevers, an untreated one and one with a reduction in the quality factor by $Q = \frac{Q_0}{2}$. Figure 4.10 depicts the measured grating with cross sections for the different cases. The first cross section acquired with 0.2 Hz per line shows a good measurement. No overshoots or ringing is visible and trace and retrace match perfectly. The parachuting effect appears at sharp edges at which the cantilever loses contact to the sample and increases its amplitude. Due to the high quality factor of a silicon cantilever this takes several periods of the oscillation which leads to a sloping edge instead of a steep one. This effect only occurs when the topography of the sample causes a detaching of the cantilever. When a high step in direction of the cantilever occurs, the amplitude is directly reduced and the quality factor has no effect. This makes this effect asymmetrical when scanning a gap. To demonstrate the effect, the scan rate per line was increased to 0.8 Hz. The cross section reveals a clear parachuting effect. An increase of the feedback parameters did not change this effect. For the treated cantilever this effect is

reduced. Actually, the feedback parameters of the system have to be increased so much to show the effect that ringing occurs. This means that in the measured topography small oscillations are produced since the inertia of the feedback system for the z-direction of the AFM is too high and so the control loop overcorrects the distance. Although a cantilever with only a small reduction in quality factor was chosen, the effect is clearly demonstrated.

4.6 Summary and Conclusion

The more advanced the AFM techniques are, the more does the importance of the frequency spectrum of the cantilever grow. It it is nearly uninteresting for basic modes like tapping or contact mode, but for an investigation of the mechanical properties of the sample it is of high interest. To get comparable results, similar cantilevers should be used. Cantilevers even from the same batch behave differently due to the high production tolerances of commercial cantilevers. 3D printing gives the opportunity to tune the spectrum to the desired one and thus obliterate those differences. It also helps to overcome typical limits for scanning speed since it reduces the quality factor of the cantilever and thus directly improves the cantilever transient response. For self-sensing cantilevers 3D printing also helps to improve the deflection of the probe in the way that most stress is applied at the sensor.

A shorter version of this chapter was published as 'Tailored probes for atomic force microscopy fabricated by two-photon polymerization', Gerald Göring[1], Philipp-Immanuel Dietrich[1], Matthias Blaicher, Swati Sharma, Jan G. Korvink, Thomas Schimmel, Christian Koos, Hendrik Hölscher: Applied Physics Letters (109), Cover Story and Featured Article (2016)

[1] contributed equally to this work

5 Polymer Cantilever for Atomic Force Microscopy

In the last two chapters 3D printing was used to modify cantilevers consisting of silicon. Since it is easy to write other structures, it is obvious to print a complete cantilever. Besides the freedom of writing arbitrary forms, it is also possible to position the structures exactly where they are needed. For atomic force microscopy in contact mode, the cantilever can just be written on the edge of a chip as on commercial cantilevers. Here, it is possible to design the cantilever with the desired properties and use it directly after coating it with silver. The written cantilevers

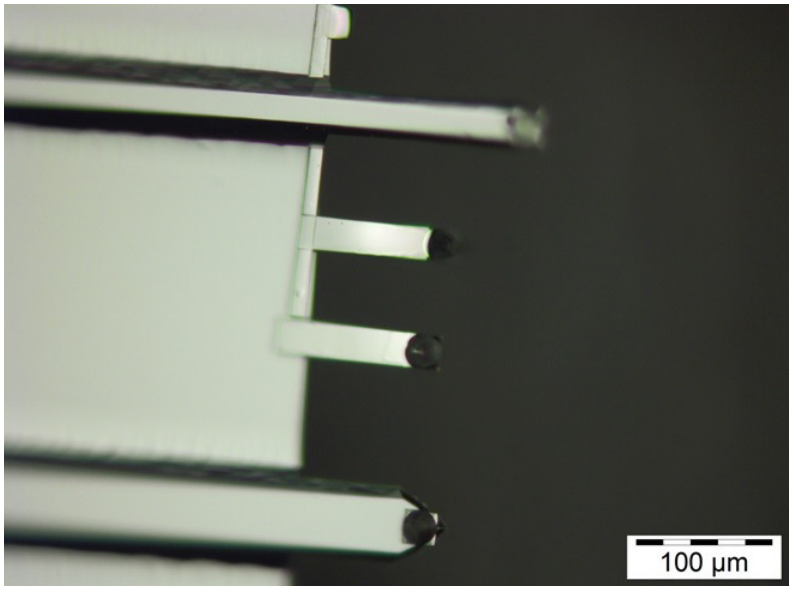

Figure 5.1: Two short cantilevers written on a chip between two cantilevers of a commercial chip. To obtain good reflection, the cantilevers were evaporated with silver.

were a first proof of principle and can be used as normal cantilevers in AFM. They have a resonance frequency of 93 kHz and are indistinguishable for the user from the silicon cantilevers in tapping mode except the low quality factor of $Q \approx 90$ instead of $Q \approx 1000$ typical for silicon cantilevers. This difference in quality factor leads to two noticeable differences. The amplitude of the polymer cantilever is smaller than the amplitude of the silicon one when shaking with the same energy and the polymer cantilever achieves the free air amplitude after 90 shaking cycles whereas the silicon one needs about 1000 cycles. This inherently allows faster scanning speed since the cantilever has to oscillate at its equilibrium state before measuring the next point. In fact, the amount of data points collected per second can be calculated by:

$$n = \frac{\pi \cdot f_{res}}{Q}$$

with n as points per second, f_{res} as resonance frequency and the quality factor Q. For the same resonance frequency the polymer cantilever is thus able to collect ten times more data points per time unit than the silicon one [87].

Whereas the AFM is a standard tool to manipulate objects down to the nanometer or even atomic range [105, 158, 159], the microscope itself is magnitudes larger than the typical scan sizes which inherently inhibits in situ measurements where less space is proivided as in endoscopic measurements for example. Additionally, it consists of many non-standardized discrete components which limit integration to most other analytical tools like fluorescence spectroscopy. It is always necessary that the parts can be disassembled and adjusted due to wear of the cantilever [160] and its production variances. Contamination with dirt particles also leads to the requirement of a new cantilever. For the change of the cantilever several steps are required:

Change of the Cantilever: The cantilever itself has to be taken out of the cantilever holder. Usually it is possible to extract the cantilever holder and pull the cantilever, which is hold by a leaf spring, off the holder. Then, the new cantilever can be fixed in the holder and the holder can be reassembled into the AFM head.

Alignment of the Laser: To get the laser reflected into the photodiode, it has to be aligned in both lateral directions. The cantilever itself has a typical width of 30 µm and thus it is uncommon that the laser hits the cantilever in the same position as the previous one. When using a different cantilever type, it may vary more than a millimeter due to non-standardized parameters like the length of the chip.

Alignment of the Photodiode: Since the laser and the cantilever are now in different positions, the reflected laser will also hit the photodiode in another spot. The photodiode is typically divided into four quadrants in order to be able to measure the lateral and vertical deflection of the cantilever. If every quadrant produces the same photo current, the laser is in the middle of this photodiode.

Some self-sensing approaches overcome these steps by using strain sensors on the base of the cantilever [119]. For more complex measurements like process monitoring in chemical deposition processes or microfluidic systems, on which fluids can be added, exchanged or removed, more advanced equipment for the laser readout is necessary [161]. For miniaturization of AFMs different approaches were used. One was to slowly ion mill a cantilever directly out of fiber end [13, 14]. This approach delivers well aligned cantilevers which can be read out interferometrically. Since there is only one optical channel, these cantilevers can be used in contact mode only and without the possibility to detect the lateral bending of the cantilever. This is the main advantage of the contact mode over tapping mode, since it allows to gather information about the friction on the sample.

Here, two-photon absorption 3D lithography is introduced as a tool to write cantilevers directly on laser facets. 3D printing has already shown to be able to fabricate well-aligned freeform structures on optical fibers [162]. Additionally, 3D printing is able to print beam shaping lenses

on facets [163, 164] or enables highly efficient optical coupling [18]. Even 3D printed fiber microphones have been demonstrated [165].

However, all of these approaches are limited to simply emitting and/or collecting light from one channel. For AFM in dynamic mode at least two channels are required. One for actuation and one for the distance readout. To have multiple channels, V-goove fiber arrays can be used. Due to their fabrication process the alignment of the fiber to each other has small tolerances. This also gives the opportunity to have more channels for other experiments as shown in chapter 6. In the next section methods are shown to get the best actuation and readout solutions.

5.1 Fabrication

5.1.1 Fabrication Process

For the fabrication of the cantilevers, commercially available V-groove single mode fiber (SMF) arrays are cleaned and mounted into the fiber array holder. As described in section 5.1.4, a pre-baking process is performed to vaporize the water on the surface of the array to enhance the adhesion of the structure. After this procedure the holder is mounted into the Nanoscribe Professional GT with the fiber facets perpendicular to the optical axis of the objective. The focus of the camera and laser correspond, which helps to coarsely set the focus on the surface. For the x-y-calibration, the corresponding fiber can be illuminated by a LED. This helps to prevent confusion of different fibers of the array and to position the structure with micrometer accuracy. For the z-calibration, the fluorescence of the resist is used. The focus is driven from the resist into the surface of the fiber array. As soon as the focus crosses the border from the resist to the surface, the Nanoscribe machine automatically detects the absence of the fluorescence light. To improve adhesion and counterbalance misalignment in the interface finder, the structures are written with a z-offset of 1 µm to 3 µm into the substrate. After the writing process, a developing process of 15 min in propylene glycol methyl ether acetate (PGMEA) is applied with a subsequent cleaning bath of 15 min in isopropanol. After the bath, the structure is rinsed with isopropyl alcohol and dried by pressure air.

5.1.2 Writing Parameters

After the creation of the 3D model, the model has to be sliced into different layers. The layer size can be chosen depending of the required accuracy. In this work layers with minor importance, like the base of the cantilever, are sliced into 100 nm layers. High important structures like optical active surfaces or the tip of the cantilever are sliced in 50 nm layers. This improves the surface quality but also doubles the writing time when writing with the same scanning speed.

For the writing process itself, the two main parameters are scanning speed, which equals the speed of the focus, and the intensity, which can be scaled in the laser scaling factor between

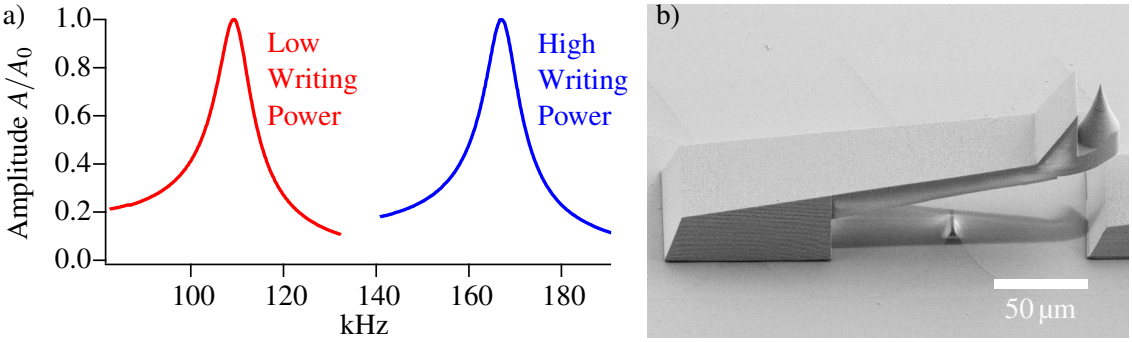

Figure 5.2: **a)** Measurements of the resonance frequency of two cantilevers with the same design. The only difference is the laser power during the writing process which leads to different Young's moduli and thus to different resonance frequencies. **b)** A SEM image of one of those cantilevers.

0 and 1, where 1 means full power of the laser. These parameters have a high impact on the obtained structures. The cross linking of the polymer is influenced by the power of the laser. The higher the power, the more links are broken up simultaneously which results in a higher cross linking. This influences surface roughness, shrinkage as explained in section 5.1.5 and stiffness of the structure as explained in section 5.1.3. To start polymerization, the laser power has to be above the polymerization limit. When the laser power is too high, the destruction limit is reached. This results in spontaneous polymerization chain reactions which are similar to small explosions. When this occurs, small black burned areas are visible in the structure. To find the correct intensity, dosage tests are performed with different laser powers before writing the cantilever.

The second parameter, the scan speed, influences the precision of the writing process. In general, lower writing speed improves the structure precision but directly scales with the writing time. Both parameters, scanning speed and laser power, depend on each other. For a faster writing, a higher laser dose is required since the time of the laser on a certain spot is reduced. To improve optical active areas and small structures like the cantilever tip a low scanning speed of 1 mm/s is chosen and for bulk structures a speed of 10 mm/s.

5.1.3 Tuning the Young's Modulus

3D printing does not only give freedom in form and placement of the structure, the writing process itself is also tunable. To get a stable structure it is typically recommended to write with a laser power near the destruction limit of the resist. This leads to the highest degree of cross linking and thus to the highest Young's modulus. When reducing the intensity, cross linking is reduced which can be used to tune the spring constant as well as resonance frequency as explained in section 2.1.5. To demonstrate this possibility, two identical cantilevers were written on a fiber array. One was written with a laser energy as low as required for photopolymerization and one with the power near the destruction limit of the photo resist. After cleaning, 50 nm of gold were evaporated on top of a 5nm chrome adhesion layer to obtain a good cavity as well as absorption of the driving laser. The cantilever written near the polymerization limit resonated

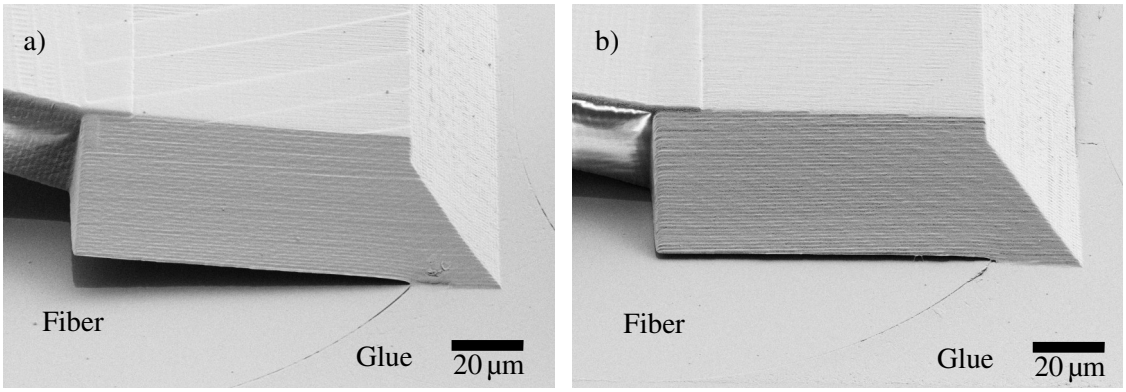

Figure 5.3: Two SEM images of cantilevers written with different powers. **a)** A cantilever written with low power suffers from low adhesion on the single mode fiber which leads to an upbending. **b)** The cantilever written with high intensity shows better adhesion.

at a frequency of 109 kHz whereas the cantilever written with high power resonated at 167 kHz. Since the frequency of a cantilever with one free end grows with the square root of the Young's modulus (see section 2.1.5), the ratio $r = 1.53$ of both frequencies indicates a variance of the Young's modulus of 2.3 when keeping the other variables constant. This gives an additional freedom of fabrication.

5.1.4 Adhesion Control

The fabrication process also has to be controlled to avoid specific problems. One of those problems is that the structures also have to stick to the surface on the desired place since there are no mechanical or chemical bonds. Experience shows that printed structures stick well on rough surfaces but there are problems for smooth surfaces like glass. Figure 5.3 shows a typical behavior of a cantilever partly written on the glue of the fiber array and partly written on the cladding of the fiber. The cantilever sticks well on the glue, but there are problems on the smoother fiber. When writing with low power it is even possible that there is no connection between the structure and the fiber. Upbending processes as explained in section 5.1.5 support this. This changes the distance and the angle of the mirror of the cavity on the cantilever and leads to poor coupling which reduces the signal-to-noise ratio. A high power near the destruction limit of the resist leads to a better adhesion and thus prevents upbending of the base. Even if a low writing power and thus a low Young's modulus is preferred, the first layers should be written with high power to increase adhesion.

Water contamination also reduces the adhesion. Since at room temperature and pressure there is always a water layer on top of surfaces, it also helps to remove this layer. This can be done by a baking process on which the fiber arrays are baked at 150 °C for 30 min. After this, the used resist is dropped on the hot surface to prevent an enclosure of water. The resist then prevents the surface from water contamination.

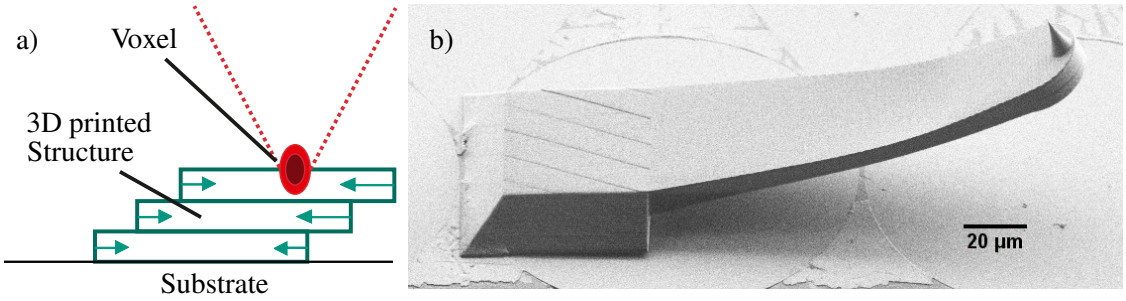

Figure 5.4: **a)** Drawing of the shrinkage process which leads to an upbending. The overhanging layer shrinks more which leads to an upbending of thin cantilevers as depicted in the SEM image **b)**. Adopted from [22].

5.1.5 Upbending of Cantilevers

When printing with 3D printers, there is always a modification of the printed material involved which has side effects. It is a common problem that the printed material has another density than the liquid material. The problem of 'warping', known from macroscopic 3D printers with plastic filament, also occurs with the Nanoscribe system. While the resist is exposed, it shrinks in the range of 0.5 % [166], which leads to internal strain in the layer. On cantilevers this can be well observed because the shrinking layer start to bend the cantilever up. The shrinkage of the overhanging side, which is stronger than the shrinkage of the side where the layer is completely connected to the layer underneath leads to this upbending.

5.2 Working Principle

For optomechanical interaction, fiber facets are able to emit and collect light. Beam shaping lenses, total internal reflection mirrors or reflecting surfaces are easy to print. In combination with a metal coating different solutions for the position readout are possible. The readout can be chosen to be behind, under or before the tip to obtain different sensitivities. The same applies for the actuation. The next sections will explain basic principles and show the wide range of possibilities which can be selected to fit the needs of a certain application.

For fabrication of the freeform cantilevers, a commercially available two-photon polymerization 3D printer was used (Nanoscribe Photonic Professional GT) with an 40x magnification objective and an aperture of 1.4. As resist the commercially available IP-Dip was utilized. For optical active structures like lenses and mirrors, as well as the tip a writing speed of 1 mm/s was used to achieve high accuracy while other parts were written with a speed of 10 mm/s. The laser power was set right below the destruction threshold of the photo resist.

5.2.1 Readout

The readout and tip position can be placed on different positions as depicted in figure 5.5. The basic principle is an interferometric readout as introduced in section 2.1.1. The same fiber is used

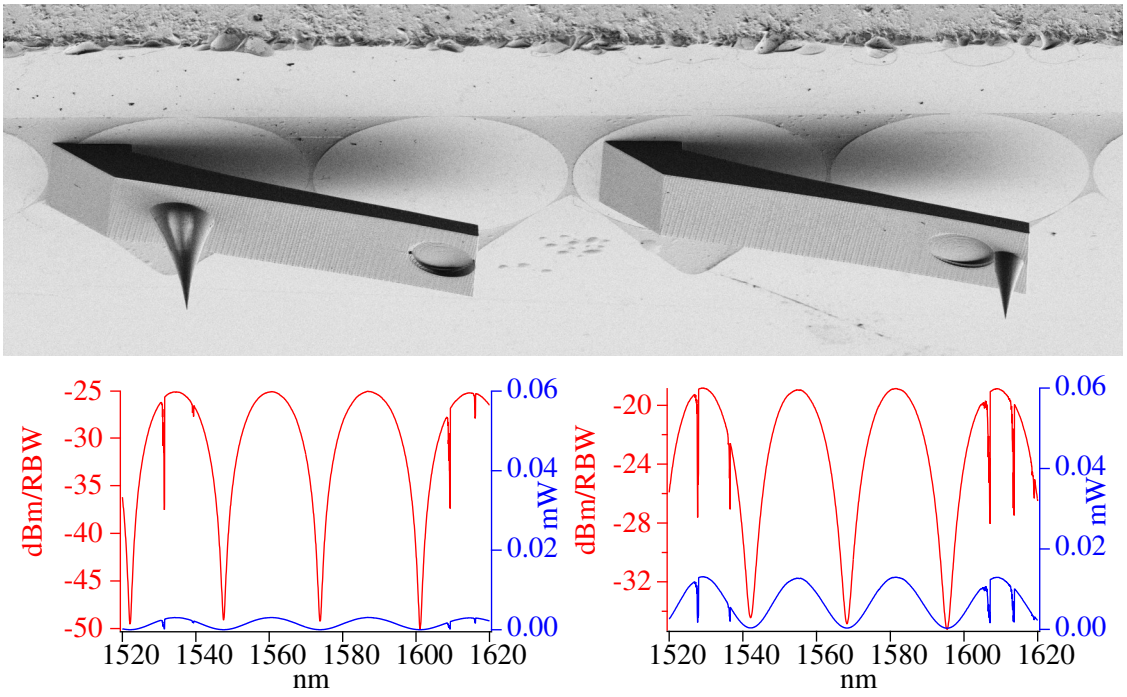

Figure 5.5: SEM image of two different versions of AFM cantilevers without gold coating. The position of the tip and the position of the sensor determine the sensitivity and the maximum measurable distance. The diagrams below the SEM images show the reflected laser power for each cantilever for wavelengths between 1520 nm to 1620 nm. The dBm/RBW values are converted into an emitted laser power in milliwatt on the right y-axis in blue. The fibers have a diameter of 125 µm.

for laser emission and collection and the cavity is formed by the fiber facet and the cantilever. By bending the cantilever, the free spectral range of the cavity formed by a freeform mirror on the cantilever and the fiber facet changes and thus the measured intensity. Depending on the wavelength of the laser, the intensity follows a sine function with a periodicity of the half wavelength for a low reflectivity of the mirrors for a distance sweep of the length of the cavity. For easy control it is helpful to have a linear signal and thus it is recommended to use only 20 % to 30 % of the full range. This would give a usable range of 240 nm when measuring with a wavelength of 1600 nm. This is enough for most cases but can be extended or reduced by using a mechanical reduction by printing the tip further away from the readout. In figure 5.5 two different cantilevers with different reduction factors are shown. Whereas the right one has a ratio of nearly 1 since the detector and the tip are next to each other, the left one has a high sensitivity since a small change at the tip leads to a big distance change at the position sensor. For the position sensor there are also multiple possibilities. Two reflective surfaces are needed for the interferometric readout: one with a fixed distance and one with a distance varying with the deflection of the cantilever. For the reference reflection, the reflection on the fiber facet, which is caused by the change of the refractive index from the fiber-air transition, is chosen. As second reflection, the one of the transition from air to the polymer of the sensor or the transition of the polymer to the air on top of the cantilever can be used. When using the first transition from air to polymer, the top of the cantilever can be designed to form a light exhaust, which refracts the light in a direction, that does not couple back into the fiber when reflected at the sample.

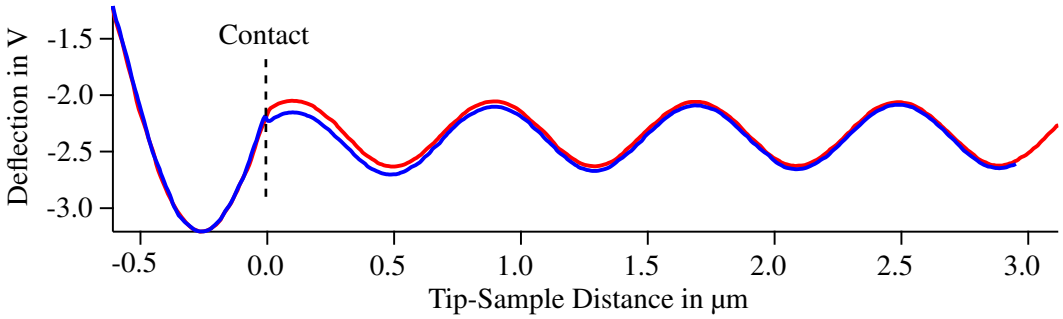

Figure 5.6: Force curve of a printed cantilever without gold coating. The surface reflects enough light into the readout fiber to form an interferometer. This leads to an artificial signal, multiple micrometers before the tip touches the surface.

Figure 5.5 also contains two diagrams of the light collected from the emitting fiber. To measure the reflected energy from the cavity, an external cavity laser with a power of 2 mW and with tunable wavelengths from 1520 nm to 1620 nm is connected to a 3 dB-coupler suitable for broadband operation. For calibration of the energy a gold mirror instead of the fiber array with the printed structures was connected and the reflected energy was measured. The reflected energy of −9.6 dBm was nearly constant over the whole wavelength range and can be converted to 110 µW. A high modulation depth between 18 dB to 25 dB is depicted in figure 5.5.

This is a good solution for a readout when it is assured that no back scattered light from the sample can reach the readout fiber. But since most samples reflect light, this solution needs some improvement. A typical force distance curve of an uncoated cantilever is depicted in figure 5.6. Before the tip comes into contact with the sample, there is already a signal in the deflection due to the secondary cavity formed by the sample and the readout fiber. To prevent this, a metal coating can be applied after the 3D writing process. In this work, 50 nm to 100 nm of gold was evaporated on a 5 nm chrome adhesion layer. The cantilevers were designed to have a freeform mirror on top which was adjusted with the optic simulation tool ZEMAX (OpticStudio) to match the reflectivity of the fiber facet to form a critically coupled cavity. The gold covered structure reflects 6 dB to 12 dB more power back into the photodiode. This makes it easier to measure the distance despite the reduced modulation depth of 4 dB. When comparing figure 5.7 with figure 5.5 it is also conspicuous that the failures in the lower and higher wavelength range do not exist anymore.

To measure with the interferometric readout, it is best to stay in the linear range of the intensity signal. This has two advantages, namely the feedback signal of the cantilever responses linearly, which makes it easier to find proper feedback parameters for the control loop, and it delivers the highest modulation depth since the slope of the sine-wave-like response is the highest there.

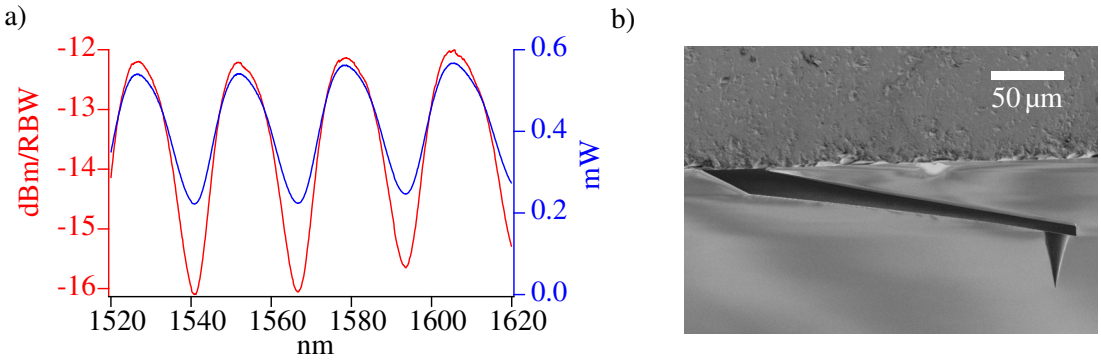

Figure 5.7: **a)** Reflection of the cantilever for different wavelengths. The cantilever depicted in the SEM image **b)** is the same as in figure 5.6 and figure 5.5, but evaporated with 50 nm gold on top of a 5 nm chrome adhesion layer. The power returned from the cavity was converted into milliwatt in blue. The scale is ten times the scale of figure 5.8 and figure 5.5.

5.2.2 Cantilevers with High Finesse Optical Cavity

To further increase the sensitivity, it is possible to increase the reflectivity of the mirrors forming the cavity as presented in chapter 2.1.1. High finesse cantilevers have a very high sensitivity since their quality factor of the dip in the distance dependent signal is high, which leads to a very steep slope. When bending the cantilever, the sensor signal virtually walks along this line and that is why a high change of the signal occurs. When using only the reflection of the fiber facet this is not possible since it only reflects 4 % of the light, which results in high loss of light. To have high reflectance, it is possible to evaporate gold on the fibers before writing the structures. Figure 5.8 shows a measurement of such a cavity. The quality factors of the resonances go up to $Q = 1580$. To calculate the finesse of this resonator, the effective length of the designed cavity is calculated. With a refractive index of the resist of $n = 1.52$ and a thickness of 8.12 µm, the product of those can be added to the lengths of the air cavity with a length of 28.9 µm to obtain the effective length of the cavity of L =41.3 µm. This can be calculated to the free spectral range (FSR) via $\Delta\lambda_{FSR} = \lambda^2/2L = 29.4$. Divided by the full width at half max (FWHM= 1.08) a finesse of 27.2 for the second dip is obtained. The theoretical value for the finesse can be calculated by the reflectance of the gold mirrors. For the semitransparent 20 nm mirror on a fiber the reflectivity of $R_{Au\_20nm} = 0.175$ and for the gold layer on top of the cantilever a reflectivity of $R_{Au\_70nm} = 0.982$ is used. To prevent additional absorption there is no adhesion layer applied. The finesse F can be calculated by:

$$F = \frac{2\pi}{-\ln\left(R_{Au\_20nm} \cdot R_{Au\_70nm}\right)} = 27.5.$$

This value corresponds perfectly with finesse of $F = 27$ acquired from the fit. Remaining errors can be explained by an inaccurate layer thickness of the gold evaporation. The dips of the cavity indicate additionally a FSR of 25 nm and thus a length of the cavity of 46 µm, which can be explained by the upbending of thin cantilevers as explained in section 5.1.

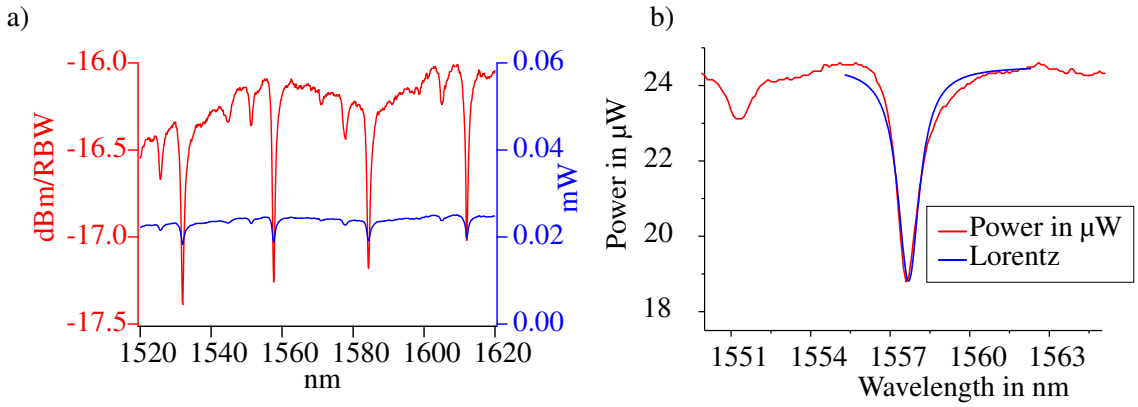

Figure 5.8: **a)** Reflection of a cantilever written on a fiber coated with a semitransparent 20 nm gold layer. The cantilever was covered with 70 nm gold on top for high reflectivity of the freeform mirror. For both layers no adhesion layer was used. The power was converted into milliwatt for an easy comparability with figure 5.7 and figure 5.5. This system leads to many reflections in the cavity and thus to a high quality factor of 1580 which can be obtained from the fit in **b)**. With a designed effective length of the cavity of 41.3 µm this results in a finesse of nearly 27.

5.2.3 Actuation

For the actuation of an AFM cantilever various solutions are possible. Most commercial AFM systems drive the cantilever oscillations with a shake piezo. This is an easy to implement approach but it has some drawbacks:

- The piezo actuates the whole AFM. This introduces unwanted vibrations and reduces signal-to-noise ratio.
- Especially on higher actuation frequencies the resonance frequencies of the piezo introduces resonance peaks which do not belong to the spectrum of the cantilever.
- In liquid environment acoustic modes form, which can cover up the cantilever resonance completely.

These problems limit not only the picking of the right resonance, it also limits the whole measurement. The elements which are mechanically coupled to the shake piezo can influence the deflection signal in a way that the measured amplitude and deflection do not represent the forces acting between the probe and the sample. Especially in frequency modulated AFM, where the phase is held with a control-loop at a fixed value, this can prevent stable cantilever vibration [167]. This is also a common problem in commercial systems and that is why sometimes special equipment is offered, which drives the cantilever in another way. One way to directly drive the cantilever is to use a magnetic field. Besides applying a magnetic field on the cantilever, the cantilever has to interact with this field. Either a specially modified cantilever is used or an alternating current has to be induced at the cantilever as done in Asylum Research's iDrive [168]. A more usable drive is a photothermal excitation [169, 170]. Here, a laser is focused on the cantilever where the absorbed energy leads to a temperature gradient and thus to a deformation of the cantilever. The polymer used for the cantilever is transparent to most wavelengths longer

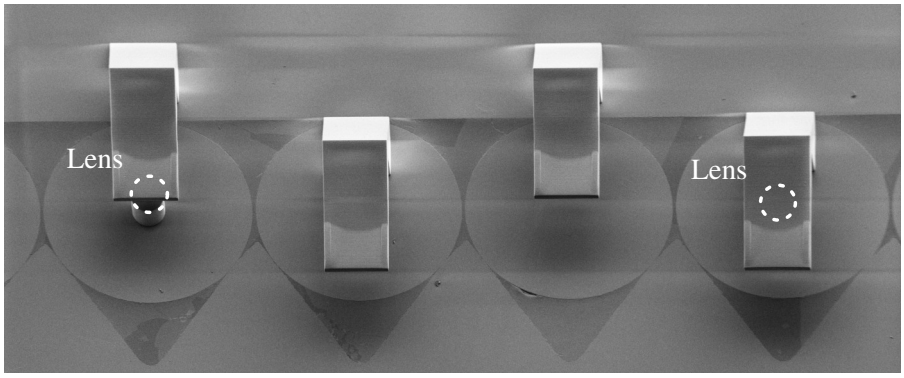

Figure 5.9: SEM image of cantilevers with different actuator positions. Some versions contain a focusing lens. The circular cladding of the fiber has a diameter of 125 µm.

than UV-light which equals the activation energy for photo polymerization. Test measurements have revealed some changes of the cantilever in terms of resonance frequency and stiffness when actuating with a 405 nm laser due to additional cross linking in the resist, even after 30 min of UV-curing. The gold layer on top of the cantilever introduced to shield the readout fiber against reflected light from the sample can be occupied to absorb light with longer wavelengths. These observations led to the idea of photothermal actuation of the cantilever. For maximum amplitude it is best to apply a sinusoidal modulated laser on the base of the cantilever without further focusing. The lenses which were designed to focus the laser in a spot as small as possible did not make any noticeable difference.

5.2.4 Actuation Simulation

To further evaluate the thermal actuation, simulations of the thermal absorption and thermal expansion of the cantilever were performed. To understand the possibilities of thermal actuation, the critical thermal time constant τ is of great importance. This constant is the time the cantilever needs to go from the cool state to the heated state or vice versa. This directly limits the maximum possible drive frequency f_c for which the amplitude of the cantilever reaches its maximum and the heat deviation can follow the applied power of the driving laser. When driving faster than the corner frequency f_c, the cantilever cannot completely heat up or cool down, which results in much lower amplitudes [171]. To compare the simulation and the measurement, the step response of the cantilever was measured. To measure the step response, the actuation laser was stepped from zero to full power with a signal generator while the deflection was measured with the position detector and recorded with the Tektronix TDS 2014 oscilloscope.

Power Absorption

For the simulation, the energy of the heating source has to be determined. The energy for the actuation is derived from the absorbed energy of the laser which has a power of 10 mW. For the absorption, the path of the laser with a wavelength of 785 nm through air and cantilever was

Table 5.1: Table of the parameters used for the simulation. If not other specified, the parameters are taken from the Comsol database.

Material	IP-Dip Resin	Glass	Gold	Chrome	Aluminum
Densitiy ρ [kg/m^3]	1020 [172]	2210			
Young's modulus E [GPa]	3.5 [172]	71.7			
Poisson's ratio ν	0.45 [172]	0.17			
Thermal expansion coefficient α [1/K]	$5.0 \cdot 10^{-5}$ [173]	$5.5 \cdot 10^{-7}$			
Emissivity ε	0.91	0.93 [174]	0.47 [175]		
Refractive index n	1.52 [103]	1.5	0.149 [176]	3.134 [176]	2.693 [177]
Extinction coefficient k	0	0	4.783 [176]	3.447 [176]	8.438 [177]

modeled as a cube of air with a subsequent cube of IP-Dip resin, each with a length of 500 nm, a 5 nm chromium adhesion layer and a subsequent 100 nm gold layer. The size of the cubes was of minor importance since the absorption of both layers is negligible, but they have to be included into the simulation due to the reflection which occurs on the transition between layers with different refraction indices. The model was simulated with Comsols wave optics module (electromagnetic waves, frequency domain). For the simulation, a defined magnetic field was first set in y-direction and then a defined electric field was set in y-direction at port 1. The angle of incidence was perpendicular to the surface for both. Floquet periodic conditions were applied on one side of the structure to take into account that the volume can be expanded in xy-direction. The simulated wave is excited at the top of the cube and propagates through the adhesion layer and the gold coating. The transmission and reflection are calculated by the transmitted and reflected intensity of the bottom of the structure. As a result, the cantilever absorbs 15.8 % of the laser light, which equals 1.58 mW when using the maximum 10 mW of the actuation laser.

Thermal Expansion

For the simulation of the cantilever response, the thermal heat source was modeled to have a Gaussian profile with a mode-field diameter of 20 µm at $1/e^2$-intensity with a standard deviation of 10 µm. The total power is derived from the power absorption simulation and is nominally 1.58 mW. To include the thermal influence of the expansion of the gold layer on top of the cantilever, the built-in boundary condition 'thin layer' of Comsol was used and set to 100 nm and the properties were set up to match the material properties of gold. For the heat transfer of the structure a quartz cuboid substrate was added underneath the structure to simulate the fiber array. The thermal conductance between the structure and the cuboid was varied to match the

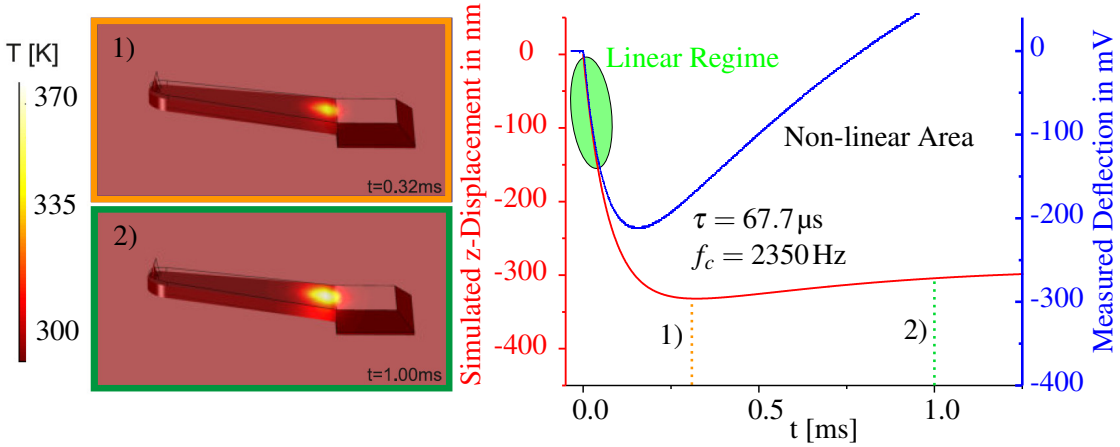

Figure 5.10: Simulated and measured response of the 3D printed AFM-cantilever upon sudden heating. The simulation as well as the measurement with the interferometric readout show a downbending of the cantilever due to the high temperature gradient when switching on the actuator laser. This bending is strong enough that the linear regime of the readout is left. When the heat dissipates into the cantilever, the gradient decreases which leads to a back bending of the cantilever. Simultaneously the cantilever elongates, which leads to worse coupling and thus further reduces the obtained signal.

measured response to determine the actual heat transfer. As a result it could be determined that the thermal conduction to the fiber array is of no importance and the best fitting was obtained for a gap conductance of zero. This is counterintuitive since one would expect thermal conductance to the fiber as the main cooling process. An explanation of this might be the adhesion problem discussed in section 5.1.4. In combination with the shrinkage discussed in section 5.1.5, this could lead to partial detached areas where the cantilever base has no direct contact to the glass fiber. This would prevent a high conductance through the fiber array since a gap between the cantilever and the fiber array would act as insulator. Another explanation might be that at room temperature and pressure the thin water layer on top of the array mixes with the resist which would lead to a lower density in the resist near the fiber array which would also limit the heat transfer.

The simulation as well as the measurement show principally the same behavior of the cantilever. It can be divided into two processes whereas the first one leads to a downbending and the second one to an upbending of the cantilever. For the measurement it has to be considered that the response of the cantilever is acquired with the interference-based readout. The ideal response of this readout for low reflectivity has the form of a sine wave for a distance sweep and should only be operated in the linear regime. As the bending of the cantilever exceeds this linear regime, a nonlinear behavior of the readout has to be taken into account. The first process leads to a fast downbending of the cantilever due to the thermal expansion of the top of the cantilever. At the beginning, the temperature gradient is very high since the lower part of the cantilever is at room temperature and the laser acts only at the top side of the cantilever. Due to the thermal conductance of the cantilever, the heat starts to spread over the cantilever which leads to a smaller heat gradient. The cantilever now also expands at the bottom side which leads to lesser bending. This behavior is shown in the simulation as well as in the measurement. The measurement seems to have a much stronger back bending of the cantilever than in the simulation but it has to be

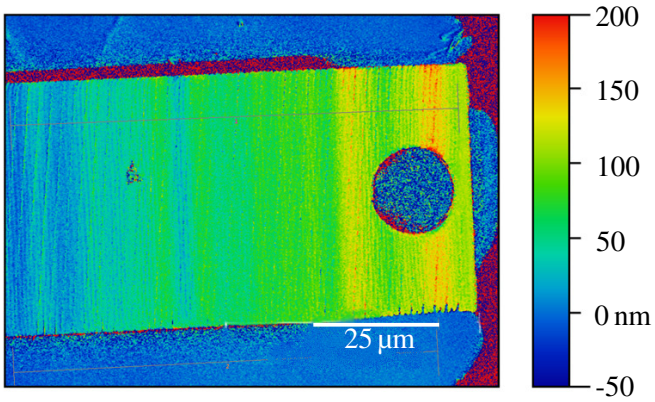

Figure 5.11: Differential VSI measurement of a cantilever before and after applying 5 mW at the actuator fiber. The tip shows a height difference of 140 nm. This property can be used to compensate fabrication errors or can be used for z-actuation.

taken into account that the heated cantilever is bent and elongated which leads to a shifted optical axis between the fiber facet and the mirror at the cantilever which reduces the signal obtained from the optical readout.

It is obvious that after a while a new equilibrium state will settle, where the laser induced heat equals the discharged one. Apart from the possibility of dynamically shaking the cantilever, it is now possible to control the height of the cantilever by a laser intensity offset.

This can be useful for different situations. One is that this can be used for the z-feedback of the scanning system. This would save the piezo used for the compensation of the topography when scanning over a sample. Another aim is to have multiple cantilevers at one system [178, 179]. The production of such cantilevers suffers from multiple problems. One is the alignment of these cantilevers, which optimally differ less than 1 µm in height to prevent too much force on one cantilever. Additionally, every cantilever should have its own z-positioning system like an integrated piezoelectric actuator [180] to be able to measure higher topography. Here, the laser power could be used for the feedback.

To measure the offset of the cantilever without the distortion of the resulting misalignment between the fiber facet and the mirror, a white light interferometer was used (Bruker ContourGT-K with 50X magnification). After loading the cantilever into the vertical scanning interferometer (VSI), the sample was aligned vertically. The system was set to measure two times and display the difference between both measurements. After the first measurements, the actuation laser was activated with a power of 5 mW and the second measurement was performed. As a result the image in figure 5.11 was obtained. The cantilever tip bent up to 140 nm in respect to the surface of the fiber array, which did not move as expected. This correlates excellently with the simulation results from figure 5.10 which indicates a deflection in the range of 300 nm for the double laser power of 10 mW.

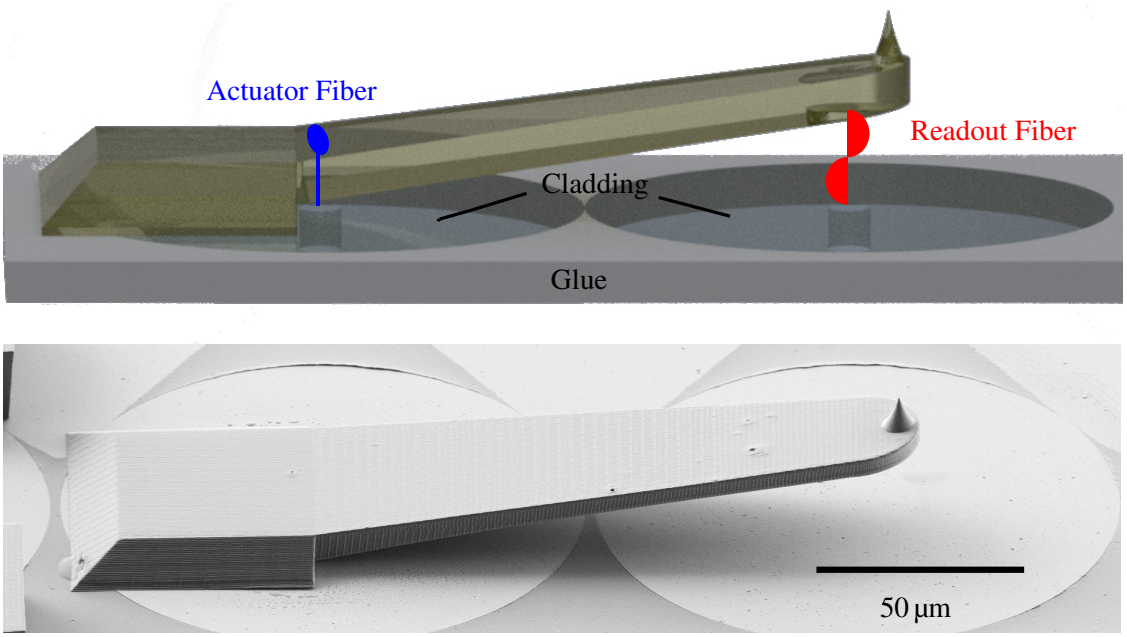

Figure 5.12: Scheme and SEM image of an atomic force microscopy cantilever for dynamic mode. The cantilever uses two fibers of a fiber array; one for thermal actuation and one for an interferometric readout.

5.3 The Standard Polymer AFM Cantilever

As described in chapter 5.2.4 and chapter 5.2.4, all elements for the assembly were identified and well characterized. Despite the fact of completely freedom of forming a cantilever it was decided to basically adopt the form of traditional cantilevers. This shape is proven to work and there is plenty of literature about the theory of the oscillation and bending behavior. This restriction still has enough freedom to improve the used system but gives a guideline for orientation.

The basic version of the 3D printed cantilever is depicted in figure 5.12. It uses two fibers, one for thermal actuation and one for the interferometric readout. The cantilever itself has a rectangular form with rounded edges for better production. The tip is next to the readout fiber to have no mechanical reduction between the readout and the tip in order to have a calibration free cantilever as explained in section 5.6. To reflect the light from the readout fiber, a freeform mirror was calculated with Zemax to obtain a critically coupled cavity as explained in section 5.2.1

To improve the adhesion on the cantilever, it was written on a base which has a square area which is narrowing. The actuator fiber is located directly under the origin of the cantilever on the base to obtain maximum deflection of the cantilever and thus maximum amplitude at the tip. The cantilever itself has a tilt of 13° to assure that the tip interacts with the sample and not with any other part of the cantilever with a protruding feature of the sample.

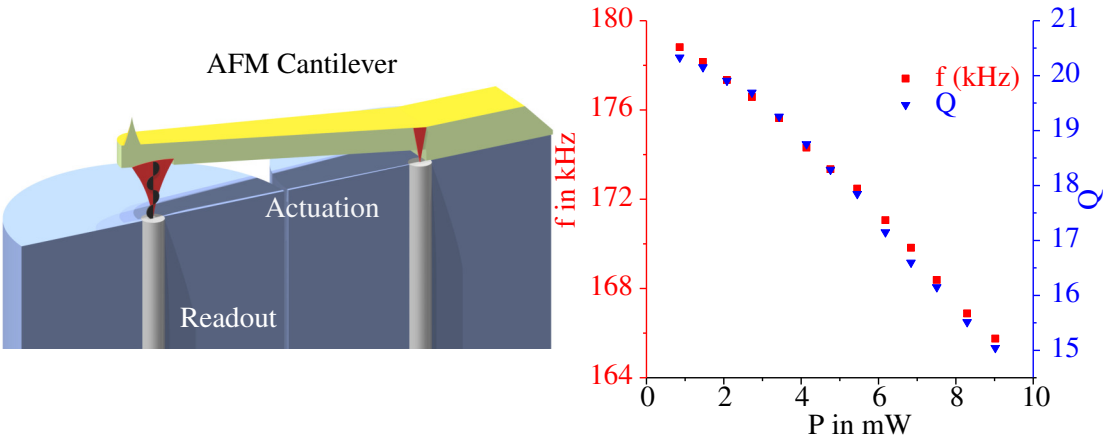

Figure 5.13: To actuate the cantilever, a laser is modulated with a sine wave voltage at resonance frequency. The power oscillates with an amplitude around an offset value. By increasing the offset, the cantilever heats up, which makes it softer and results in a lower resonance frequency and a decreased quality factor. This effect can be used to tune the resonance frequency over a wide range.

5.4 Tuning the Resonance Frequency

Now the laser actuator is used to influence the mechanical properties of the cantilever. Taking the absorbed power from the laser into account, the temperature of the cantilever rises when increasing the laser power. This temperature change also affects the Young's modulus as it decreases due to the higher mobility of the polymer chains [181][182, p. 54ff]. Since the resonance frequency of a cantilever depends on the square root of the Young's modulus, the resonance frequency can be tuned by tuning the laser power.

As explained in the previous chapter, a predefined, single resonance frequency is favored by industry as well as in research since it simplifies the setup and enables parallelized measurements with having only one actuation laser and one multiplexed lock-in amplifier.

Since the absorbed energy is responsible for the change in the Young's modulus, a high absorption is desired. To obtain a high absorption of the laser, a 100 nm thick gold layer was evaporated on a 5 nm chrome adhesion layer. The standard type cantilever was used as schematically depicted in figure 5.13. The actuation of the cantilever was accomplished by utilizing the actuation fiber. The readout fiber was used to form a cavity with the mirror near the tip of the cantilever. To tune the cantilever, an amplitude of 1 mW was used and an offset up to 9 mW was subsequently applied in steps around 0.6 mW. As readout the interferometric readout fiber was utilized. To find the resonance frequency, the modulation signal was swept around the expected resonance frequency of 200 kHz with the Asylum Research controller. The software automatically detects the peak of the obtained Lorentz curve and also calculates the quality factor of the oscillation. The resonance frequency of the cantilever without applying an offset was measured to be 180.8 kHz. As a result, the resonance frequency could be nearly linearly tuned from 178.8 kHz to 165.8 kHz, which enables compensating an inaccuracy in the range of 15 kHz, which equals around 8 % of the resonance frequency in lower direction. The quality factor, which can also be of interest especially in respect of scanning speed, can also be tuned in the range of $Q = 20$ to $Q = 15$. When

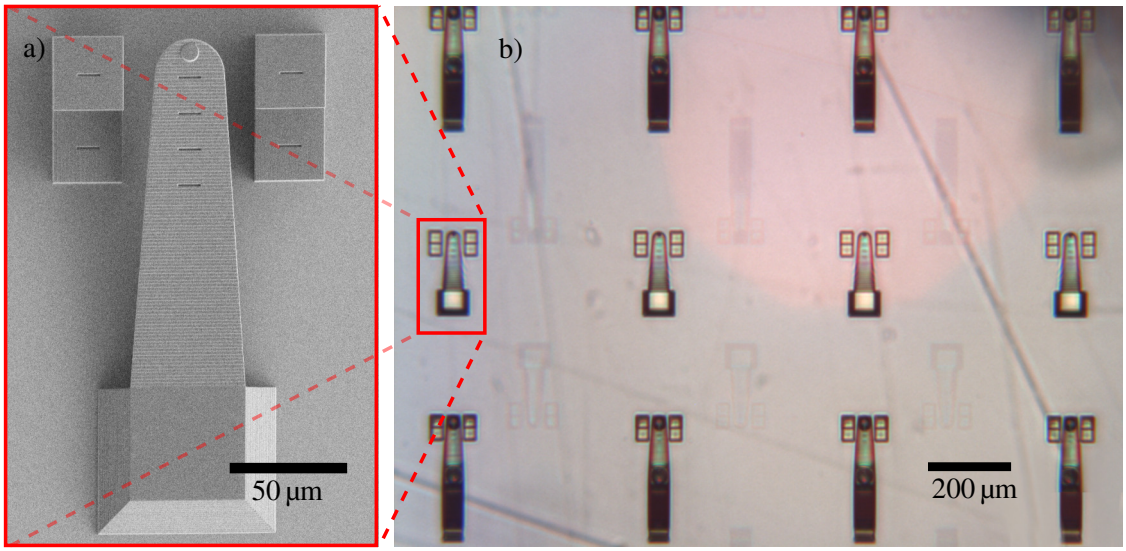

Figure 5.14: **a)** SEM image of one AFM cantilever of the array. **b)** An optical microscope image of a part of the array. The tip was left out to save time. Blocks are written next to each cantilever to evaluate the shrinkage of the cantilevers.

fitting with a linear slope, a change of the resonance frequency of $-1.63\,\mathrm{kHz/mW}$ and a change of the quality factor of $-0.7/\mathrm{mW}$ can be calculated.

5.5 Reproducibility

To use multiple cantilevers in one measurement, which opens the perspective for parallel measurements, reproducibility is a key factor. The standard etching processes allow the production of cantilevers with large variances of important properties like resonance frequency or spring constant in the range of 30 % [5, 6]. This inherently inhibits simultaneous measurements in dynamic mode, if not one lock-in amplifier per cantilever is provided. The only possibility up to now is to use the much noisier contact mode, which incorporates high forces. The possibility to measure with multiple channels is easy to accomplish when using a commercially available fiber array [183], which can even be fabricated by hand [184]. Those fiber arrays are one- or two-dimensional arrangement of fibers with high precision. A 8×8-array with a pitch of 127 µm can easily scan an area of $1\,\mathrm{mm}^2$ by moving only 127 µm in x- and y-direction. Thus for the fabrication two properties are of interest. One is the resonance frequency, which should not vary much to be able to use one actuation laser and one lock-in amplifier which can be multiplexed, and the second one is the height of the cantilever over the fiber facet because this determines the wavelength on which the readout has its highest sensitivity as explained in chapter 5.2.1.

5.5.1 Resonance Frequency Deviation

To determine the reproducibility of the 3D printing process, a large array of AFM-cantilevers was written on a quartz substrate. Images are provided in figure 5.14. On this array, 71 AFM

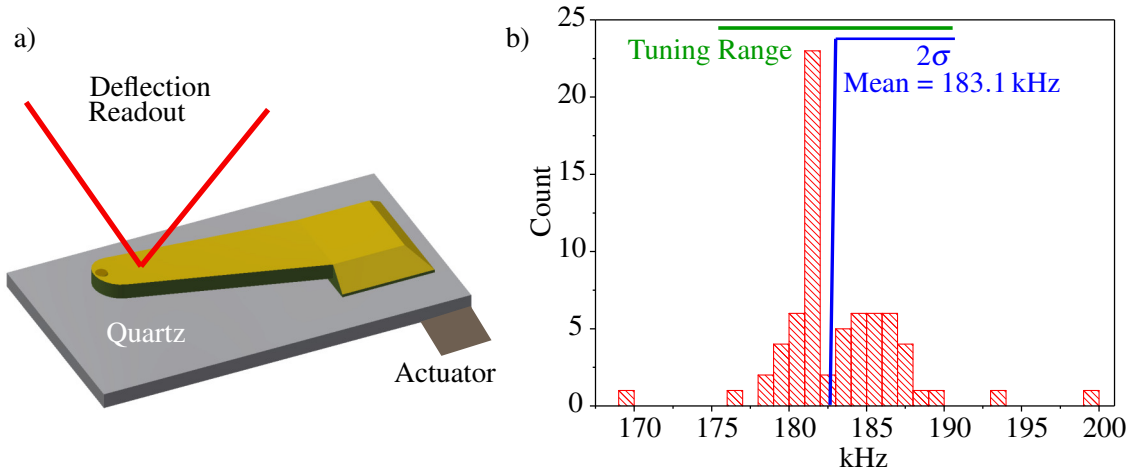

Figure 5.15: **a)** Scheme of the readout and the actuation for this measurement. **b)** A histogram of the acquired resonance frequencies of 70 AFM cantilever. The thermal tuning range is also plotted. The tuning range allows to tune 95 % of all fabricated cantilevers to oscillate at the same resonance frequency.

cantilevers were written as well as 69 SNOM cantilevers. To determine the resonance frequency of all these cantilevers, the whole quartz substrate was glued on an adapter which was originally used to electrically connect to TMR-sensors. For the AFM a holder exists, where this whole adapter can be inserted. The adapter is clamped with plastic clamps on top of a shake piezo. With this piezo the whole substrate was shaken by sweeping 100 kHz around the expected resonance frequency. To readout a single cantilever, the laser of the AFM was focused on the respective cantilever and the reflected light was collected by a split photodiode as in conventional AFM. A schematic of the setup is provided in figure 5.15. In order to have a high reflectance, the cantilevers were coated with a 5 nm chromium layer followed by a 100 nm gold layer. The cantilevers themselves were written with a slicing distance of 200 nm to be able to fabricate the array in reasonable time.

Seventy AFM cantilevers were measured and had a mean value of 183 kHz and a standard deviation of σ =3.9 kHz. Considering the possibility of thermally tune the cantilever resonance frequency in the range of 15 kHz, as presented in the last section, it is possible to compensate fabrication errors in the range of 2σ. With that, 95 % of all produced cantilevers can be shifted to the desired resonance frequency.

5.5.2 Height Deviation

Besides the resonance frequency, the height of the cantilever is of special interest. The readout laser has to have a certain wavelength to ensure high sensitivity of the system. This wavelength directly depends on the distance between the fiber facet and the cantilever mirror as explained in section 5.2.1. To be able to use only one wavelength for multiple cantilevers, the length of the cavity has to have only little deviation. Ideally the cantilever tips should exceed the same height to minimize the forces applied to the surface.

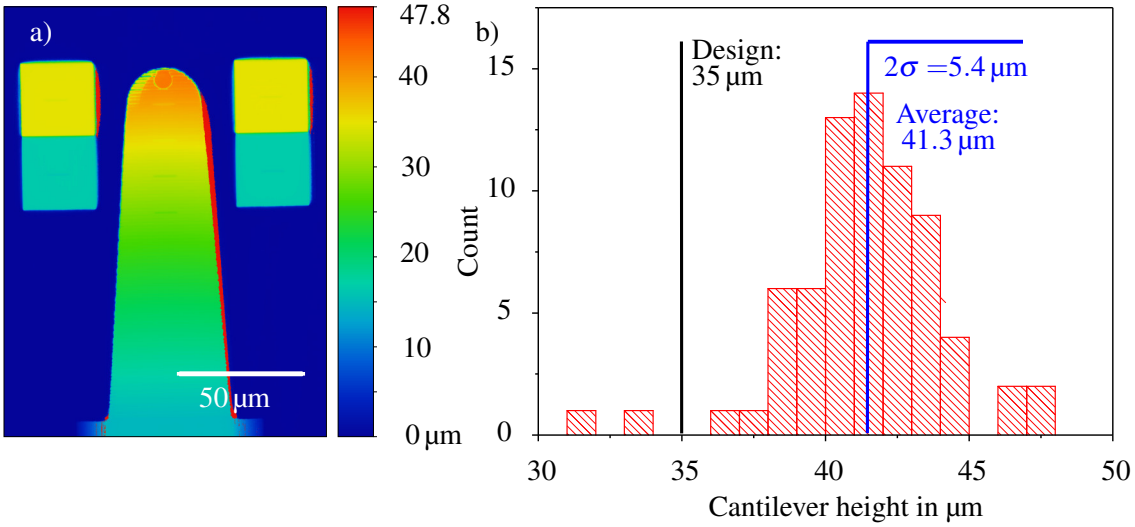

Figure 5.16: **a)** VSI image of a measured cantilever. **b)** A histogram of 70 cantilevers. The cantilevers show a significant shift between the designed and the measured height due to upbending.

The same array of cantilevers used to determine the deviation of the resonance frequency shown in figure 5.14 in the previous chapter were also used to determine the deviation in cantilever height. To measure the height, whose deviation is preeminently caused by the upbending of the cantilever during and shortly after the writing process as explained in chapter 5.1.5, reference blocks were written next to the cantilevers. Further, the cantilevers were cut off in the same plane as the height of those blocks. To evaluate shrinkage, the reference blocks as well as the cantilevers were equipped with reference lines. To measure the height difference between the blocks and the cantilevers, a VSI (Bruker ContourGT-K with 50x magnification) was utilized.

The measurement revealed a significant deviation between the designed height and the measured height. The cantilevers were designed to be 35 µm above the surface as the calibration block besides the cantilever. Since the calibration blocks accord well with the design parameters, the deviation of σ =2.7 µm can be explained by an upbending of the cantilever as discussed in section 5.1.5. The shrinkage of the layer, which causes the upbending highly depends on writing speed, dose and geometry. In chapter 6.5.2 some solutions to reduce this upbending are presented.

5.5.3 Predetermination of the Resonance Frequency

This directly leads to the question of how accurately the resonance frequency can be predetermined. There is a difference of reproducibility in terms of how the resonance frequency is distributed and how well the desired frequency matches the obtained one. When designing a cantilever, the first design parameters are constrained by the desired optical features like readout or actuation. Those have to fit the properties of the fibers from the fiber array. After this procedure, there is nearly no limitation when designing the cantilever. Therefore a standard model was used as AFM Cantilever in this work, which was adapted to the intended use. To estimate the

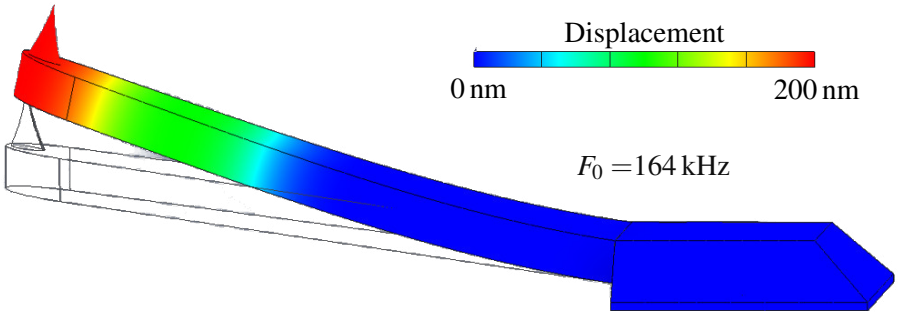

Figure 5.17: Simulation with Autodesk Inventor to obtain the resonance frequency. The image additionally shows displacement in color scale.

resonance frequency, simulations were performed with Autodesk Inventor. The design files were already created in this software, which made it easy to get resonance frequencies after specifying material properties like Young's modulus E =3.5 GPa, Poissons ratio ν =0.45 and density ρ =1020 kg/m^3 [172].

At first, the resonance frequency of 164 kHz was obtained. This is only a deviation of 15 kHz to the measured 179 kHz. This can be explained by the dose dependent variation of the Young's modulus. The density was set to be fixed in the simulation since the volume of the resist does not change that much. The Young's modulus was calculated to be 4.16 GPa which is plausible since the cantilevers were written with a laser power near the destruction limit to have high cross linking as well as high adhesion on the fiber array. This example shows that within certain limits it is possible to predetermine the resonance frequency of a newly designed cantilever.

5.6 Calibration of Cantilevers

A typical problem for a classical AFM setup is calibration. After inserting the cantilever and the aligning process of the laser and photodiode, the measurement cannot start directly. First the setup has to be calibrated. The current from the photodiode is transformed into a voltage by a transimpedance amplifier setup with a fixed gain. But due to a different beam position or a difference in reflectivity of the cantilever, the current varies and thus does the measured voltage. To calibrate the AFM, a force distance curve has to be measured on which the cantilever is pressed with the tip against a hard surface. The traveled distance of the z-piezo and the measured signal can be used to calibrate the deflection value. During this process the tip can already be damaged, contaminated or blunted. The polymer cantilevers with their interferometric readout mechanism allow a touchless calibration procedure:

When tuning the readout laser to different wavelengths, the free spectral range can be calculated with two acquired points and thus it is possible to exactly know how far away the cantilever is from the fiber facet as explained in chapter 2.1.1. This means that the length of the cavity, and thus with the given wavelength the relationship between the acquired photo current and the change of distance, can easily be calculated without touching the sample.

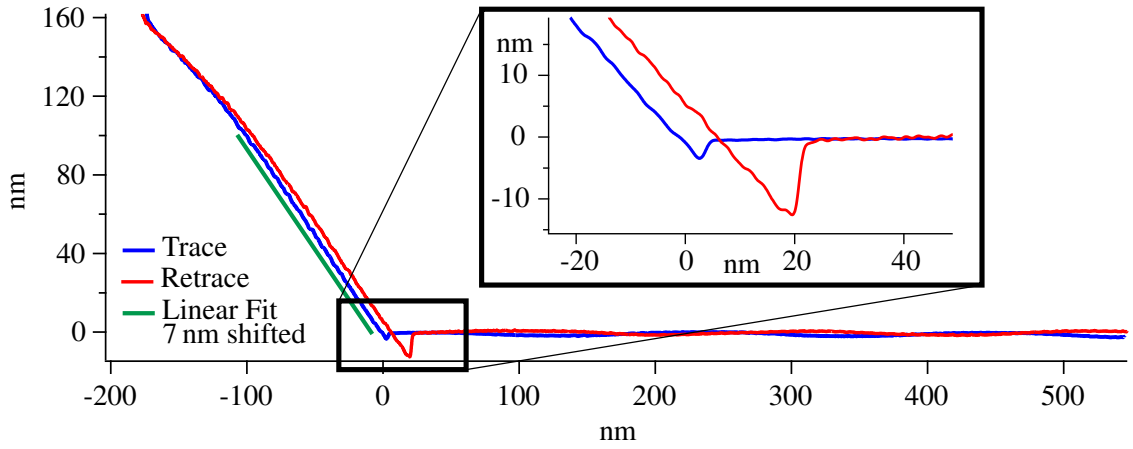

Figure 5.18: Force curve of the standard AFM cantilever. Trace and Retrace differ slightly due to elastoplastic deformation of the cantilever and tip. The zoom-in reveals high sensitivity since the snap-in is clearly visible. The fit in green to determine the sensitivity was shifted 7 nm to the left side to simplify differentiation of the plots.

For further advanced AFM modes like multifrequency mode this also gives an additional advantage. The sensitivity of a beam deflection readout highly depends on the position and size of the laser. This can lead to a complete suppression of a mode of interest [85]. The 3D printed cantilevers can be positioned with micrometer accuracy and thus it is possible to avoid this problem.

When measuring with the cantilever, the displacement of the cavity does not match the displacement of the tip since the tip is in a certain distance to the mirror of the cavity to reduce back scattering from the sample. This leads to a mechanical reduction factor. This factor depends on the form of the deformation of the cantilever and it can be distinguished between the static deformation factor δ_{static} and the dynamic deformation factor $\delta_{dynamic}$. When measuring a force distance curve, only the static deformation factor is calibrated. When information about the amplitude in dynamic mode is required, the calibration factor $\delta_{cal} = \frac{\delta_{static}}{\delta_{dynamic}}$ is used. This factor is also known in classical AFM setups and typically set there to 1.09 [86]. For the polymer AFM cantilever both deformation factors were simulated to be:

$$\delta_{static} = 1.26,$$
$$\delta_{dynamic} = 1.21,$$

which directly leads to the calibration factor $\delta_{cal} = 1.05$. Due to the low geometrical variations in cantilever fabrication, it is sufficient to measure a force distance curve once for one type of cantilever to calibrate the MR factor. All other cantilevers have the same and do not have to be calibrated again. A typical force curve acquired with the standard AFM cantilever is depicted in figure 5.18.

The force curve looks similar to the one acquired with the beam deflection readout on a silicon cantilever. Only slight differences are visible. One is that the deflection is not completely linear, it starts to bend a little bit. This can easily be explained by the readout. With the interferometric

readout, the deflection has the form of a sine wave as explained in 5.2.1. The force curve was only performed for a few hundred nanometers to stay in the linear regime. The green line in the figure is the linear fit to set the sensitivity, but it was shifted 7 nm to the left to allow to distinguish between the trace, retrace and the fit. Additionally, a shift between the trace and the retrace is visible. This can be explained by elastoplastic deformation of the cantilever and tip. the cantilever was designed to have high resonance frequency as well as high spring constant. This is necessary in order to have good sensitivity and enables high measurement speed in dynamic mode. When performing a force curve, this means that the applied force is orders of magnitudes above the one applied when using a cantilever made for contact mode.

In order to calculate the mechanical reduction factor δ_{static}, a fit with a sine wave was performed on the deflection. The fit returned an $\omega = 6.56 \cdot 10^6/\mathrm{m}$. To calculate δ_{static}, formula 2.3 can be used:

$$\delta_{static} = \frac{2 \cdot \Delta z}{\lambda} = \frac{2 \cdot \frac{2\pi}{\omega}}{\lambda} = 1.24$$

with the wavelength $\lambda = 1550\,\mathrm{nm}$. This excellently fits the simulated value of $\delta_{static} = 1.26$. To measure in dynamic mode, the calibration factor $\delta_{cal} = 1.05$ has to be taken into account to consider the different form of the cantilever in dynamic and static mode.

5.7 AFM Measurements with Polymer Cantilevers

As described in chapter 5.1.1-5.5.3, the cantilever is well defined in terms of fabrication, actuation, optical readout system and displacement behavior. The following measurements show the potential of the developed system. All measurements were performed within the AFM system presented in chapter 2.1, with a piezo stage (Physik Instrumente GmbH & Co. KG) for xy-movement of the sample with a scan range of 800 µm in each direction and a z-piezo with a throw of 100 µm. As AFM controller the ARC2 (Asylum Research) was utilized, which provided the feedback signals as well as analog to digital and vice versa data converting. The AFM was damped by an active vibration isolation table (Halcyonics Micro 40). As modulation laser for the actuation, the laser diode driver (Newport Model505) was supported by the ILX Lightwave LDT-5910B temperature controller. As tunable laser for the readout, the Santec Tunable Semiconductor Laser TSL-210 was used. To convert the light intensity into a voltage, the Agilent 8163A Lightwave Multimeter was utilized. Before every measurement the hood was closed to prevent eye injuries and both lasers, for readout and actuation, were switched on and a few minutes were granted for the cantilever to reach thermal equilibrium. After this, the wavelength of the interferometric readout was swept to acquire the maximal and minimal photo current which equals the maximum and minimum light returned from the cavity. After this procedure, the wavelength was adjusted to return a current in the middle between the two extrema. Then the resonance frequency was determined by sweeping the modulation frequency of the actuation laser in the range of the designed resonance frequency. The modulation frequency was set to reach an amplitude of 97 % of the maximum free air amplitude to stay in the repulsive regime. Then the wavelength of

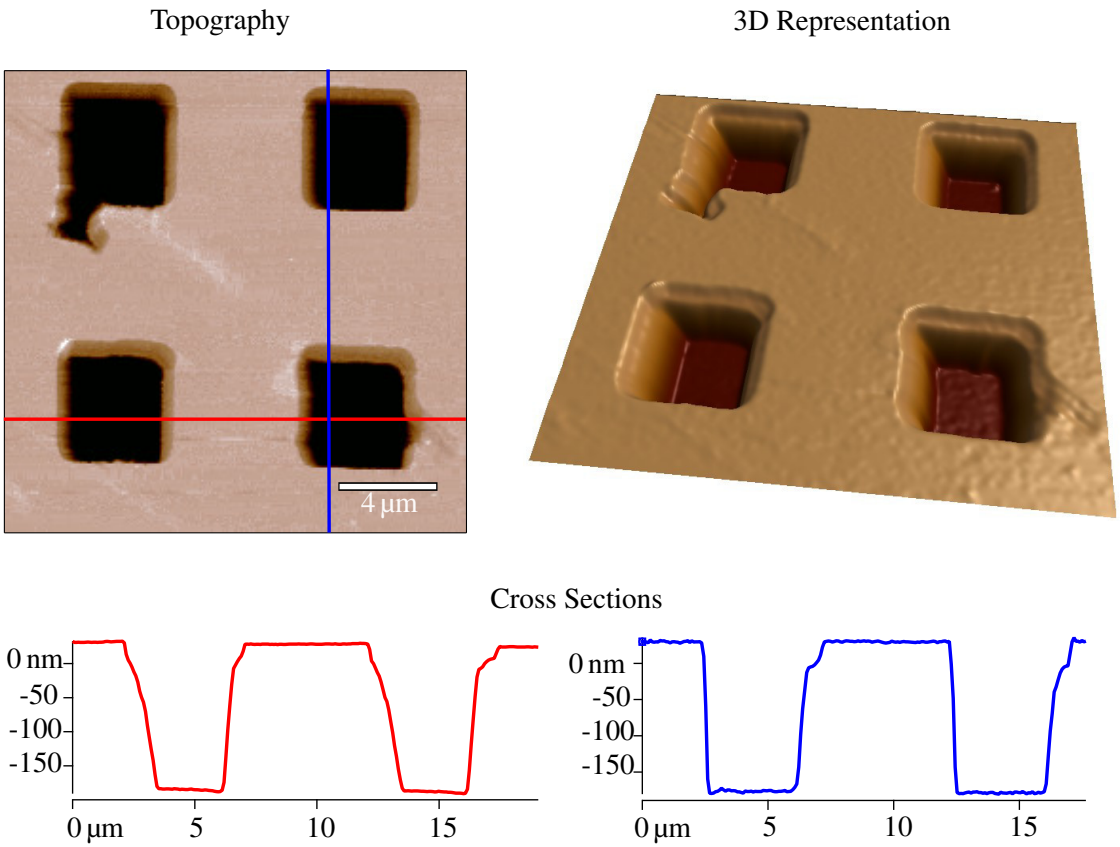

Figure 5.19: First AFM measurement with the standard AFM cantilever. The silicon test grating is clearly scanned and no artifacts are visible.

the readout laser was manually fine-tuned to return the highest amplitude. Then the AFM could be used as any other conventional AFM.

To demonstrate the ability of the system, different measurements were performed with the focus on different properties. When not mentioned otherwise, the standard AFM cantilever was used.

5.7.1 Proof of Concept

This was actually the first measurement performed with the polymer cantilever with the interferometric readout. A grating is typically used to test the calibration of the AFM. The silicon calibration grid has a pitch of 10 µm and has squares etched in with a depth of 200 nm and an edge length of 4 µm. During the measurement the AFM behavior was comparable to a normal AFM. The acquired data presented in figure 5.19 do not show any conspicuousness in terms of overshootings or artifacts.

This measurement was proof that the system works as designed, but is mainly included in this work for a sentimental reason, since this was the measurement that encouraged us to invest more time into this promising project.

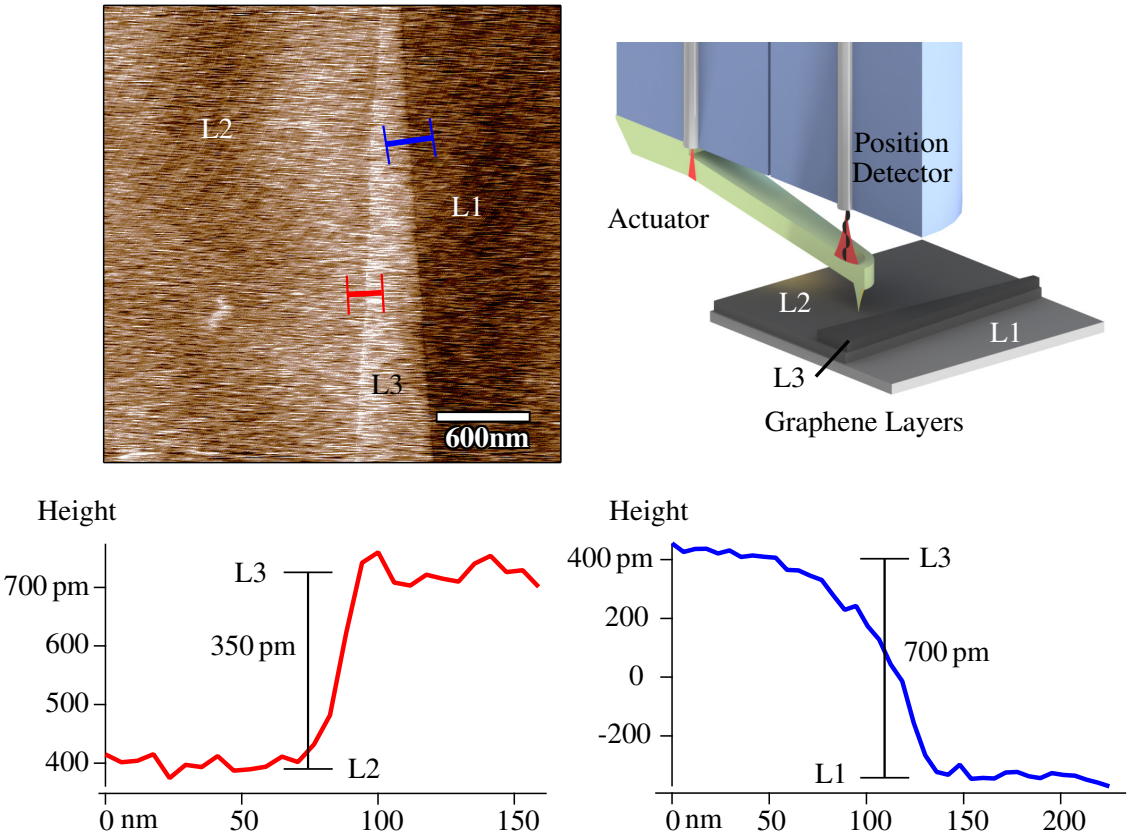

Figure 5.20: AFM measurement on a freshly cleaved HOPG surface. Clearly 3 different layers, L1-L3 are visible as depicted in the scheme. The steps in the cross sections match the literature values for graphene layers.

5.7.2 Atomic Resolution

High resolution measurements are the discipline in AFM that needs the highest sensitivity. For the high resolution demonstration, the smallest accessible samples were used: Atoms. The measurement of atomic steps was used to demonstrate the excellent vertical resolution of the sensor system. To have a clean sample, a freshly cleaved highly oriented pyrolytic graphite (HOPG) was used.

On the measurement depicted in figure 5.20 clearly three layers with different heights are distinguishable. The depicted cross sections show steps with a height of 350 pm on the single step and a height of 700 pm on the double step. This is well in accordance to 335 pm mentioned in literature [185]. Thus, the system is able to measure down to the atomic range. The remaining noise in the image can be explained by the laser noise of the wavelength and intensity. The readout laser contains an external cavity to tune the laser wavelength, which is also sensitive to vibrations. Nevertheless, such a tunable laser is the best choice for the readout since it makes it possible to work at the wavelength with the highest sensitivity. Furthermore, the stage used for the x- and y-movement has a big range of 800 µm × 800 µm, which is not conceivable for atomic resolution.

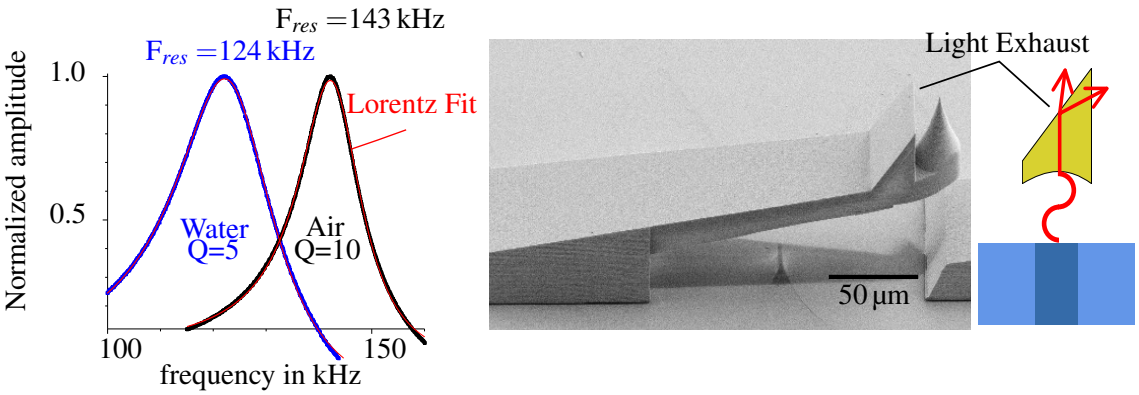

Figure 5.21: Two measured resonance curves of the cantilever of the SEM image, one curve measured in water and one in air. The cantilever is equipped with a light exhaust, to prevent that light reflected from the sample can couple back into the readout fiber.

5.7.3 Measurement in Water

An additional field of use are in situ measurements in liquid environment. More accurately, the environment itself can change without disturbing the measurement. To perform a measurement in liquid, typically additional accessories are used like a closed fluid cell. This cell encapsulates the sample and the cantilever but has windows to let the laser from the deflection readout enter the cell, which allows the reflected beam to reach the split photodiode. This cell is important to protect the electronics and other parts sensitive to liquid like the actuation piezo [161] from destruction. Further, it is not possible to measure successively in air and water for example, without starting a new realignment process. The different refractive indices refract the light differently, which results in a new alignment of the laser pointing at the cantilever as well as the photodiode. Additionally to the displacement of the laser, a new calibration process has to be performed to be able to convert the acquired photocurrent from the photodiode into a distance. The 3D printed approach only has a cavity in which the light is reflected between the two ends of the cavity. Besides the different intensities in the cavity for different environments due to the different transitions of the light when leaving the fiber facet and the wavelengths in the medium, nothing else changes.

In preliminary experiments difficulties appeared when engaging the tip of the cantilever to a reflective surface due to light reflected into the readout fiber. This effect increases in liquid environments due to the smaller difference in refractive indices between cantilever and water. To evaluate that theory, a copper oxide sample which absorbs nearly all the light in the infrared region was used and the effect nearly vanished. To overcome this problem, a light exhaust was introduced above the readout fiber which refracts the light not reflected by the cantilever, so that it cannot be reflected back from the sample surface into the fiber.

For demonstration, a grating was measured in air, and subsequently in water. The grating was glued with epoxy into a vessel to prevent the grating from floating away when pouring the water in. Before every measurement, the resonance frequency was acquired since there is a change

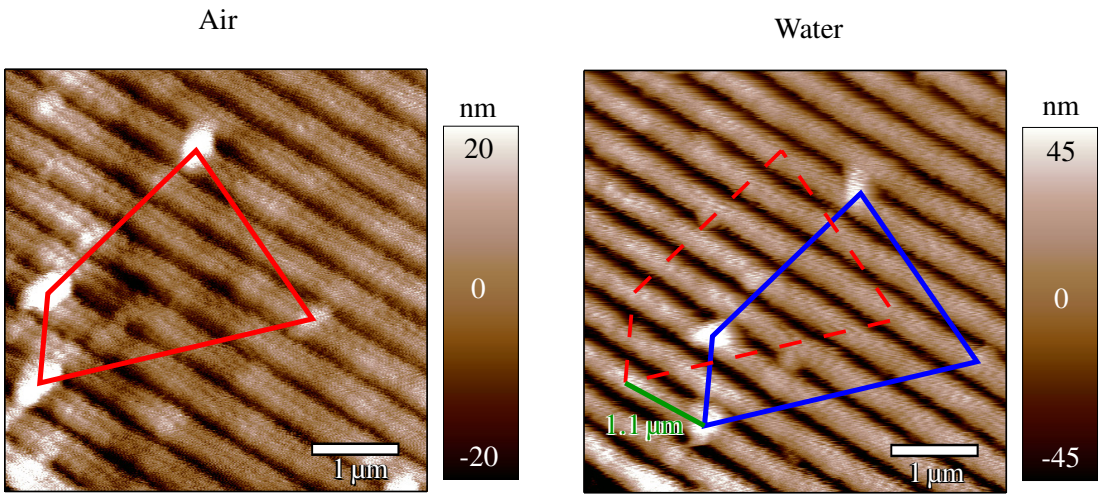

Figure 5.22: Two successive AFM measurements of a test grating in air and then in water. No realignment was necessary between the measurements. With usage of dirt particles, a small shift of only 1.1 µm is revealed.

in resonance frequency when changing the environment. Both resonances are depicted in figure 5.21.

The cantilever was brought into close vicinity of the grating. After tuning the resonance frequency, the cantilever was engaged onto the surface and a typical AFM measurement was performed. After the measurement the cantilever was withdrawn and distilled water was poured into the vessel until the grating and the cantilever were completely covered with water. Due to the increased damping of the water the resonance frequency was decreased. Thus a retune was performed and the wavelength of the readout laser was adjusted to return the highest amplitude. Then the cantilever was engaged again when the second measurement was performed. Both measurements are depicted in figure 5.22.

When comparing the measurements, four dirt particles can be spotted on both images with the same distance to each other. The only difference is that the measurements are shifted by 1.1 µm to each other. With this small shift it is an easy task to measure the same spot in different environments without the need of special equipment.

5.8 Summary and Outlook

In this chapter, the concept of 3D printed polymer cantilevers on fiber arrays was introduced. The actuation and readout principles were optimized based on theory, simulations and experiments.

Different measurements demonstrate the possibilities of the system as well as the high sensitivity which makes it even possible to reveal atomic steps on HOPG. All this studies were partly based on classical AFM cantilever geometries already known from silicon cantilevers to reduce the high degrees of freedom. Further studies could use those results and explore new territories in terms of form and function. Figure 5.23 shows an example of a cantilever already optimized for high resonance frequency due to less mass and with less dynamic friction to increase amplitude due to an aerodynamically optimized shape. The introduced system was only used for AFM measurements. Further application areas might include sensing applications with chemically active coated cantilevers to determine the concentration in liquids by the change of the resonance frequency or viscosity measurements.

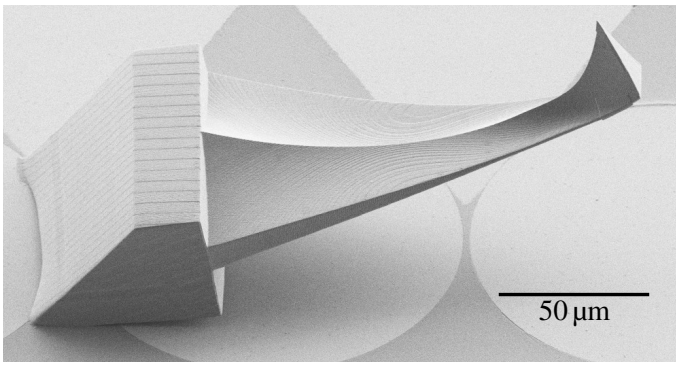

Figure 5.23: First design of an hydrodynamically optimized cantilever to improve amplitude and resonance frequency in liquid environment.

A manuscript of a shorter version of this chapter was prepared as 'Nanoprinted Scanning-Probe Microscope Engines utilizing Optical Actuation and Read-Out', Philipp-Immanuel Dietrich[1], Gerald Göring[1], Mareike Trappen, Matthias Blaicher, Thomas Schimmel, Hendrik Hölscher, Christian Koos

[1] contributed equally to this work

6 Freeform SNOM Cantilevers

Despite the use of 3D printed cantilevers for AFM, additional optical channels of the fiber array can be utilized to gather even more information from the sample. Whereas optical far field measurements are limited due to the Rayleigh diffraction limit at $d = 0.61\lambda_0/\mathrm{NA}$ with the minimum resolution d, the wavelength λ and the numerical aperture NA, the near-field does not suffer from this limitation. This fact is used by classical scanning near-field optical microscopy (SNOM) [186, 187]. The optical information is extracted out of the near-field by a small aperture with a subwavelength diameter or a small metallic tip which interacts with the local field. Even though in a classical setup SNOM is complicated and hard to interpret, SNOM is often required for life science [188, 189] or material science [190–193] and the characterization of integrated optical devices to select 'known-good' dies [194]. To obtain a small fiber with an aperture, a coated fiber is heated and thinned by a manual pulling process [92] or etching. Typically, either the illumination or the collection of the light is done with bulk optics.
As explained in chapter 2.2, a SNOM setup resembles an AFM setup. The specimen can be scanned in xy-direction and a feedback is responsible for the z-direction. In contrast to an AFM setup, the SNOM probe usually oscillates laterally above the surface and for the feedback a phase-locked loop is used. To actuate the fiber, it is tightly connected to a tuning fork. When the fiber oscillates in close vicinity to the surface, the resonance frequency changes, which can be used as feedback signal. The resolution increases the closer the fiber is to the specimen. Distances of smaller than 20 nm are preferable [195].

6.1 Design Considerations

To utilize fiber arrays as the base for a SNOM, the design of the previously developed standard AFM cantilever, which uses two fibers, one for the deflection readout and one for actuation, has to be expanded to include the necessary four optical channels. Due to the pitch of 127 µm, the cantilever would span over half a millimeter which would lead to low resonance frequency and low fabrication resolution since the cantilever would have to be written with a less magnifying objective due to the lens coverage and the size of the cantilever. During this work, two working approaches were tested, one will be referred to as 'wire bond SNOM' and one as 'standard SNOM', which was further investigated.

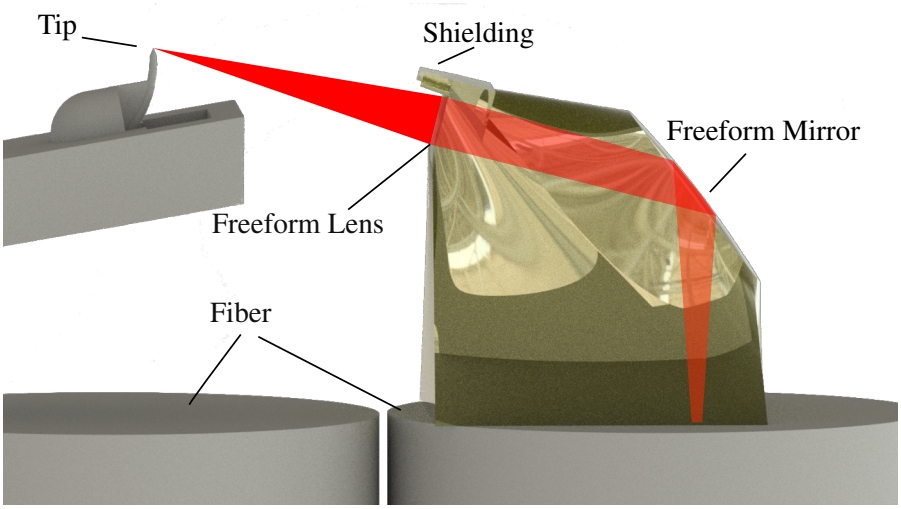

Figure 6.1: Rendering of the designed mirror which reflects the light from the fiber on the gold coating to the tip. The output is a freeform lens which focuses the light on the tip and is protected from evaporated gold by a shielding.

6.2 Working Principle

Both cantilevers share some basic principles: one is the illumination and the other one is the actuation. For the illumination a new approach had to be designed. The actuation itself had to be shifted to reduce the size of the cantilever.

6.2.1 Illumination

To have proper illumination of the tip, one fiber was utilized and will be referred to as illumination fiber. On the fiber a mirror was designed, which reflects the light from the fiber to the tip of the cantilever. To increase the reflectivity of the mirror, the gold coating usually applied to the cantilever was beneficial. The freeform mirror was designed to focus the light on the tip of the cantilever through a freeform lens as depicted in figure 6.1. To avoid back reflections of the light on the output of the mirror, a shielding was written above. As explained in chapter 2.2, SNOM typically relies on macroscopic optics, either for illumination or collection of the light. The presented approach easily substitutes the whole microscope.

6.2.2 Actuation

There are different approaches to account for the topography of a sample in SNOM measurements. It is possible to scan the topography and then rescan the sample with a certain distance for the SNOM signal or use dynamic modes and utilize the long-range forces for the feedback. When operating a SNOM in contact mode, the small aperture starts to wear off and increases in size pretty fast, which directly reduces the resolution of the optical signal. Thus an actuation has

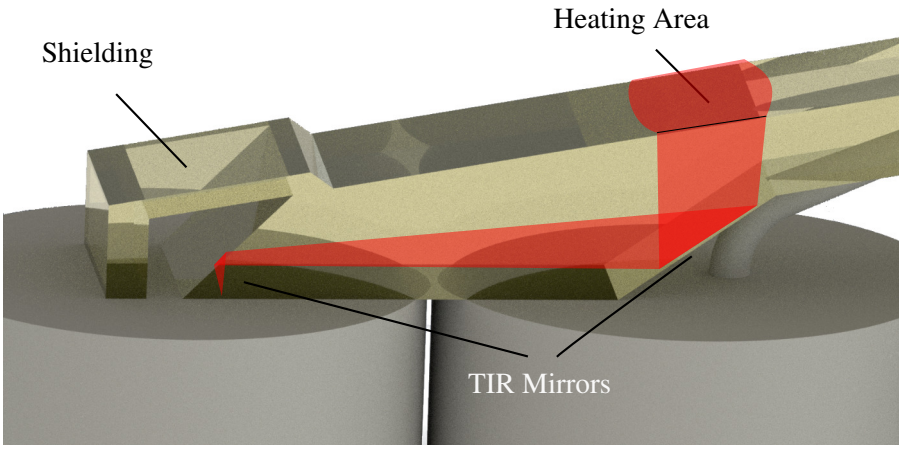

Figure 6.2: To have a short cantilever but still actuate at the base of the cantilever, two total internal reflections (TIR) were used to bring the actuation light to the base. Total internal reflections do not suffer from the absorption on the interface and thus improve the intensity.

to be implemented into the SNOM to operate in tapping mode. Since the distance readout and the light collector from the tip have to be on the moving cantilever, a solution with the actuation fiber not directly under the cantilever is preferred. One solution could be to use a second mirror as presented in the previous section and focus the light on the base of the cantilever, but there is a more elegant one. Due to the absorption on the interface between the polymer and gold, the intensity of light is reduced. On the other hand, total internal reflection does not suffer from this. Thus the solution is to use two total internal reflections to bring the light from the outer fiber to the base of the cantilever as depicted in figure 6.2. To obtain high reflectance using total internal reflection, the resist at the first reflection, which occurs at the top of the cantilever, is protected from the evaporated gold with a shielding. The second reflection is already protected by the cantilever itself.

Actuation Simulation

To be able to simulate the thermal response of the cantilever, the absorbed energy has to be known. As for the standard AFM cantilever in chapter 5.2.4, simulations were performed to acquire the absorbed energy. For the simulation a cube of the used IP-Dip resist, with an edge length of 500 nm, was used to simulate the way of the light through the cantilever. Since total internal reflection is used, no loss is expected and thus the reflections were not taken into account. The last two layers, the chrome adhesion layer and the 100 nm gold layer, are responsible for the absorption. Thus the simulated model consists of the cube IP-Dip resin and two subsequent layers of chrome and gold. For simulation, the propagation was simulated for a defined magnetic field as well as a defined electric field, each in y-direction, and started at the IP-Dip cube with zero incidence. To include thermal expansion in xy-direction, Floquet periodic conditions were applied. For this simulation, the same parameters as in table 5.1 were used. For the maximum of 10 mW from the actuation laser, an absorption of 22.7 % was simulated, which equals 2.27 mW.

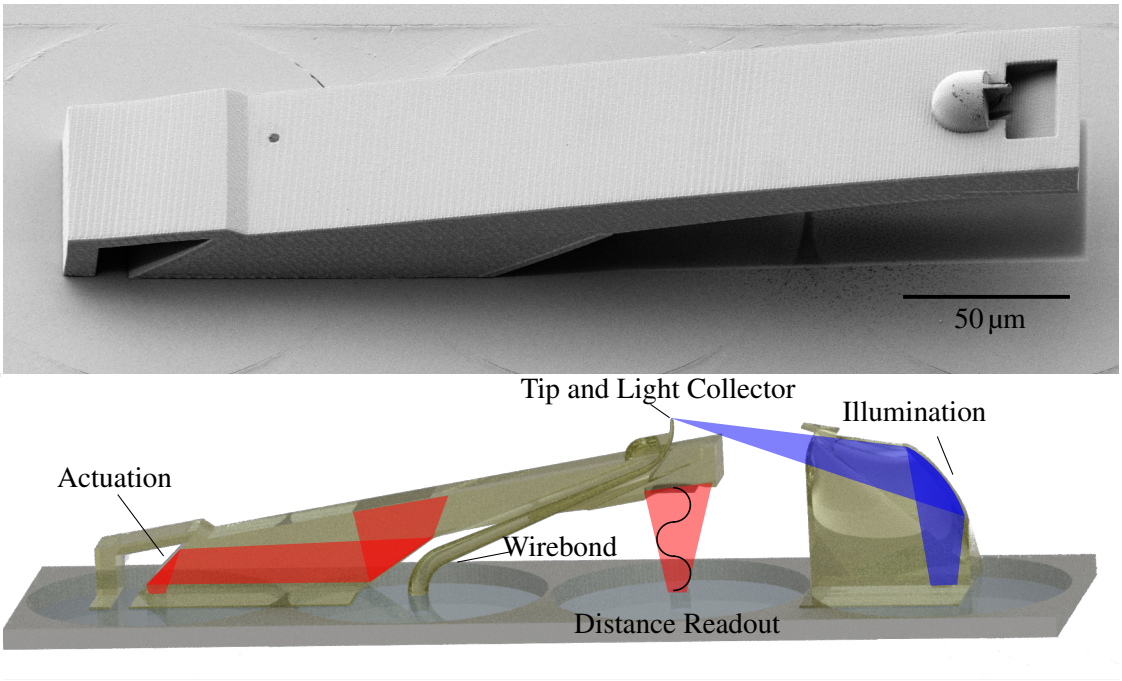

Figure 6.3: SEM image and half-section scheme of the wire bond AFM. The light of the illuminator is refracted from the specimen and then collected from the wire bond tip. The distance readout is located next to the tip.

In contrast to the AFM cantilever (1.58 mW), there is an increase in absorbed power. Since the only difference between those two simulations is that in the SNOM simulation the wave directly starts at the IP-Dip resin, whereas the AFM wave starts at a cube of air, the increase results from the missing transition from air to the resist.

6.2.3 Writing Parameters

Writing parameters of the illumination process are important since they influence adhesion, Young's modulus, the thermal expansion coefficient and more. To be able to compare the results obtained in this chapter, writing parameters were kept constant when not noted otherwise. The slicing distance of the model was set to 100 nm for the bulky part of the cantilever, whereas optical active areas like mirrors and lenses as well as the cantilever tip were sliced into 50 nm layers. The laser intensity was chosen to be near the destruction limit. This increases the Young's modulus due to an increased cross linking, which results in a high resonance frequency and improves the adhesion of the cantilever on the fiber array. The scanning speed was set to 10 mm/s for the parts sliced into 100 nm and to 1 mm/s for the finer parts.

6.2.4 The Wire Bond SNOM

The remaining two channels are the distance readout and the SNOM collector. Ideally both channels would be located at the tip, since the tip is used to also collect the light and the readout should have high sensitivity. One solution is to use a 3D printed wire bond [196] to guide the

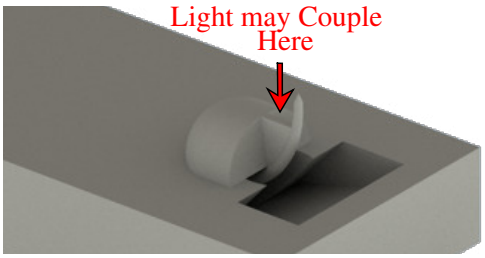

Figure 6.4: Calculations of the whispering gallery mode for the printed wiring board reveal that light may couple through the connection of the wire bond and cantilever into the bond.

light away from the tip into a fiber which is not directly located under the tip. The photonic wire bond is a concept introduced for chip scale interconnects. With these wire bonds light can be directed from the tip to a fiber with low losses. Thus for the readout, the fiber under the tip can be utilized. A schematic drawing as well as a SEM image is depicted in figure 6.3.

The left fiber is used as actuation fiber and the light is brought via two total internal reflections to the base of the cantilever as explained in section 6.2.2. The second fiber is connected via a photonic wire bond which is joined with the cantilever and simultaneously acts as tip. Due to the gold coating, the tip does not have an aperture and the cantilever has to be scanned above the surface until the tip opens. On the third fiber, the distance readout is implemented next to the tip. To protect the readout from stray light, the mirror for the cavity is printed on the bottom side of the cantilever and the top side consists of an angled surface which acts as light exhaust. On the fourth fiber the illumination mirror is printed. The mirror consists of a freeform mirror which is coated with gold and a freeform lens which focuses the light on the tip.
Figure 6.5 shows a measurement of an illuminated fiber array. To test the SNOM measurement, one fiber of a fiber array which was used as sample was illuminated. The fiber is a single mode type which has a well-defined Gaussian beam profile for wavelengths above 1260 nm. The measurements reveal some interesting effects. For the illumination of the sample fiber a laser with a wavelength of 1550 nm and a power of about 3 mW was used. The fiber itself should be flat, but it seems to have a curvature in the middle. This effect vanishes when the illumination of the sample fiber is switched off. Thus this effect is a thermal effect of the wire bond cantilever, which seems to deflect when being heated from the illumination, which results in a measured deflection of the topography. Further the measured SNOM signal is shifted by 1.5 µm to the topography. This is visible when comparing the green circle, which was drawn around the spot with the highest SNOM signal. But the most noticeable effect is visible in the blue cross section which is not only a Gaussian beam but also a second peak. To explain where this peak derives from, a whispering gallery mode calculation was performed for the wire bond. The mount of the wire bond on the cantilever allows not only the light from the tip but also the light from the mount to couple into the SNOM collection fiber. This also agrees with the position of the cantilever while scanning. The fast scan direction was perpendicular to the long axis of the cantilever. Due to the scaling of the SNOM image this effect is a little bit accentuated since it is only in the range of 8 %. But this measurement has led to the design of a second cantilever, which does not suffer from this problem.

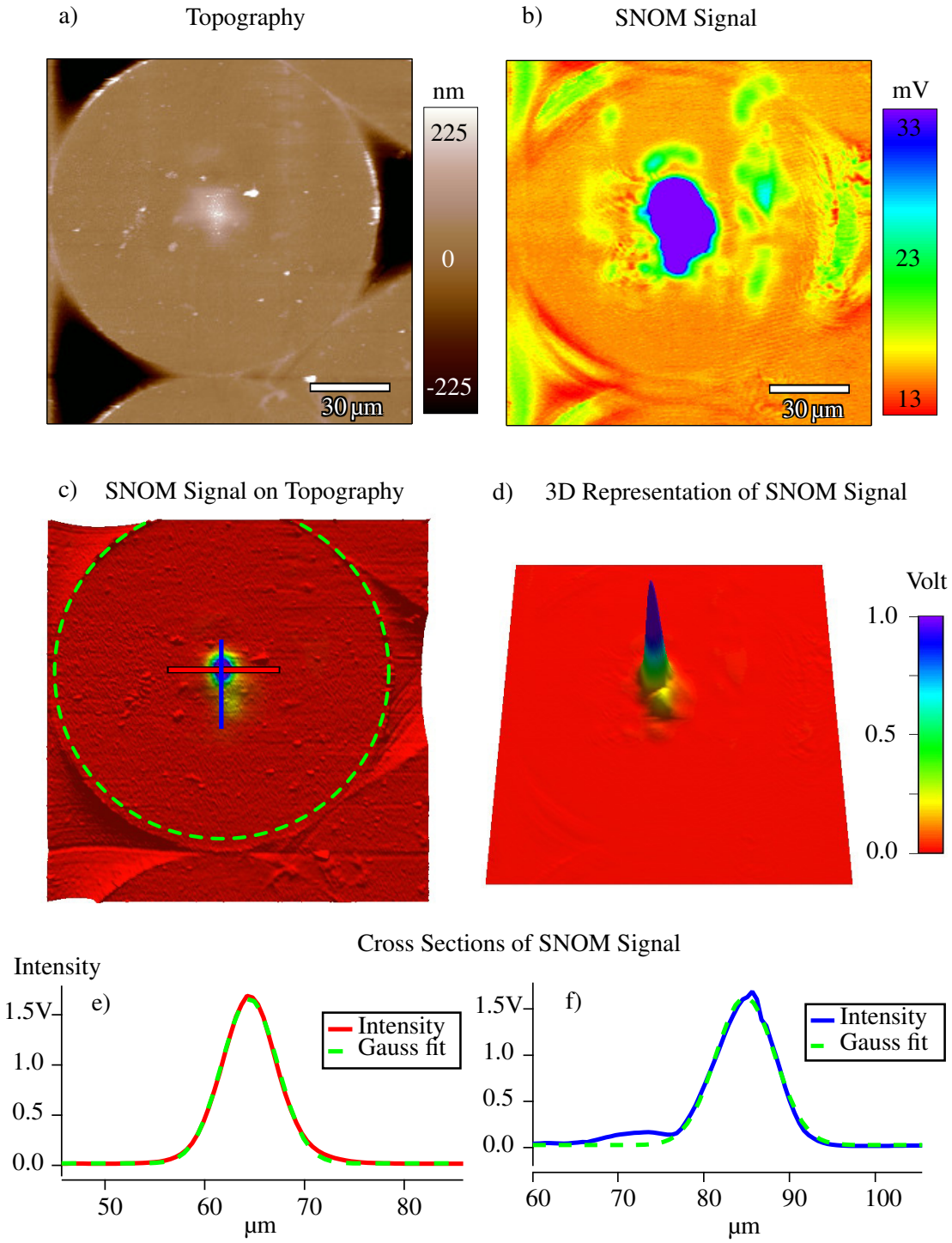

Figure 6.5: **a)** Topography and **b)+d)** SNOM signal of an AFM measurement of an illuminated fiber with the wire bond AFM. **c)** The SNOM signal is used as color code on top of the topography to measure the shift between topography and SNOM signal as indicated by the green circle in **c)**. The measured beam has a good Gaussian shape **e)** in x-direction but has some deformations **f)** in y-direction.

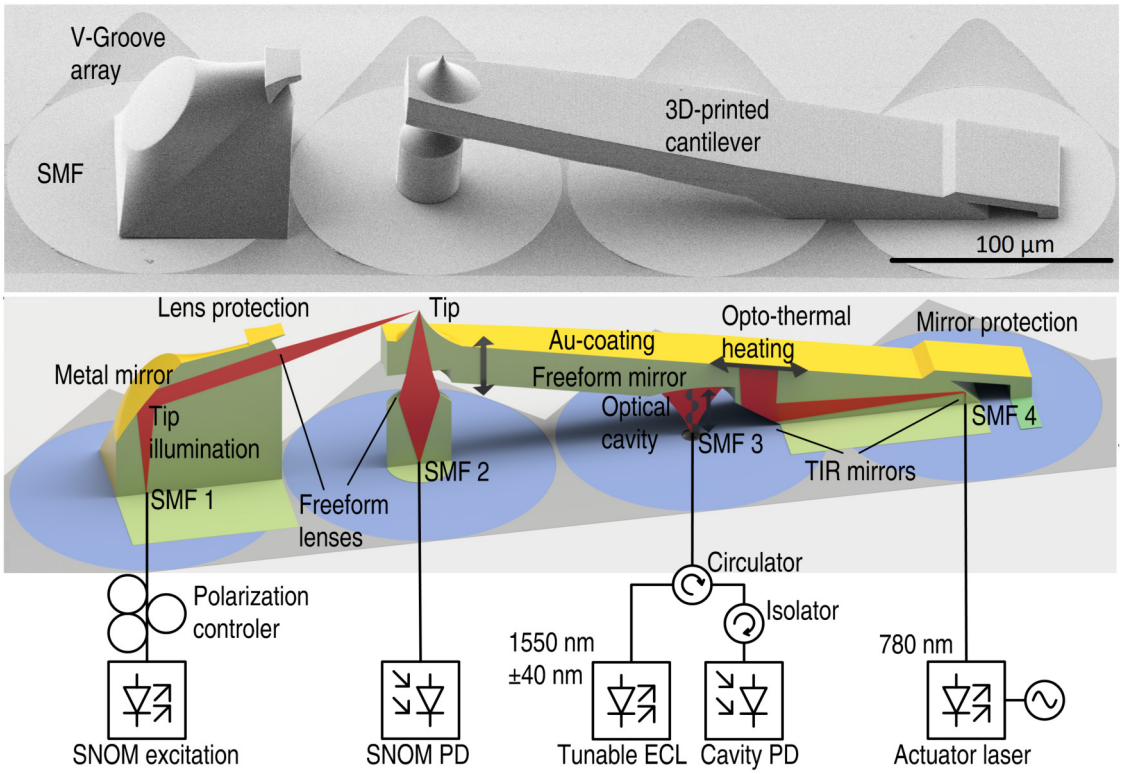

Figure 6.6: SEM image and scheme of the standard SNOM cantilever. The mirror consists of a freeform mirror coated with gold and a freeform lens which focuses the light on the tip. The SNOM collector is underneath the tip, where a lens couples the light into the single mode fiber (SMF). The distance readout is near the base and to get the actuation energy to the base of the cantilever two total internal reflections (TIR) are used. Adopted from [197].

6.2.5 The Standard SNOM Cantilever

On the wire bond SNOM the fiber underneath the tip was used for the distance readout and the light collected from the tip was directed with a photonic wire bond to the fiber which is situated more at the base of the cantilever. This was the first choice to have a high sensitivity. Since throughout all measurements the sensitivity was never a problem, the position readout and the SNOM collection fiber were interchanged. Thus the SNOM collection can be situated directly under the tip without the need of a wire bond and the readout is shifted more to the base of the cantilever. Figure 6.6 depicts a SEM image as well as a scheme of the setup.

For the illumination of the tip the freeform mirror explained in section 6.2.1 was used. To rotate the polarization of the light, a polarization controller was interconnected between the excitation laser and the fiber. The actuation scheme from section 6.2.2 with two total internal reflections was adapted. For the distance readout, a freeform mirror was designed to match the intensity of light coupled into the single mode fiber from the mirror to the reflectivity of the fiber facet. This forms a critically coupled cavity.

For the design the physical optics module of ZEMAX was used. There is no need for a light exhaust since the cantilever has a slope to make sure that only the tip is in contact with the

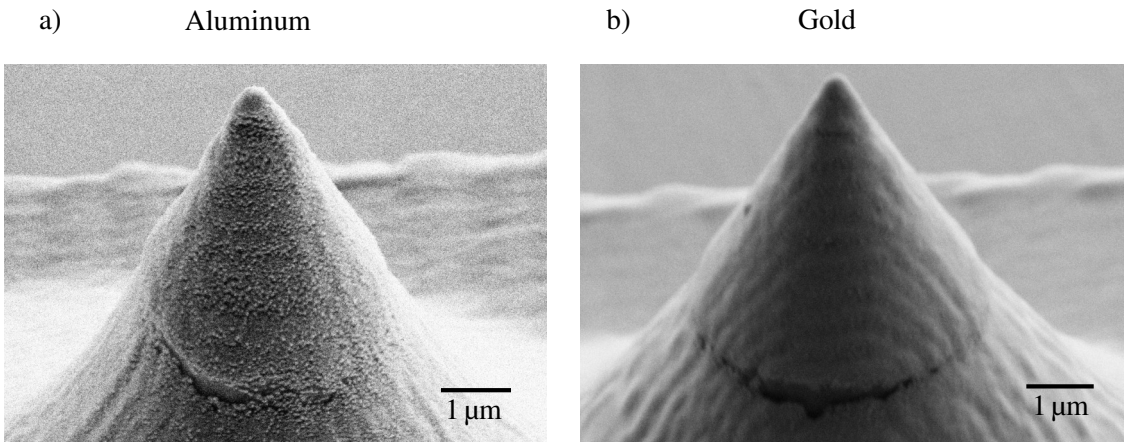

Figure 6.7: Two SEM images of cantilever tips. **a)** A tip evaporated with 100 nm aluminum and **b)** with 100 nm gold. Both on top of a 5 nm chrome adhesion layer. The aluminum tip is significantly rougher and more porous.

specimen, which keeps the readout far away from a reflective surface. The metal coating also attenuates enough to prevent stray light. To measure the deflection of the cantilever, a tunable laser with external cavity was used and connected with a circulator. The circulator is an optical device with three fiber connections. The circulator directs light from input A to input B, light from input B to input C and light from input C to input A with high efficiency. With this, the laser light coupled in from the laser exits at the cavity, and the laser light which is coupled from the cavity into the fiber then exits at the fiber connected to a photodiode. To prevent reflections from the photodiode which would be guided to the laser, an isolator was inserted. For the SNOM light collection, the fiber under the tip is used. To improve the efficiency, a freeform lens was printed on top of the fiber. Due to the 100 nm gold coating on top of a 5 nm chrome adhesion layer, the cantilever has to be scanned over a surface for a while to open a small aperture at the tip, which enables SNOM measurements.

6.3 Coating

In literature, most SNOMs use an aluminum cladding to form an aperture probe [92]. In this case, the same coating is also needed to have absorption of the laser light from the actuator to obtain a thermal expansion of the cantilever. To achieve this, gold was used. When using a 10 mW actuation laser with a wavelength of 785 nm, simulations in section 6.2.2 result in an absorption of 2.27 mW for a gold layer. The same simulation was also performed for an aluminum coating. An absorption of 2.32 mW was simulated, which does not show a significant difference. When comparing both coatings in the SEM, the aluminum is significantly more porous and more uneven than the gold coating. Also the adhesion of the gold layer is better than the aluminum one. This led to the decision to keep gold as top coating. It is also noticeable that in the SEM images a clear edge is visible at the tip. This is a result from the change of the writing parameters to decrease the tip radius. This edge could be reduced when using a gradual change instead of an

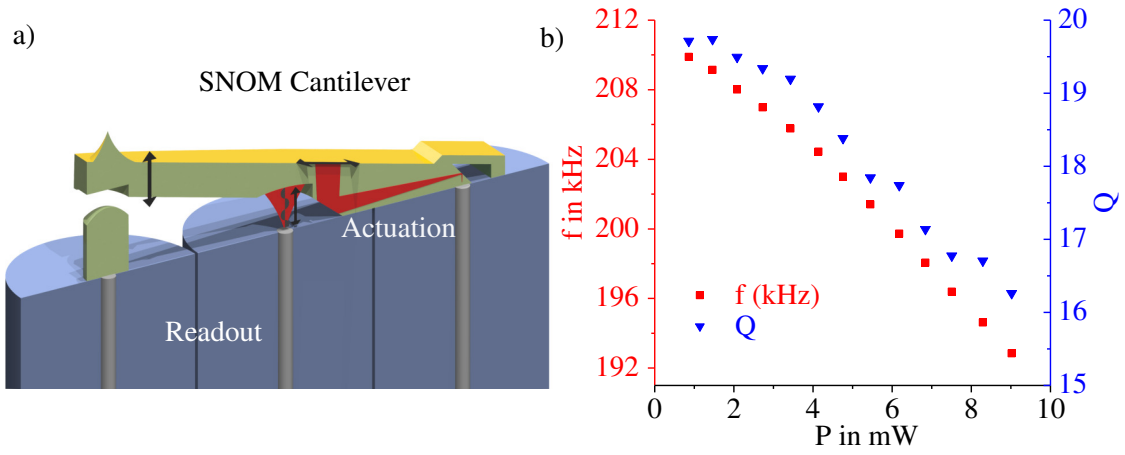

Figure 6.8: **a)** Schematic of the setup for thermal tuning. The cantilever is used as in a normal measurement but the offset of the actuation laser is stepwise increased for each resonance sweep. **b)** The increase of the structure temperature leads to a decrease of the resonance frequency as well as of the quality factor.

abrupt one.

6.4 Tuning of the Resonance Frequency

The resonance frequency of the standard AFM cantilever can be tuned by an offset from 1 mW to 9 mW in the actuation laser by 15.2 kHz. This helps to equalize fabrication deviations. For the standard SNOM cantilever this measurement was also performed. For this, the actuation laser was modulated with a voltage with a fixed amplitude and a variable offset. For every offset a sweep of the frequency was performed to acquire the resonance frequency. A Lorentz fit was automatically carried out for every spectrum and the resonance frequency was noted down as well as the quality factor. Due to the increase of the transferred heat to the cantilever, the cantilever temperature increases which leads to a softer material and thus to a decrease of the Young's modulus. This results in lower resonance frequency as well as quality factor. A scheme and the results of the measurements are depicted in figure 6.8.

Between 0 mW to 9 mW, the resonance frequency changed by 17 kHz, which equals a change of -2.13 kHz per 1 mW offset. This factor is a little bit higher than the one from the standard AFM cantilever but is still at the same range, as expected.

6.5 Reproducibility

When improving the properties of a cantilever, it is important to know how well a cantilever can be refabricated. For this, a measurement of reproducibility was performed. On a quartz substrate 69 standard SNOM type cantilevers were written as well as 71 standard AFM type cantilevers. The slicing was increased to 200 nm to improve production speed. Furthermore, tips were cut

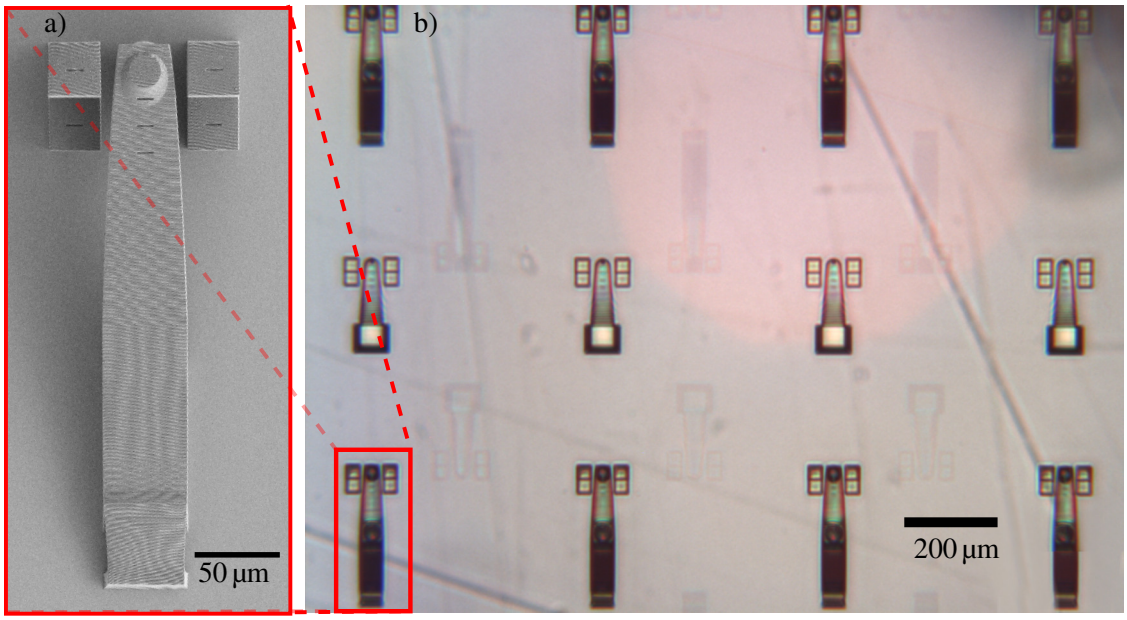

Figure 6.9: **a)** SEM image of one SNOM cantilever of the array depicted **b)** in the optical microscope image. The tip was cut of at 68.88 µm and reference blocks were written with the same height to be able to compare the bending of the cantilever.

off in a height of 68.88 µm above the substrate. To easily compare the height with the designed height, reference blocks were placed beside the cantilever. Slits were placed into the blocks as well as into the cantilever to evaluate shrinkage.

6.5.1 Resonance Frequency

The resonance frequency is an excellent indicator for reproducibility. It depends on the form of the cantilever as well as on the Young's modulus. Deviations in the production lead to a deviation in the resonance frequency. To measure the resonance frequency, the quartz substrate was mounted on a printed circuit board, which was originally used to electrically contact the TMR cantilevers. This board was mounted on a holder with an integrated piezo actuator. For the readout of the resonance frequency, a laser was focused on each cantilever and the reflected light was collected in a split photodiode as with conventional AFMs. To improve the reflectance of the cantilevers, they were coated with 100 nm gold on top of a 5 nm chrome adhesion layer. The highest peak in the frequency sweep was taken as resonance frequency since a Lorentz fit did not match good with the measured form of the resonance due to the noise produced by the other cantilevers, which led to an oscillation of the hole substrate.

The resonance frequency of all 69 cantilevers has a mean value of 188 kHz. Compared to the variances from commercial cantilevers, which are in the range of 30 % [5, 6], the 3D printed cantilevers have a low deviation of 3.9 kHz, which equals 2 %. By thermal heating, the resonance frequency of the SNOM cantilever could be varied by 17 kHz, which is larger than the 2σ

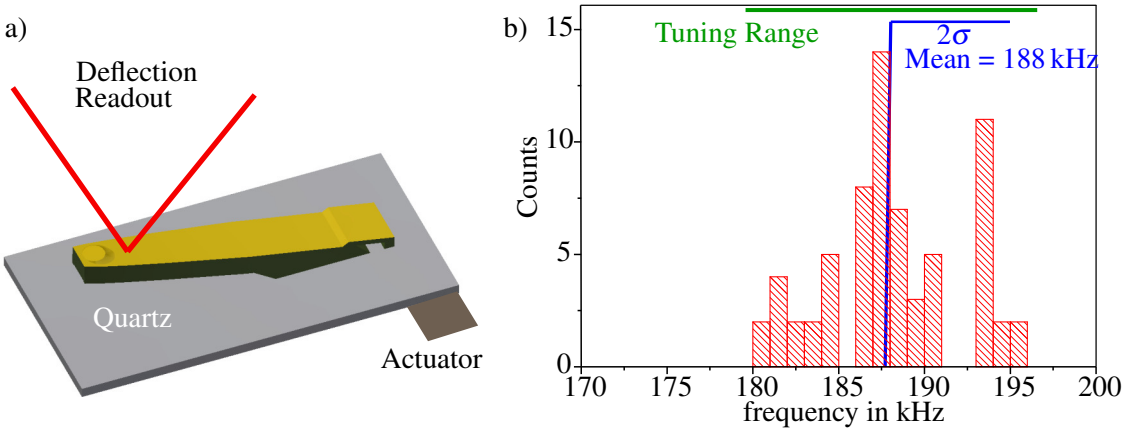

Figure 6.10: **a)** The readout of the cantilever on the quartz substrate is depicted. **b)** The histogram shows excellent reproducibility. The remaining deviation can be adjusted by thermal heating.

deviation of the cantilevers. This means that more than 95 % of all cantilevers can be brought to oscillate at the same resonance frequency.

6.5.2 Height Deviation

To have a high sensitivity at the deflection readout, a certain wavelength has to be chosen. This wavelength depends directly on the length of the cavity between the fiber and the cantilever. In these experiments, a tunable laser with an external cavity was used to always have the highest sensitivity. Besides the high price of such a laser, this comes for the cost of noise due to wavelength shifts and sensibility for external vibrations. When aiming for commercial usage of the system, a laser with a fixed wavelength is preferred. Therefore the deviation in the cavity is of great importance. To measure the height of the cantilever, a vertical scanning interferometer (VSI) (Bruker ContourGT-K with 50x magnification) was used. The height of the cantilever was defined as difference between the substrate and the cut off tip. A histogram of the acquired data and an example measurement of the VSI is depicted in figure 6.11.

As a result, an average height of 69.0 µm was measured. This matches well the designed height of 68.88 µm. A deviation of 689 nm was measured which is a good value compared to the 2.68 µm of the standard AFM cantilever presented in figure 5.16. This can be explained by the thicker cantilever of the standard SNOM. This prevents the upbending, which was the major reason for the height deviation of the standard AFM cantilever. This information has led to a design of a thicker AFM cantilever.

6.5.3 Predetermination of the Resonance Frequency

The resonance frequency of the produced cantilevers has a low deviation but when designing a cantilever, the design of the resonance frequency is also of interest. The best method to determine the resonance frequency of the cantilever is to simulate the resonance with Comsol or Autodesk

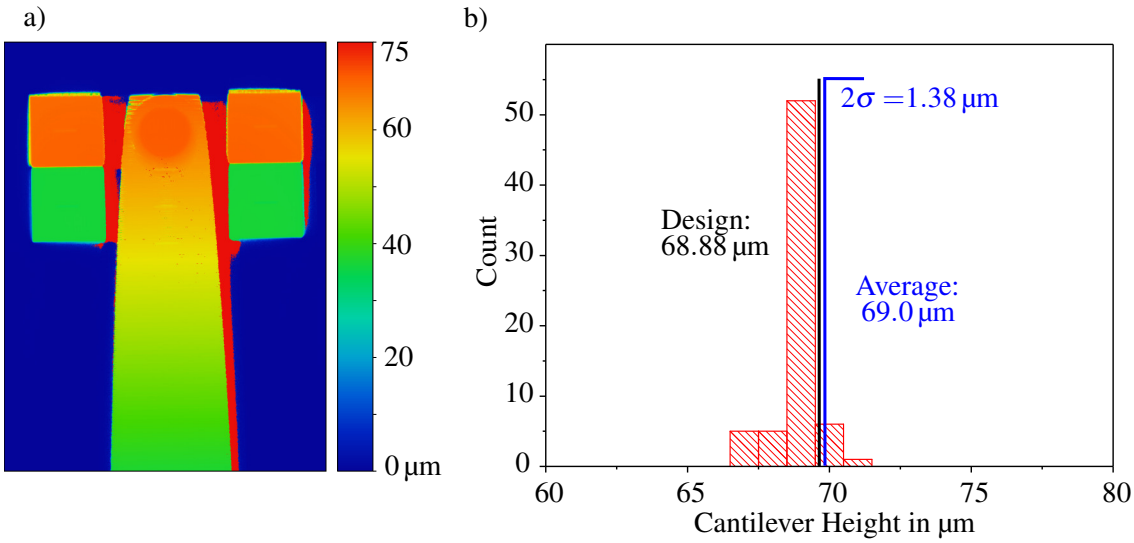

Figure 6.11: **a)** An example VSI measurement to determine the height of a SNOM cantilever. **b)** A histogram of the height deviation of 69 standard SNOM cantilevers. Designed and measured height deviate only 120 nm.

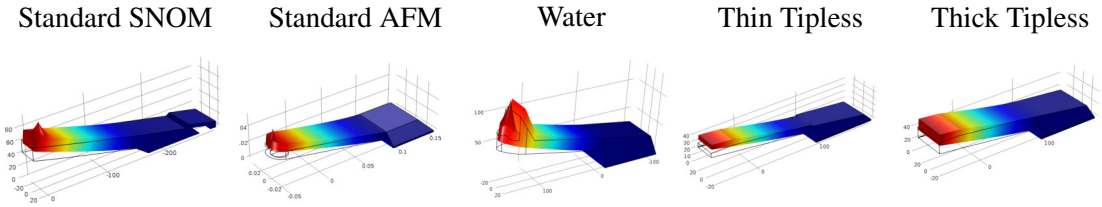

Figure 6.12: Comsol simulations of the bending behavior and resonance frequencies of different kind of cantilevers. Adopted from [22].

Inventor and change the mass or geometry of the cantilever according to the desired result. To do this, the density ρ and the Young's modulus have to be known. The density itself does only marginally depend on the writing parameters whereas the Young's modulus is highly dependent on the writing parameters as explained in section 5.5.3. Figure 6.12 shows a collection of the simulated deflection of different cantilevers. In table 6.1 the measured and simulated resonance frequencies are listed. For the simulation, a Young's modulus of 3.5 GPa was used as mentioned in literature [172]. The cantilevers were written with a laser power near the destruction limit. The calculated error of all resonances is only 1.8 % but with a deviation of 11 %. When comparing the design with the results, a relation between the thickness of a cantilever and the deviation becomes

Table 6.1: Overview of the measured resonance frequency, the fitted Young's modulus to obtain the resonance frequency and the resonance frequency obtained by Comsol when using the literature value of 3.5 GPa for the Young's modulus [172].

Cantilever type	SNOM	AFM	Water	Thin Tipless	Thick Tipless
Resonance Frequency f_0 in kHz	189	179	173	125	181
Fitted Youngs modulus E in GPa	3.36	4.16	3.60	3.70	2.40
f_0 calculated (E =3.5 GPa) in kHz	191	164	171	121	218

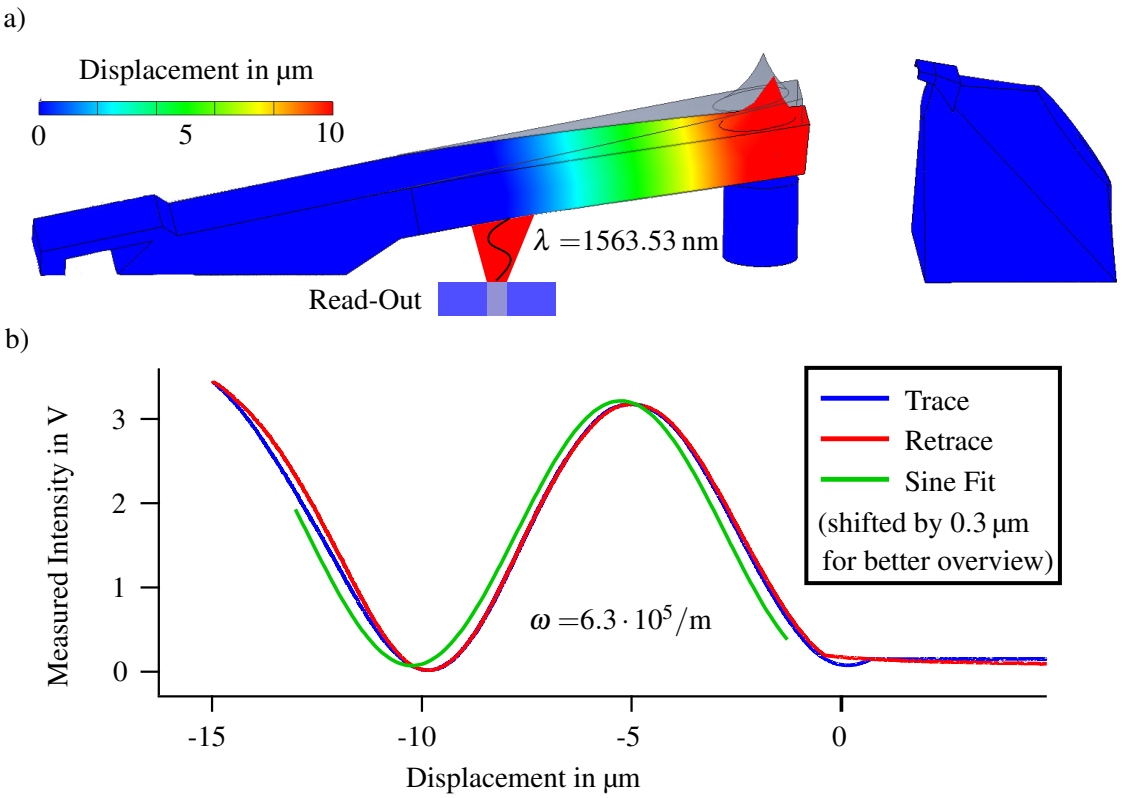

Figure 6.13: **a)** Static deformation simulation of the standard SNOM cantilever. **b)** A large force curve to calibrate the mechanical reduction factor δ_{static}. The green sine fit was shifted to the left by 300 nm to simplify interpretation.

apparent. Whereas the SNOM and the thick tipless cantilever have a resonance frequency below the simulated one, the others which were thinner have a resonance above the simulated one. As first this seems counterintuitive, but including the writing process, which happens layer by layer in z-direction parallel to the substrate, the layer area increases with the thickness of the cantilever due to the slope of the cantilever. This leads to a lower time per layer for thin cantilevers, which means that the same xy-position is illuminated faster again due to the focus size of the writing laser, which is taller than the layer size. This increases the cross linking and leads to a higher Young's modulus for thin cantilevers, which results in a higher resonance frequency than expected.

6.6 Calibration

Since the readout of the standard SNOM cantilever is located far away from the tip, the cantilever has to be investigated further. As already mentioned in section 5.6, the cantilever deflects differently, depending on the acting forces. This leads to another form when dynamical shaking than when forces act only at the tip like on a force distance curve or in contact mode. At typical force distance curves, it is possible to calibrate the dependency between the deflection readout, which is typically measured in volt, and the covered distance of the tip. In a normal AFM setup this has to be performed for every new cantilever that is mounted since the laser is focused on

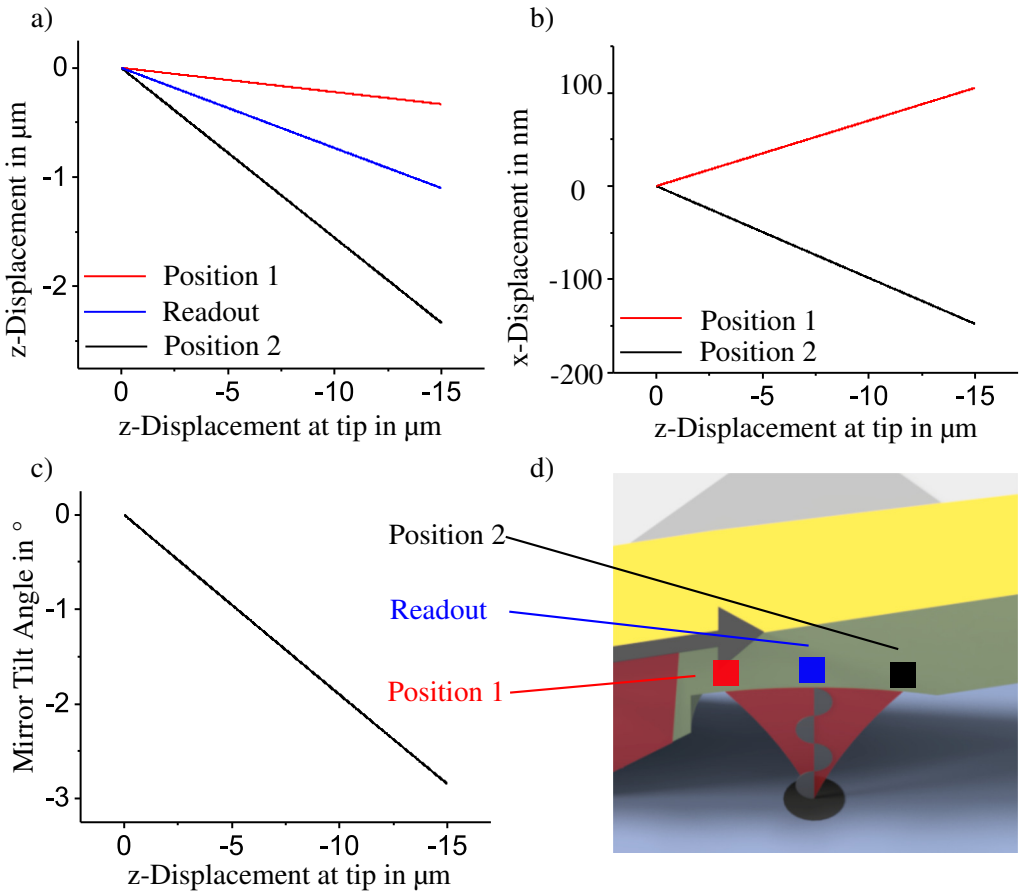

Figure 6.14: **a)** Simulation of the behavior of the cavity for a deformation caused by an acting force on the tip. **d)** Different points of the cavity are simulated. The movement of those points **a)** in x-direction **b)** in z-direction and **c)** the angle between those is plotted in dependency of the traveled distance of the tip.

a different place, which leads to a different reflection onto the photodiode. For the 3D printed cantilever, there is an easier way to calibrate the cantilever without the necessity of pressing the cantilever tip on a surface. The cavity length can be easily calculated by measuring the distance between two maxima when sweeping the wavelengths of the readout laser. Since the cavity is not directly under the tip, a mechanical reduction factor δ_{static} has to be incorporated. This can be simulated or measured with a force distance curve. Due to the high reproducibility, this has to be done for each cantilever type only one time. To be able to compare the simulation result with the experiment, a force distance curve was performed with the SNOM cantilever. The result is depicted in figure 6.13. The measured intensity has a sine wave form as expected. To calculate the mechanical reduction factor δ_{static} formula 2.3 from 2.1.1 can be used

$$\delta_{static} = \frac{2 \cdot \Delta z}{\lambda} = \frac{4 \cdot \pi}{\omega \cdot \lambda} = 12.76,$$

for the used wavelength λ =1563.53 nm. The frequency ω was derived from the plotted sine fit in green, which was shifted by 300 nm to the left to simplify the reading. To investigate the change of the cavity on the SNOM cantilever, different simulations of the behavior of the cavity were performed and depicted in figure 6.14. To evaluate the cavity when the cantilever

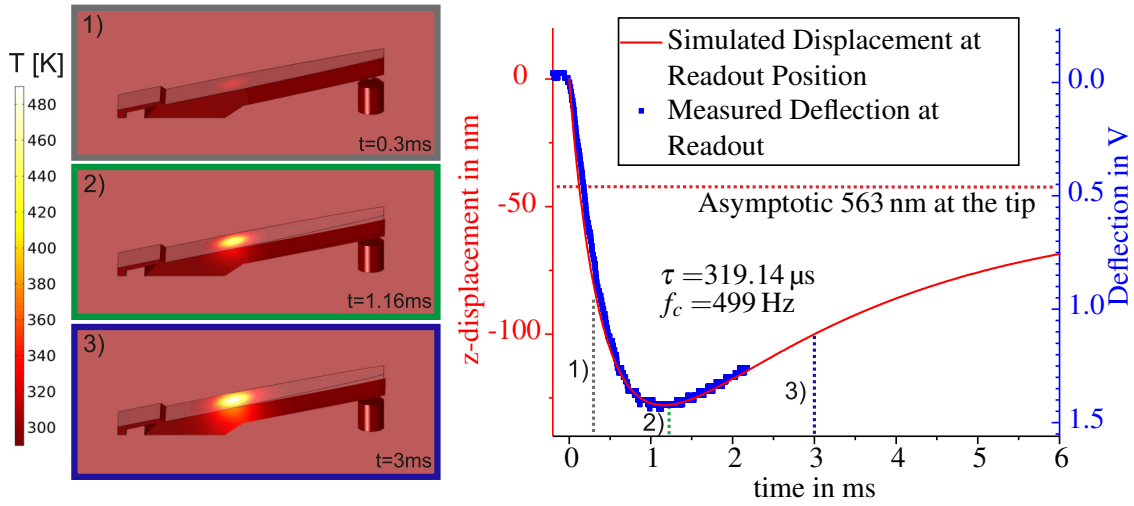

Figure 6.15: Measured and simulated thermal response of the cantilever when applying a laser pulse on the actuator. Temperature distribution in the cantilever for three different times are depicted.

deforms due to a force at the tip, three points are of importance: The beginning of the cavity, in the figures marked as 'Position 1', the middle of the cavity which is designed to be centered above the readout fiber and the end of the cavity, marked as 'Position 2'. Ideally, those positions move only equally in z-direction to just change the lengths of the cavity. But the simulations reveal that the z-positions of each point behave differently, which leads to a tilt angle of the cavity, which changes the couple efficiency calculated with Zemax from 99.1 % to an efficiency of 71.0 % for a covered distance of 15 µm. Due to the much smaller deflection of the cantilever when operating in tapping mode, a stable operation is expected. The reduction factors for static and dynamic actuation are simulated to be $\delta_{static} = 13.62$ and $\delta_{dynamic} = 11.76$, which excellently fits to the δ_{static} from the measurement. The ratio of dynamic and static factors is set to 1.09 for a conventional AFM. When measuring with the standard SNOM cantilever, it thus has to be set to $\delta_{cal} = 1.15$.

6.7 Thermal Response

The amplitude of the standard AFM cantilever was mainly limited due to the slow thermal response of the cantilever. The comparison between the measurement and simulation also suffered from the problem that the mirror of the cavity on the cantilever was not just shifted along the direction of the cavity, it was also tilted and shifted perpendicular to the cavity. Because of the large mechanical reduction factor δ_{static} this is not expected for the standard SNOM cantilever. The parameters for the simulations are listed in table 5.1 and as transferred energy, the simulated absorbed energy of 2.27 mW (section 6.2.2) was used. Heat is produced with a Gaussian distribution at the gold coating. Due to the high thermal gradient in the cantilever at the beginning, a strong downbending of the cantilever is visible. After a short time, the heat spreads in the cantilever which decreases the gradient and bends the cantilever back. The cantilever converges at a displacement of the mirror of 45.5 nm. To be able to compare the simulated thermal step

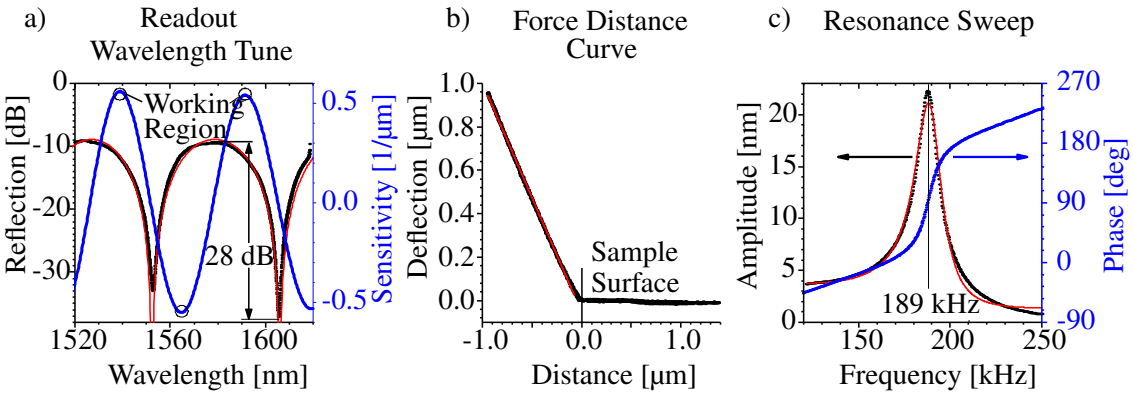

Figure 6.16: Overview of some typical properties of the SNOM cantilever. **a)** The measured intensity of the readout while tuning the wavelength. The sensitivity is plotted in blue and the targeted working points are marked. **b)** A force distance curve and **c)** a calibrated resonance sweep. Adopted from [197].

response with the experimental step response of the cantilever, the actuation laser was switched on from under the lasing threshold to full power. To measure the deflection, the optical cavity readout was utilized. Simulation and measurement depicted in figure 6.15 match perfectly. This is helpful to benchmark the behavior when designing a new cantilever and helps to optimize the thermal corner frequency. Due to the low corner frequency f_c =499 Hz, the thermal actuation suffers from large attenuation. This results in a low amplitude for thermal actuation.

6.8 Proof of Concept

Before performing the SNOM measurements, a characterization of the used cantilever was performed. In figure 6.16 an overview of the measurements is depicted. Before the wavelength for the readout was chosen, a sweep between 1520 nm to 1620 nm was executed. This was done to find the working points on which the highest sensitivity can be realized. With this tune, the cavity length can be determined and thus the calibration factor can be calculated to convert the measured voltage in a distance. Some instabilities in the tune can indicate some regions which should be avoided. After the wavelength, and with this the working point, was chosen a force distance curve was performed to check the calibration. This additional step has to be performed only once for every cantilever design. When operating in tapping mode, the resonance frequency can be determined by a sweep of the frequency of the actuation laser. A typical frequency spectrum is depicted on the right side. It is visible that the baseline of the tune is declining, which can be explained by the thermal corner frequency f_c, which is way below the resonance frequency and acts as a low pass filter.

To prove that the cantilever works as expected, a test structure was designed with different forms and shapes. A SEM image of the structure is depicted in figure 6.17. The structure consists of different forms in different sizes to measure the resolution of the cantilever. They are produced on a glass substrate via coating and etching. The structures consist of approximately 20 nm chrome. Figure 6.17 shows two example measurements of the topography as well as the SNOM signal.

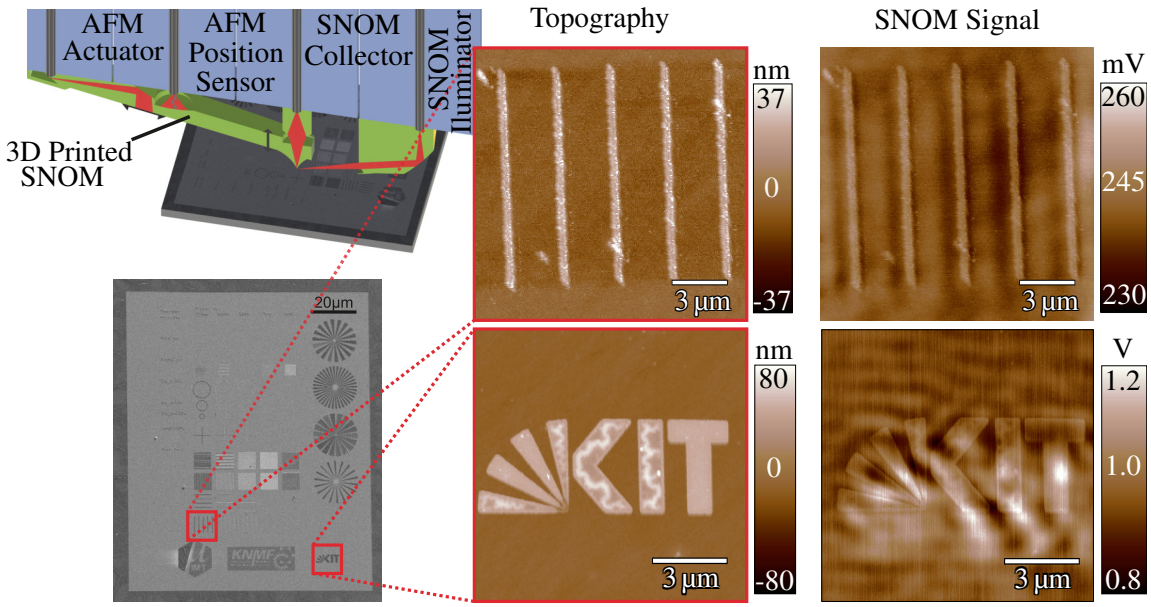

Figure 6.17: A schematic of the measurement of the test sample and a SEM image of it. Two measurements of different parts are presented on the right. The SNOM signal is higher on the chrome structures and shows shadowing in the line sample and interference effects on the KIT sample.

The measurement setup was the same as described in section 5.7 for the AFM measurements but extended with tip illumination and collection. For the SNOM signal, the sample was illuminated through the printed mirror with one out of eight available fiber coupled lasers of the two utilized MCLS1 (Thorlabs) quadruple Fabry-Pérot laser modules. The light refracted by the sample is then collected with an aperture in the tip and converted into a voltage by an Agilent 8163A Lightwave Multimeter. This voltage is then fed into the ARC2 controller and recorded as additional channel in the software.

The measurement of the line area from the test sample leads to the expected result. The SNOM signal is increased on the chrome lines. Additionally, some typical SNOM effects like shadowing are visible. The KIT logo also suffers from interference effects, which can be recognized by the periodic modulation of the SNOM signal. The topography measurements on both structures are clear and reveal on the KIT logo that the production process of the test sample has to be improved since it seems that the Polymethylmethacrylat (PMMA) used during the production is still partly on the chrome.

6.9 Mode Field of a Single Mode Fiber

To measure the precision of the SNOM readout, a sample with a well known optical near-field illumination can be measured. On the wire bond cantilever presented in section 6.2.4, the measurement of a single mode fiber with a well specified core revealed the existence of a whispering gallery mode. The single mode fiber is also suitable to test this SNOM cantilever. In figure 6.18 this measurement is depicted. The top left image shows the measurement setup. The measured

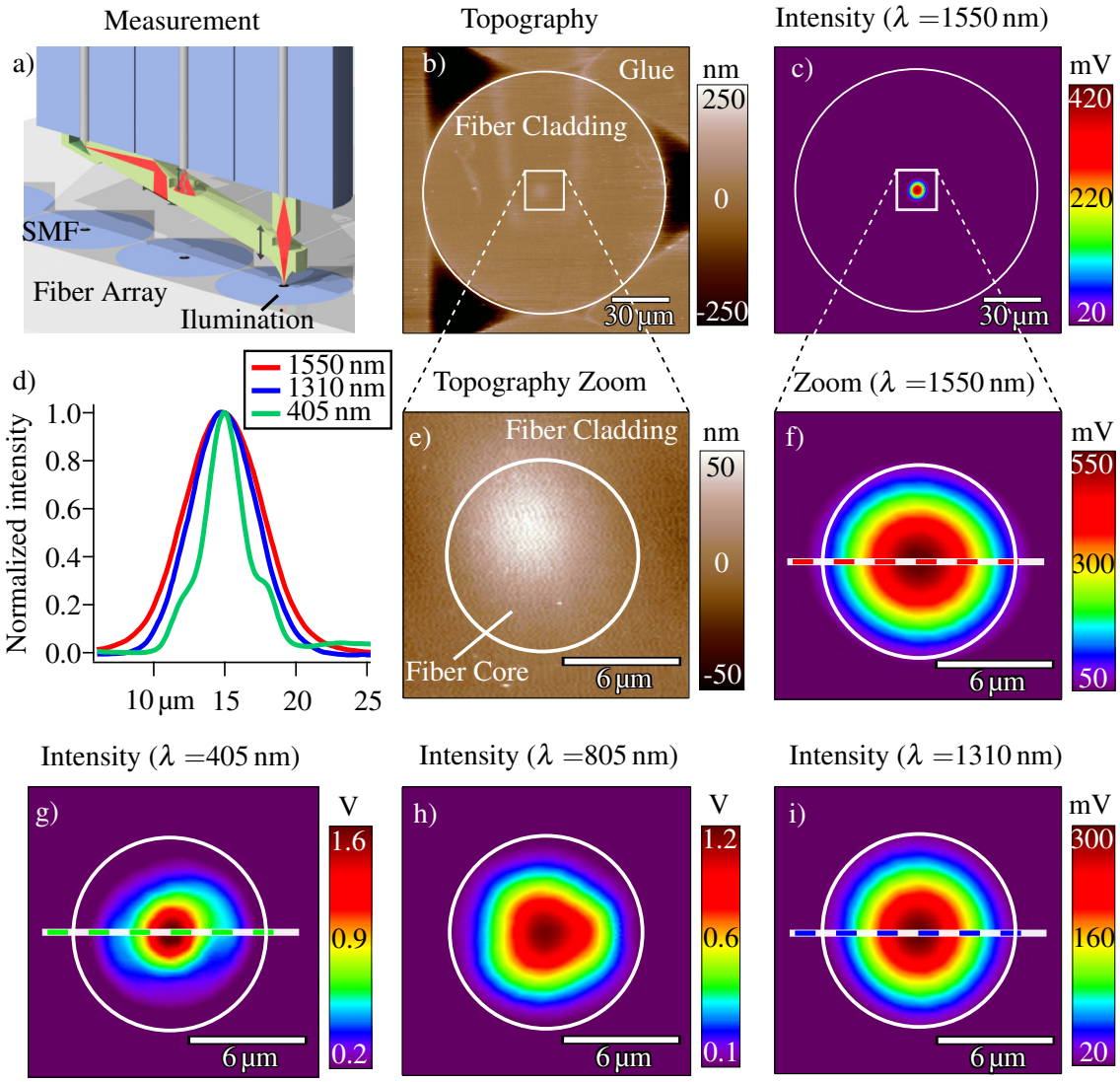

Figure 6.18: **a)** Setup of the measurement of the mode field of a single mode fiber (SMF) which is specified for single mode operation above 1260 nm. **b)+c)** A scan of 150 µm for the overview is shown as well as **e)+f)** a zoom image of the fiber core. **f)-i)** SNOM images reveal nice Gaussian shapes of the mode field for **f)** 1550 nm and **i)** 1310 nm whereas the profiles for **h)** 805 nm and **g)** 405 nm show multimodal behavior as expected. **d)** Cross sections of the mode field for different wavelengths.

single mode fiber is specified for single mode operation for wavelengths above 1260 nm. The topography is flat despite the v-grooves that were used to align the fibers in the fiber array. To find the core of the fiber, the fiber is illuminated with a 1550 nm laser with a power of approximately 3 mW. The SNOM channel leads to the core with 10 µm diameter. After zooming in, the SNOM image reveals a Gaussian shaped beam. The $1/e^2$ mode field diameter (MFD) lies in the specification of the fiber. The topography shows a little bump in the center. This bump disappears when the 1550 nm laser is switched off. This can be explained by an additional absorption of energy by the cantilever coating of the illumination laser, which leads to a bending of the cantilever and leads to this artifact of an elevated surface. This effect can be reduced when using lower energy for the illumination. As expected, the form of the mode field of the 1310 nm is similar to the form of the 1550 nm laser. When using a laser with a wavelength of 805 nm, which is below the

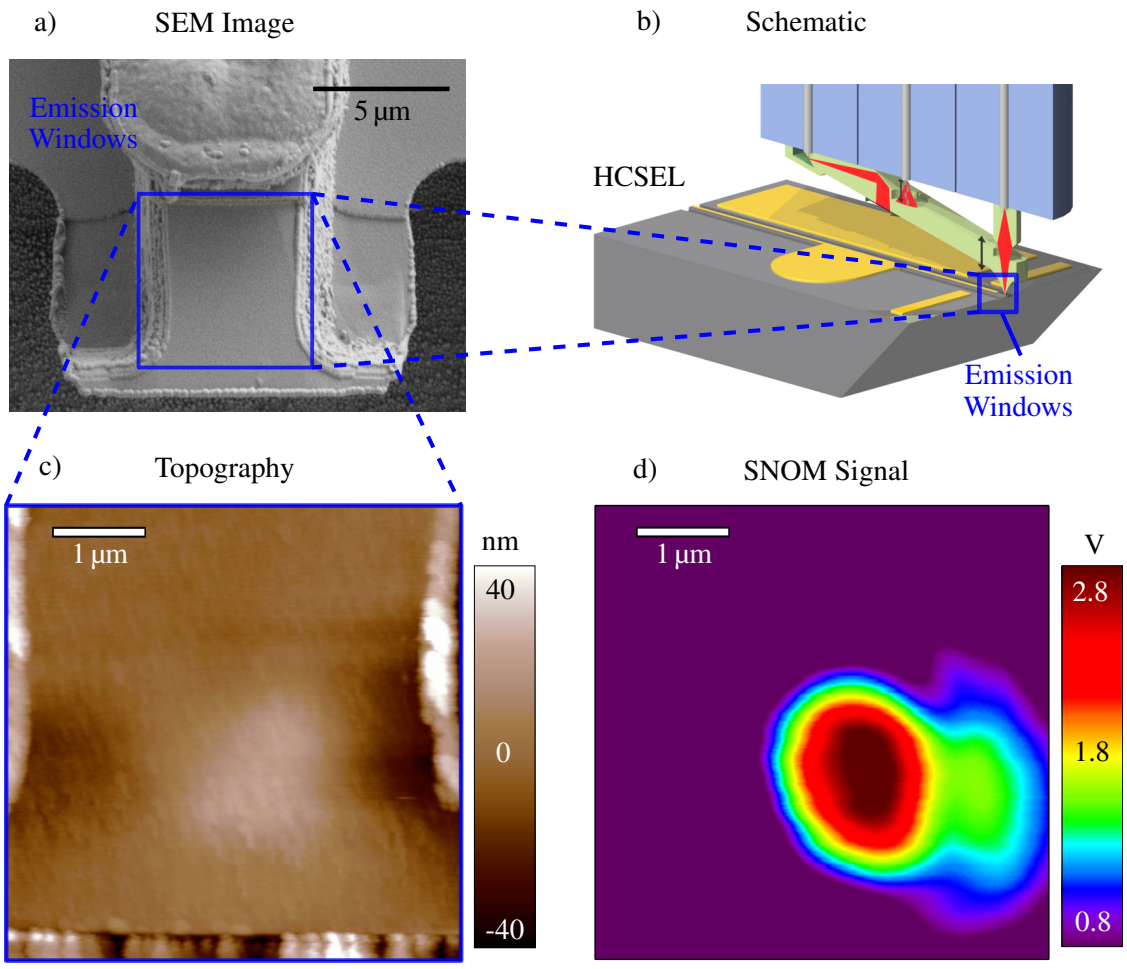

Figure 6.19: **a)** SEM image of a vertically emitting horizontal cavity laser (HCSEL). **b)** Setup of the SNOM measurement. **c)** With the help of the measured topography the **d)** mode field can be allocated and a diameter of 3.5 µm and 3.2 µm along the slow and fast scan axis respectively, is calculated by the second order-moment method. This excellently fits to the mode filed calculated from the far-field.

specification for single mode operation, the mode field starts to deform. When using a 405 nm laser, multiple deformations occur and the mode field is completely different from a Gaussian one. This measurement proves the SNOM cantilever to properly work and be able to measure a mode field without any artifact from whispering gallery modes. One has to be careful with the amount of energy which is absorbed by the cantilever because it can lead to a deformation of the measured topography.

6.10 Mode Field of a HCSEL

The measurement of the mode field is of great importance when designing lenses for coupling the light from the device or for all kind of freeform lenses. There are different approaches to calculate the near-field from a far-field measurement like an angular scan in one direction of the far-field radiation pattern [198] or the transverse offset technique, which uses the coupling efficiency to calculate a possible near-field [199]. A vertically emitting horizontal cavity laser

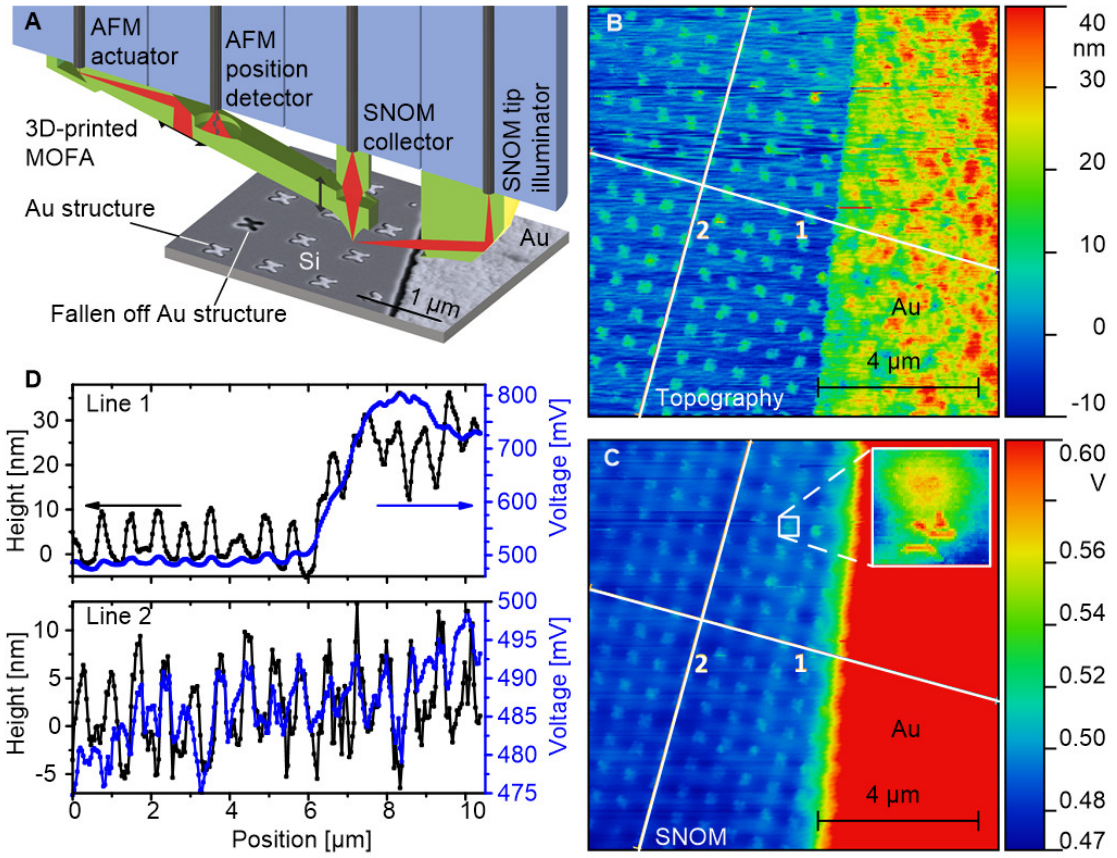

Figure 6.20: SNOM measurement of bow-tie antennas. The antennas are arranged in a regular pattern with a distance of 650 nm, which is resolved well. The antennas are illuminated with the IR part (λ >1180 nm) of a white light laser through the 3D printed freeform mirror. In the SNOM image the antennas are also well resolved, which demonstrates a resolution better than the Abbe limit. Adopted from [197]

(HCSEL) is a component that generates a non-trivial optical near-field. To calculate the form of a lens which efficiently couples the light into a single mode fiber, the near-field of this laser has to be known. The used HCSEL operates at a wavelength of 1490 nm and is set to emit a power of 1.5 mW.

The measurement of the topography in figure 6.19 matches the SEM image, despite the small bump directly at the center of the maximum emission, which is caused by a deformation of the cantilever due to the absorbed heat. The SNOM image reveals a non-uniform near-field, which can be calculated by the second order-momentum method, with a mode field diameter of 3.5 µm along the slow scan axis and 3.2 µm along the fast scan axis. Far field measurements of the HCSEL result in corresponding mode field diameters of 2.8 µm and 3.2 µm [200]. This demonstrates the simplicity of the presented method to obtain quantitative data to characterize light emitting components.

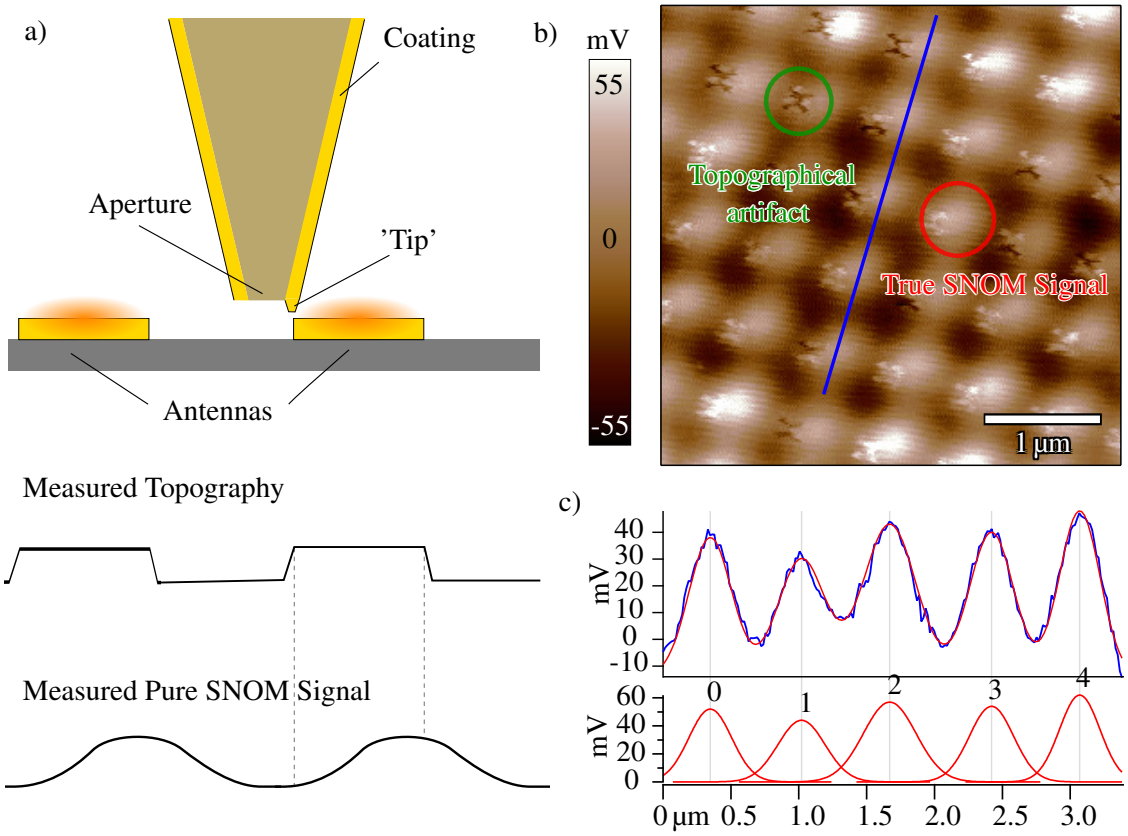

Figure 6.21: **a)** Schematic explanation for the shift between the topography and SNOM signal. **b)** Zoom-in on a detail of the SNOM image of the bow-tie antennas in figure 6.20. Topographical artifacts are visible and a little bit shifted to the pure optical signal. **c)** To estimate the resolution of the SNOM signal, a cross section was taken and fitted with multiple overlapping Gauss curves, which can be used for the calculation of the resolution.

6.11 SNOM Image of Nano Antennas

Not only the mode field of emitting components is of interest. Plasmonic structures have a different scattering cross section for different wavelengths. The effect results from free electrons which are oscillating relatively to the positively charged metallic nanoobjects. Depending on geometry and size of the structure, different resonances are possible due to coupling of these oscillations. A famous example for these effects are bow-tie antennas [201]. These antennas can be designed to be optical active in a wavelength exceeding their own dimension. Due to the Abbe limit, it is not possible to resolve them in the far-field. Because of the Abbe limit does not exist in the near-field, a measurement of the near-field can resolve those antennas optically. An array of bow-ties was measured with the SNOM cantilever. The setup of the measurement, a SEM image of the sample and the schematic are depicted in figure 6.20. For the measurement, the antennas were illuminated through a white light laser to ensure to meet the resonance frequencies of the plasmons of the bow-ties. For this purpose, the infrared part of the white light from the Kohera SuperK Versa was separated by the IR-VIS split box at 1180 nm and coupled into the illumination fiber from the cantilever. The printed mirror on the fiber reflects the light onto the sample and tip. In the topography as well as in the SNOM image, the bow-tie antennas can be clearly

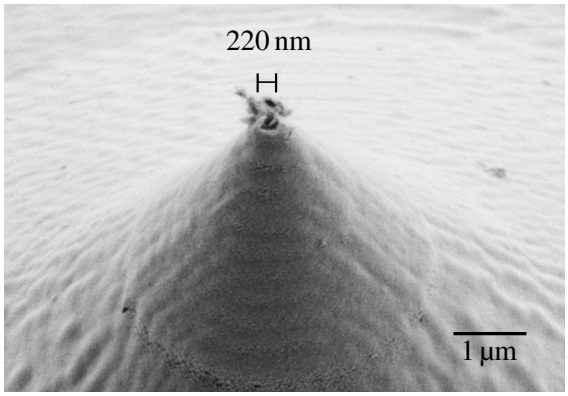

Figure 6.22: SEM image of the tip after the measurement. As expected, the gold at the tip wears off and leaves a small aperture (approximately 220 nm), which enables SNOM measurements.

distinguished from the substrate. The interpretation of SNOM images can be difficult since SNOM can suffer from different effects. One of this effects is that the topography crosstalks into the SNOM channel [202, 203]. This effect results from the offset of the topographical measuring tip and the center of the optical aperture as schematically depicted in figure 6.21. When the tip changes the distance when it is moved over a changing topography, the light collecting aperture also changes its distance, which results in a change of the collected photocurrent.

6.12 Resolution Determination

To prove a SNOM image, the effect of above mentioned topographical artifacts can be used. When the SNOM image has this kind of topographical artifacts but an additional feature which has an offset and a lower resolution, the SNOM signal is credible [204]. To prove the SNOM image, a zoom image of the bow-tie array was measured. Figure 6.21 shows this measurement. The effect described is clearly visible. The crosstalk of the topography with very high resolution shows the form of the antennas, but there is also a signal shifted to the topography. This is the true SNOM signal. To calculate the resolution, a cross section of the SNOM signal was taken and a multipeak fit for a series of Gauss curves was performed. For the fit, a baseline was set and the fit takes the overlap of the Gauss peaks into account. The mean value for all full width at half maximum (FWHM) values resulted in 363 nm. When considering that the structure has a dimension of nearly 250 nm in diameter, a resolution of $r = \sqrt{363^2 - 250^2}$ nm $= 264$ nm can be calculated. Since the resolution of a SNOM mainly depends on the diameter of the aperture [205], the cantilever tip was inspected by a SEM measurement. Figure 6.22 shows the opened tip. The tip opening is in the range of 220 nm, which is in agreement of the resolution determination from the Gauss peaks. Since the tip was opened by scanning hard over a sample, it is easy to improve the resolution by testing different forces to open the tip or use focused ion beam milling [206] which could lead to very small apertures but would also make an additional fabrication step necessary.

6.13 Summary and Conclusion

In this chapter the standard SNOM cantilever was introduced. The presented SNOM capable cantilevers used the readout principle from the standard AFM cantilever but have improved the actuation principle through two total internal reflections, to avoid the air-polymer-interface and thus reduce losses. The cantilever was investigated to match measurements and simulations to enable the predetermination of important properties prior to the production process. For illumination, a mirror was designed which was used to illuminate a non-transparent sample which is necessary for standard SNOM measurements. This saves the use of macroscopic optics. The collection of the light worked well without any whispering gallery modes which was demonstrated on measurements of illuminated single mode fibers. The near-field of a HCSE-laser was surveyed and accorded with far-field measurements. A resolution beyond the Abbe limit was demonstrated.

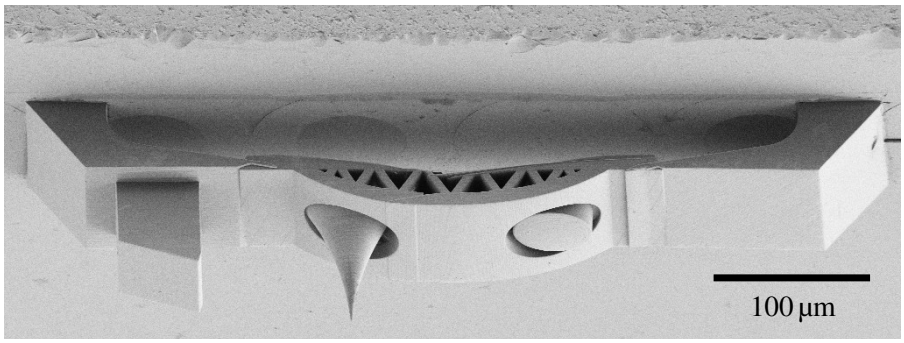

Figure 6.23: SEM image of a possible design of a future SNOM. The two constraints on the side lead to a resonance frequency nearly three times above a cantilever with one free side.

A manuscript of a shorter version of this chapter was prepared as 'Nanoprinted Scanning-Probe Microscope Engines utilizing Optical Actuation and Read-Out', Philipp-Immanuel Dietrich[1], Gerald Göring[1], Mareike Trappen, Matthias Blaicher, Thomas Schimmel, Hendrik Hölscher, Christian Koos

[1] contributed equally to this work

7 Summary and Outlook

In this thesis the possibilities of 3D printing in the field of AFM are explored and an entirely printed setup for atomic force microscopy with extended SNOM capabilities is presented. Sharp tips, with a radius of $r = 25\,\text{nm}$, were printed in different forms and shapes to fit different samples, to improve lateral resolution and to decrease or remove artifacts of an inverted imaging effect caused by an inadequate tip shape. Additionally, the fabricated polymer tips exhibit long-term stability and low wear-rates. Further investigations were related to the tuning of the resonance spectrum of vibrating cantilevers to improve scanning speed and increase or decrease specific eigenmodes.

The 3D printed system developed combines the tapping mode of traditional dynamic mode AFM and the non-diffraction limited light collection capability of a SNOM setup. The new SNOM setup can be operated without an alignment process or macroscopic optical components. For fabrication, a direct laser writing system with two-photon absorption polymerization was employed. The cantilevers produced show high resonance frequencies of 200 kHz to 300 kHz with low fabrication variances of 2 %. The cantilevers can be precisely aligned automatically using software on the utilized fiber arrays, which makes the alignment and recalibration process of the readout system of standard AFM unnecessary. This simplifies the traditionally complicated SNOM setup, which also incorporates expensive, bulky and complicated-to-align optics. Due to the integration of the optics necessary for SNOM measurements, this setup allows the measurement of samples in situ or in changing environments.

The directly written polymer tips with radii in the range of 25 nm can be designed for special applications. High aspect ratio, 30 µm long tips were written to perform measurements of deep trenches and up to 25 µm high elevating rose petals which are inaccessible for standard 10 µm to 16 µm long tips. The tips produced this way also exhibited a low wear rate over a 36 hour duration experiment. A three inch wafer, containing 120 self-sensing TMR-cantilevers, was equipped with tips in about three hours. To improve the ease of use, those tips were designed to protrude over the edge of the TMR-cantilevers so that it is possible to have a top view of the measurement area with an optical microscope during the AFM scan. Carbonization of the polymer tips is demonstrated, which offers additional possibilities for the fabrication of hard, conducting and easy to functionalize tips.

Because of low internal damping of commercial AFM probes, scan speed is limited, which restricts the investigation of dynamic properties. In order to address this problem, cantilevers were coated by 3D printing. As little as a few micrometers of polymer on top of a silicon cantilever

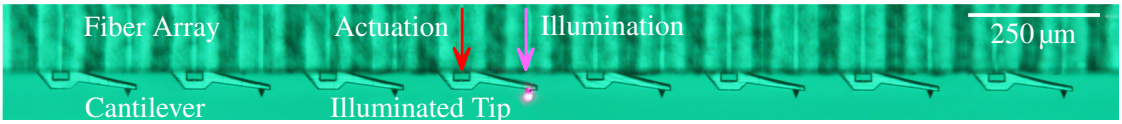

Figure 7.1: Example of a parallel setup of 8 actuated cantilevers on a fiber array with 16 fibers. Adopted from [197].

was sufficient for a threefold reduced quality factor, which directly leads to a speed improvement of the same order. Another mode of the AFM is to incorporate oscillations with higher eigenmodes than the first harmonic. This enables stable feedback, high sensitivity and the quantitative measurement of physical properties. To improve the cantilever spectrum, different frameworks were written on cantilevers to tailor it. Additionally, a substantial reduction of noise in the spectra of these cantilevers is observed.

To combine the advantages of adapted tips and high speed polymeric cantilevers, complete polymer cantilevers were written. Cantilevers with high resonance frequencies in the 200 kHz to 300 kHz range have low quality factors of between 10 to 20, which suit the specifications of high speed cantilevers. Due to the ability to produce the cantilevers directly at the desired location, it is possible to write a cantilever directly on the end of two adjacent optical fibers. The first fiber is used to photothermally actuate the cantilever by thermal expansion, whereas the second fiber forms an interferometric cavity together with the cantilever itself.

By careful evaluation of the absorption and heat transfer properties in simulation and experiment, the design and working parameters were optimized in order to achieve fast thermal response and to enable high frequency oscillations and high amplitudes. The printed setup is sensitive enough to reveal atomic steps, which are smaller than 0.35 nm, on a freshly cleaved HOPG surface. Additionally, the interferometric readout is proven to work for measurements in air, then in water and other environments, without realignment. A so-called light exhaust was designed to prevent stray light from the surface entering the readout fiber. The resonance frequency of a classical silicon cantilever reduces by around 66 % when the system is immersed in water. For hydrodynamical reasons, the 3D printed polymer cantilever reduces its resonance frequency from 143 kHz in air by 13 % to 124 kHz in water. This property enables faster scanning speeds in biological AFM investigations.

By equipping the system with an additional readout channel that collects the light through an aperture at the tip in a third fiber, the system is extended to have scanning near-field optical microscopy capabilities (SNOM). For sideways illumination, a freeform mirror, which reflects the light from a fourth fiber through a lens on the cantilever tip was designed. Mode field measurements of active components like a horizontal cavity surface-emitting laser and of passive components like plasmonic antennas, were performed and the integrated SNOM system shows sub wavelength resolution. The resonance frequency of the SNOM cantilever is around 30 to 40 times higher than the tapping mode SNOM, which was recently published.

The sensor system size is only limited by the size of the v-groove fiber array which has a dimension of 600 µm × 300 µm and can further be reduced, if needed, by using multicore fibers

with diameters in the range of 100 µm for the whole system. The production variation of the resonance frequency is proven to be $3\sigma = 6\,\%$, which is five to eight times better than for commercially available cantilevers. Because of the possibility to thermally change the resonance frequency on-the-fly by a laser intensity offset, it is possible to actuate multiple cantilevers on a large fiber array with the same resonance frequency, which raises the possibility of low cost parallel measurements for in situ quality control as indicated in figure 7.1. If small piezo tubes or a micro-electromechanical system (MEMS) were used for scanning, the size of the whole AFM system could be reduced to a size that would enable endoscopic measurements.

A List of Publications

A.1 Patents

1. Philipp-Immanuel Dietrich, Gerald Göring, Mareike Trappen, Matthias Blaicher, Hendrik Hölscher and Christian Koos
   Mikro-optomechanisches System und Verfahren zu seiner Herstellung
   PATENT 102017221952.1 (2017)

A.2 Publications

1. Gerald Göring, Philipp-Immanuel Dietrich, Matthias Blaicher, Swati Sharma, Jan G. Korvink, Thomas Schimmel, Christian Koos and Hendrik Hölscher
   Tailored probes for atomic force microscopy fabricated by two-photon Polymerization
   Applied Physics Letters 109, 063101 (2016), Cover Story and Featured Article

2. Philipp-Immanuel Dietrich, Gerald Göring, Mareike Trappen, Matthias Blaicher, Thomas Schimmel, Hendrik Hölscher and Christian Koos
   Nanoprinted Scanning-Probe Microscope Engines utilizing Optical Actuation and Read-Out
   Manuscript prepared for submission

A.3 Conference Contributions

1. Christian Koos, Wolfgang Freude, A. E. Guber, A. Schimmel, M. Lauermann, S. Schneider, C. Weimann, S. Muehlbrandt, T. Harter, S. F. Wondimu, T. Wienhold, S. von der Ecken, P. I. Dietrich and G. Göring
   Photonic Integration for Metrology and Sensing
   OSA Integrated Photonics Research, Silicon, and Nano- Photonics (IPR), New Orleans, Louisiana, USA, 24 - 27 July , paper ITh1A.1. (2017) Talk (invited)

2. Stefan Kilper, Gerald Göring, Dirk Rothenstein, Zaklina Burghard, Stefan Walheim, Thomas Schimmel and Joachim Bill
   M13 Bacteriophage / ZnO Nanowires: From Viruses to Semiconductive, Piezoelectric Nanowires
   Stuttgarter Forschungstag 2017, Stuttgart, 29.06.2017, Poster

3. Gerald Göring, Tobias Meier, Alexander Förste, Ali Tavassolizadeh, Karsten Rott, Dirk Meyners, Roland Gröger, Günter Reiss, Eckhard Quandt, Thomas Schimmel and Hendrik Hölscher
   Multifrequency AFM with Self-sensing Tunneling Magnetoresistive (TMR) Cantilevers
   Statusworkshop Nano-2016 des Kompetenznetzes, Bad Herrenalb, Talk (price: 2nd best talk)

4. Gerald Göring, Philipp-Immanuel Dietrich, Matthias Blaicher, Swati Sharma, Jan G. Korvink, Thomas Schimmel, Christian Koos and Hendrik Hölscher
   Tailored Probes for Atomic Force Microscopy Fabricated by two-Photon Polymerization
   Statusworkshop Nano-2016 des Kompetenznetzes, Bad Herrenalb, Poster

5. Raphael Schmager, Ruben Hünig, Guillaume Gomard, Benjamin Fritz, Gerald Göring, Hendrik Hölscher, Heinz Kalt, Michael Powalla and Michael Hetterich
   Bio-inspired hierarchical structures for enhanced light harvesting in solar cells
   DPG Jahrestagung 2016, Regensburg, 09.-11.March, Poster

6. Gerald Göring, Tobias Meier, Alexander Förste, Ali Tavassolizadeh, Karsten Rott, Dirk Meyners, Roland Gröger, Günter Reiss, Eckhard Quandt, Thomas Schimmel and Hendrik Hölscher
   Multifrequency AFM with Self-sensing Tunneling Magnetoresistive (TMR) Cantilevers
   DPG-Jahrestagung 2015, Berlin, 15. - 20. March 2015, Talk

List of Figures

Bibliography

[1] Ernst Abbe. Beiträge zur theorie des mikroskops und der mikroskopischen wahrnehmung. *Archiv für mikroskopische Anatomie*, pages 413 – 468, 2009.

[2] G. Binnig, H. Rohrer, Ch. Gerber, and E. Weibel. Surface studies by scanning tunneling microscopy. *Phys. Rev. Lett.*, pages 57–61, Jul 1982.

[3] Björn Neu, Gerhard Meyer, and Karl-Heinz Rieder. Controlled vertical and lateral manipulation of single atoms and molecules with the scanning tunneling microscope. *Modern Physics Letters B*, (15):963–969, 1995.

[4] G. Binnig, C. F. Quate, and Ch. Gerber. Atomic force microscope. *Phys. Rev. Lett.*, pages 930–933, Mar 1986.

[5] Bruker Nano Inc. Cantilever specification, october 2017. URL `http://www.brukerafmprobes.com/Product.aspx?ProductID=3925`.

[6] BudgetSensors Ltd. Cantilever specification, october 2017. URL `https://www.budgetsensors.com/tapping-mode-afm-probe-high-resolution-sharp-shr300`.

[7] Franz J. Giessibl. High-speed force sensor for force microscopy and profilometry utilizing a quartz tuning fork. *Applied Physics Letters*, (26):3956–3958, 1998.

[8] M. Tortonese, R. C. Barrett, and C. F. Quate. Atomic resolution with an atomic force microscope using piezoresistive detection. *Applied Physics Letters*, (8): 834–836, 1993.

[9] Sadik Hafizovic, Diego Barrettino, Tormod Volden, Jan Sedivy, Kay-Uwe Kirstein, Oliver Brand, and Andreas Hierlemann. Single-chip mechatronic microsystem for surface imaging and force response studies. *Proceedings of the National Academy of Sciences of the United States of America*, (49):17011–17015, 2004.

[10] Haider I. Rasool, Paul R. Wilkinson, Adam Z. Stieg, and James K. Gimzewski. A low noise all-fiber interferometer for high resolution frequency modulated atomic force microscopy imaging in liquids. *Review of Scientific Instruments*, (2):023703, 2010.

[11] D. Rugar, H. J. Mamin, and P. Guethner. Improved fiber-optic interferometer for atomic force microscopy. *Applied Physics Letters*, (25):2588–2590, 1989.

[12] C. Schönenberger and S. F. Alvarado. A differential interferometer for force microscopy. *Review of Scientific Instruments*, (10):3131–3134, 1989.

[13] D. Iannuzzi, K. Heeck, M. Slaman, S. De Man, J.H. Rector, H. Schreuders, Johan W. Berenschot, V.J. Gadgil, Remco G.P. Sanders, Michael Curt Elwenspoek, and S. Deladi. Fibre-top cantilevers: design, fabrication and applications. pages 3247–3252, 9 2007.

[14] J. Li, F. Albri, R. R. J. Maier, W. Shu, J. Sun, D. P. Hand, and W. N. MacPherson. A micro-machined optical fiber cantilever as a miniaturized ph sensor. *IEEE Sensors Journal*, (12):7221–7228, Dec 2015.

[15] C.W. Hull. Apparatus for production of three-dimensional objects by stereolithography, mar 1986.

[16] Markus Deubel, Georg von Freymann, Martin Wegener, Suresh Pereira, Kurt Busch, and Costas M. Soukoulis. Direct laser writing of three-dimensional photonic-crystal templates for telecommunications. *Nature Materials*, pages 444 EP –, Jun 2004.

[17] Moritz Emons, Kotaro Obata, Thomas Binhammer, Aleksandr Ovsianikov, Boris N. Chichkov, and Uwe Morgner. Two-photon polymerization technique with sub-50 nm resolution by sub-10 fs laser pulses. *Opt. Mater. Express*, (7): 942–947, Jul 2012.

[18] Philipp-Immanuel C. Dietrich, Ingo Reuter, Matthias Blaicher, Simon Schneider, Muhammad R. Billah, Tobias Hoose, Andreas Hofmann, Charles Caer, Roger Dangel, Bert Offrein, Martin Möhrle, Ute Troppenz, Marlene Zander, Wolfgang Freude, and Christian Koos. Lenses for low-loss chip-to-fiber and fiber-to-fiber coupling fabricated by 3d direct-write lithography. *Conference on Lasers and Electro-Optics*, 2016.

[19] Justyna K. Gansel, Michael Latzel, Andreas Frölich, Johannes Kaschke, Michael Thiel, and Martin Wegener. Tapered gold-helix metamaterials as improved circular polarizers. *Applied Physics Letters*, (10):101109, 2012.

[20] Avi Braun and Stefan Alexander Maier. Versatile direct laser writing lithography technique for surface enhanced infrared spectroscopy sensors. *ACS Sensors*, (9): 1155–1162, 2016.

[21] E. Betzig, A. Lewis, A. Harootunian, M. Isaacson, and E. Kratschmer. Near field scanning optical microscopy (nsom): Development and biophysical applications. *Biophysical Journal*, (1):269 – 279, 1986.

[22] Mareike Trappen. 3d-printed scanning probe microscopy. Master's thesis, Karlsruhe Institute of Technology, Germany, 2017.

[23] S. Narasimha, P. Chang, C. Ortolland, D. Fried, E. Engbrecht, K. Nummy, P. Parries, T. Ando, M. Aquilino, N. Arnold, R. Bolam, J. Cai, M. Chudzik, B. Cipriany, G. Costrini, M. Dai, J. Dechene, C. DeWan, B. Engel, M. Gribelyuk, D. Guo, G. Han, N. Habib, J. Holt, D. Ioannou, B. Jagannathan, D. Jaeger, J. Johnson, W. Kong, J. Koshy, R. Krishnan, A. Kumar, M. Kumar, J. Lee, X. Li, C. H. Lin, B. Linder, S. Lucarini, N. Lustig, P. McLaughlin, K. Onishi, V. Ontalus, R. Robison, C. Sheraw, M. Stoker, A. Thomas, G. Wang, R. Wise, L. Zhuang, G. Freeman, J. Gill, E. Maciejewski, R. Malik, J. Norum, and P. Agnello. 22nm high-performance soi technology featuring dual-embedded stressors, epi-plate high-k deep-trench embedded dram and self-aligned via 15lm beol. In *2012 International Electron Devices Meeting*, pages 3.3.1–3.3.4, Dec 2012.

[24] Leo Gross, Fabian Mohn, Nikolaj Moll, Peter Liljeroth, and Gerhard Meyer. The chemical structure of a molecule resolved by atomic force microscopy. *Science*, (5944):1110–1114, 2009.

[25] F. Ohnesorge and G. Binnig. True atomic resolution by atomic force microscopy through repulsive and attractive forces. *Science*, (5113):1451–1456, 1993.

[26] Ruby May A. Sullan, Allison B. Churnside, Duc M. Nguyen, Matthew S. Bull, and Thomas T. Perkins. Atomic force microscopy with sub-piconewton force stability for biological applications. *Methods*, (2):131–141, Apr 2013.

[27] Constant A. J. Putman, Bart G. De Grooth, Niek F. Van Hulst, and Jan Greve. A detailed analysis of the optical beam deflection technique for use in atomic force microscopy. *Journal of Applied Physics*, (1):6–12, 1992.

[28] Max Born and Emil Wolf. *Principles of Optics: Electromagnetic Theory of Propagation, Interference and Diffraction of Light*. Cambridge University Press, 1999. ISBN 0521642221.

[29] S. Nemoto and T. Makimoto. Analysis of splice loss in single-mode fibres using a gaussian field approximation. *Optical and Quantum Electronics*, (5):447–457, Sep 1979.

[30] Antje Bergmann, Daniela Feigl, David Kuhn, Manuel Schaupp, Günter Quast, Kurt Busch, Ludwig Eichner, and Jens Schumacher. A low-cost afm setup with an interferometer for undergraduates and secondary-school students. *European Journal of Physics*, (4):901, 2013.

[31] V. Melissinaki, M. Farsari, and S. Pissadakis. A fiber-endface, fabry-perot vapor microsensor fabricated by multiphoton polymerization. *IEEE Journal of Selected Topics in Quantum Electronics*, (4):344–353, July 2015.

[32] Franz J. Giessibl. Atomic resolution on si(111)-(7x7) by noncontact atomic force microscopy with a force sensor based on a quartz tuning fork. *Applied Physics Letters*, (11):1470–1472, 2000.

[33] S. Hembacher, F.J. Giessibl, and J. Mannhart. Evaluation of a force sensor based on a quartz tuning fork for operation at low temperatures and ultrahigh vacuum. *Applied Surface Science*, (3):445 – 449, 2002.

[34] M. Tortonese, H. Yamada, R. C. Barrett, and C. F. Quate. Atomic force microscopy using a piezoresistive cantilever. In *Solid-State Sensors and Actuators, 1991. Digest of Technical Papers, TRANSDUCERS '91., 1991 International Conference on*, pages 448–451, June 1991.

[35] J. Tansock and C.C. Williams. Force measurement with a piezoelectric cantilever in a scanning force microscope. *Ultramicroscopy*, (Part 2):1464 – 1469, 1992.

[36] Gabi Neubauer, Sidney R. Cohen, Gary M. McClelland, Don Horne, and C. Mathew Mate. Force microscopy with a bidirectional capacitance sensor. *Review of Scientific Instruments*, (9):2296–2308, 1990.

[37] Joseph C Doll and Beth L Pruitt. Design of piezoresistive versus piezoelectric contact mode scanning probes. *Journal of Micromechanics and Microengineering*, (9):095023, 2010.

[38] T. S. Plaskett, P. P. Freitas, N. P. Barradas, M. F. da Silva, and J. C. Soares. Magnetoresistance and magnetic properties of nife/oxide/co junctions prepared by magnetron sputtering. *Journal of Applied Physics*, (10):6104–6106, 1994.

[39] J. S. Moodera, Lisa R. Kinder, Terrilyn M. Wong, and R. Meservey. Large magnetoresistance at room temperature in ferromagnetic thin film tunnel junctions. *Phys. Rev. Lett.*, pages 3273–3276, Apr 1995.

[40] C. Albon, A. Weddemann, A. Auge, K. Rott, and A. Hütten. Tunneling magnetoresistance sensors for high resolutive particle detection. *Applied Physics Letters*, (2):023101, 2009.

[41] D. Meyners, T. von Hofe, M. Vieth, M. Rührig, S. Schmitt, and E. Quandt. Pressure sensor based on magnetic tunnel junctions. *Journal of Applied Physics*, (7): 07C914, 2009.

[42] William Thomson. Xix. on the electro-dynamic qualities of metals:-effects of magnetization on the electric conductivity of nickel and of iron. *Proceedings of the Royal Society of London*, pages 546–550, 1857.

[43] P. Grünberg, R. Schreiber, Y. Pang, M. B. Brodsky, and H. Sowers. Layered magnetic structures: Evidence for antiferromagnetic coupling of fe layers across cr interlayers. *Phys. Rev. Lett.*, pages 2442–2445, Nov 1986.

[44] M. Julliere. Tunneling between ferromagnetic films. *Physics Letters A*, (3):225 – 226, 1975.

[45] T. Miyazaki, T. Yaoi, and S. Ishio. Large magnetoresistance effect in 82ni-fe/al-al2o3/co magnetic tunneling junction. *Journal of Magnetism and Magnetic Materials*, (1):L7 – L9, 1991.

[46] W. H. Butler, X.-G. Zhang, T. C. Schulthess, and J. M. MacLaren. Spin-dependent tunneling conductance of Fe|MgO|Fe sandwiches. *Phys. Rev. B*, page 054416, Jan 2001.

[47] J. Mathon and A. Umerski. Theory of tunneling magnetoresistance of an epitaxial fe/mgo/fe(001) junction. *Phys. Rev. B*, page 220403, May 2001.

[48] John G. Simmons. Generalized formula for the electric tunnel effect between similar electrodes separated by a thin insulating film. *Journal of Applied Physics*, (6):1793–1803, 1963.

[49] Jian-Gang Zhu and Chando Park. Magnetic tunnel junctions. *Materials Today*, (11):36 – 45, 2006.

[50] M. Löhndorf, T. Duenas, M. Tewes, E. Quandt, M. R/"uhrig, and J. Wecker. Highly sensitive strain sensors based on magnetic tunneling junctions. *Applied Physics Letters*, (2):313–315, 2002.

[51] Robert C. O'Handley. *Modern Magnetic Materials: Principles and Applications*. Wiley-Interscience, 1999. ISBN 0471155667.

[52] Tobias Meier. *Magnetoresistive and Thermoresistive Scanning Probe Microscopy with Applications (Schriften des Instituts fuer Mikrostrukturtechnik am Karlsruher Institut fuer Technologie) (dddvolume 25)*. Karlsruhe Scientific Publishing, 2014. ISBN 3731502534.

[53] Jacob N. Israelachvili. *Intermolecular and Surface Forces, Third Edition*. Academic Press, 2010. ISBN 0123751829.

[54] Bert Voigtländer. *Scanning Probe Microscopy: Atomic Force Microscopy and Scanning Tunneling Microscopy (NanoScience and Technology)*. Springer, 2015. ISBN 3662452391.

[55] H.C. Hamaker. The london-van der waals attraction between spherical particles. *Physica*, (10):1058 – 1072, 1937.

[56] Jacob N. Israelachvili. *Intermolecular and Surface Forces, Third Edition*. Academic Press, 2010. ISBN 0123751829.

[57] M. Saint Jean, S. Hudlet, C. Guthmann, and J. Berger. Van der waals and capacitive forces in atomic force microscopies. *Journal of Applied Physics*, (9): 5245–5248, 1999.

[58] W. Pauli. Über den einfluß der geschwindigkeitsabhängigkeit der elektronenmasse auf den zeemaneffekt. *Zeitschrift für Physik*, (1):373–385, Feb 1925.

[59] W. Pauli. Über den zusammenhang des abschlusses der elektronengruppen im atom mit der komplexstruktur der spektren. *Zeitschrift für Physik*, (1):765–783, Feb 1925.

[60] G. E. UHLENBECK and S. GOUDSMIT. Spinning electrons and the structure of spectra. *Nature*, pages 264 EP –, Feb 1926.

[61] G. E. Uhlenbeck and S. Goudsmit. Ersetzung der Hypothese vom unmechanischen Zwang durch eine Forderung bezüglich des inneren Verhaltens jedes einzelnen Elektrons. *Naturwissenschaften*, pages 953–954, November 1925.

[62] Joost W. van Honschoten, Nataliya Brunets, and Niels R. Tas. Capillarity at the nanoscale. *Chem. Soc. Rev.*, pages 1096–1114, 2010.

[63] J. Freund, J. Halbritter, and J.K.H. Hörber. How dry are dried samples? water adsorption measured by stm. *Microscopy Research and Technique*, (5):327–338, 1999.

[64] D. A. Grigg, P. E. Russell, and J. E. Griffith. Tip-sample forces in scanning probe microscopy in air and vacuum. *Journal of Vacuum Science & Technology A: Vacuum, Surfaces, and Films*, (4):680–683, 1992.

[65] David R. Lide. *CRC Handbook Chemistry and Physics, 85th Edition*. CRC Press, 2004. ISBN 0849304857.

[66] J. J. Roa, G. Oncins, J. Diaz, F. Sanz, and M. Segarra. Calculation of young's modulus value by means of afm. *Recent Patents on Napppnotechnology*, (1): 27–36, 2011.

[67] Ranjan Grover, Brendan McCarthy, Dror Sarid, and Ibrahim Guven. Mapping thermal conductivity using bimetallic atomic force microscopy probes. *Applied Physics Letters*, (23):233501, 2006.

[68] J. A. Christman, H. Maiwa, S.-H. Kim, A. I. Kingon, and R. J. Nemanich. Piezoelectric measurements with atomic force microscopy. 1998.

[69] Kanan P. Puntambekar, Paul V. Pesavento, and C. Daniel Frisbie. Surface potential profiling and contact resistance measurements on operating pentacene thin-film transistors by kelvin probe force microscopy. *Applied Physics Letters*, (26):5539–5541, 2003.

[70] Udo D. Schwarz, Hendrik Hölscher, and Roland Wiesendanger. Atomic resolution in scanning force microscopy: Concepts, requirements, contrast mechanisms, and image interpretation. *Phys. Rev. B*, pages 13089–13097, Nov 2000.

[71] Glenn C. Ratcliff, Dorothy A. Erie, and Richard Superfine. Photothermal modulation for oscillating mode atomic force microscopy in solution. *Applied Physics Letters*, (15):1911–1913, 1998.

[72] Wenhai Han, S. M. Lindsay, and Tianwei Jing. A magnetically driven oscillating probe microscope for operation in liquids. *Applied Physics Letters*, (26):4111–4113, 1996.

[73] H. Hölscher, D. Ebeling, and U. D. Schwarz. Theory of q-controlled dynamic force microscopy in air. *Journal of Applied Physics*, (8):084311, 2006.

[74] U Dürig. Interaction sensing in dynamic force microscopy. *New Journal of Physics*, (1):5, 2000.

[75] John E Sader, Takayuki Uchihashi, Michael J Higgins, Alan Farrell, Yoshikazu Nakayama, and Suzanne P Jarvis. Quantitative force measurements using frequency modulation atomic force microscopy - theoretical foundations. *Napppnotechnology*, (3):S94, 2005.

[76] J. P. Cleveland, B. Anczykowski, A. E. Schmid, and V. B. Elings. Energy dissipation in tapping-mode atomic force microscopy. *Applied Physics Letters*, (20): 2613–2615, 1998.

[77] F J Giessibl, S Hembacher, M Herz, Ch Schiller, and J Mannhart. Stability considerations and implementation of cantilevers allowing dynamic force microscopy with optimal resolution: the qplus sensor. *Napppnotechnology*, (2):S79, 2004.

[78] Franz J. Giessibl, Hartmut Bielefeldt, Stefan Hembacher, and Jochen Mannhart. Calculation of the optimal imaging parameters for frequency modulation atomic force microscopy. *Applied Surface Science*, (3):352 – 357, 1999.

[79] Jose R. Lozano and Ricardo Garcia. Theory of multifrequency atomic force microscopy. *Phys. Rev. Lett.*, page 076102, Feb 2008.

[80] Ricardo García and Elena T. Herruzo. The emergence of multifrequency force microscopy. *Nat Nano*, (4):217–226, Apr 2012.

[81] Suryendra D. Sherman, Arjan Quist, and Paul Hansma. Relationship between stickiness and surface roughness of composite materials: Atomic force microscopy and intermolecular adhesion force measurement. *Journal of Nano Research*, pages 225–235, 6 2009.

[82] Frank W. S. Stetter, Sandra Kienle, Stefanie Krysiak, and Thorsten Hugel. Investigating single molecule adhesion by atomic force spectroscopy. *J Vis Exp*, (96): 52456, Feb 2015.

[83] Mariano Carrion-Vazquez, Andres F. Oberhauser, Susan B. Fowler, Piotr E. Marszalek, Sheldon E. Broedel, Jane Clarke, and Julio M. Fernandez. Mechanical and chemical unfolding of a single protein: A comparison. *Proc Natl Acad Sci U S A*, (7):3694–3699, Mar 1999.

[84] Mark A. Poggi, Andrew W. McFarland, Jonathan S. Colton, and Lawrence A. Bottomley. A method for calculating the spring constant of atomic force microscopy cantilevers with a nonrectangular cross section. *Analytical Chemistry*, (4):1192–1195, 2005.

[85] Tilman E. Schäffer and Harald Fuchs. Optimized detection of normal vibration modes of atomic force microscope cantilevers with the optical beam deflection method. *Journal of Applied Physics*, (8):083524, 2005.

[86] D. A. Walters, J. P. Cleveland, N. H. Thomson, P. K. Hansma, M. A. Wendman, G. Gdddurley, and V. Elings. Short cantilevers for atomic force microscopy. *Review of Scientific Instruments*, (10):3583–3590, 1996.

[87] Jonathan D. Adams, Blake W. Erickson, Jonas Grossenbacher, Juergen Brugger, Adrian Nievergelt, and Georg E. Fantner. Harnessing the damping properties of materials for high-speed atomic force microscopy. *Nat Nano*, (2):147–151, Feb 2016.

[88] K. Y. Yasumura, T. D. Stowe, E. M. Chow, T. Pfafman, T. W. Kenny, B. C. Stipe, and D. Rugar. Quality factors in micron- and submicron-thick cantilevers. *Journal of Microelectromechanical Systems*, (1):117–125, March 2000.

[89] J. Mertz, O. Marti, and J. Mlynek. Regulation of a microcantilever response by force feedback. *Applied Physics Letters*, (19):2344–2346, 1993.

[90] T. Hartmann, R. Gatz, W. Wiegräbe, A. Kramer, A. Hillebrand, K. Lieberman, W. Baumeister, and R. Guckenberger. *Near Field Optics (Nato Science Series E:)*. Springer, 2012. ISBN 9401048738.

[91] Sarah Frisken Gibson and Frederick Lanni. Experimental test of an analytical model of aberration in an oil-immersion objective lens used in three-dimensional light microscopy. *J. Opt. Soc. Am. A*, (1):154–166, Jan 1992.

[92] Bert Hecht, Beate Sick, Urs P. Wild, Volker Deckert, Renato Zenobi, Olivier J. F. Martin, and Dieter W. Pohl. Scanning near-field optical microscopy with aperture probes: Fundamentals and applications. *The Journal of Chemical Physics*, (18): 7761–7774, 2000.

[93] Lukas Novotny and Bert Hecht. Principles of nano-optics, 2012.

[94] Tomasz J. Antosiewicz, Marian Marciniak, and Tomasz Szoplik. *Photonic Crystals: Physics and Technology*. Springer Milan, Milano, 2008. ISBN 978-88-470-0844-1.

[95] Khaled Karrai and Robert D. Grober. Piezoelectric tip-sample distance control for near field optical microscopes. *Applied Physics Letters*, (14):1842–1844, 1995.

[96] G. Longo, M. Girasole, and A. Cricenti. A novel tapping snom: Specifications and performances. *physica status solidi (b)*, (15):3070–3074, 2005.

[97] F. Zenhausern, Y. Martin, and H. K. Wickramasinghe. Scanning interferometric apertureless microscopy: Optical imaging at 10 angstrom resolution. *Science*, (5227):1083–1085, 1995.

[98] Gerd Kaupp and Andreas Herrmann. Scanning near-field optical microscopy by near-field reflectance enhancement: a versatile and valid technique. *Journal of Physical Organic Chemistry*, (2):141–143, 1999.

[99] Fleischer Monika. *ntrev*, chapter Near-field scanning optical microscopy nanoprobes, page 313. 2017 2012.

[100] Tommaso Baldacchini. *Three-Dimensional Microfabrication Using Two-Photon Polymerization: Fundamentals, Technology, and Applications (Micro and Nano Technologies)*. William Andrew, 2015. ISBN 0323353215.

[101] Osamu Nakamura. Three-dimensional imaging characteristics of laser scan fluorescence microscopy: Two-photon excitation vs. single-photon excitation. *Optik*, (1):39–42, 1993.

[102] Shoji Maruo, Osamu Nakamura, and Satoshi Kawata. Three-dimensional microfabrication with two-photon-absorbed photopolymerization. *Opt. Lett.*, (2): 132–134, Jan 1997.

[103] Nanoscribe GmbH. Datasheet: Ip-photoresists, october 2017. URL `http://www.nanoscribe.de/files/1814/0662/4393/IP-Resist_IP-Dip_web.pdf`.

[104] Mo Li, Hong X Tang, and Michael L Roukes. *Scanning Probe Microscopy - The Lab on a Tip*. Springer Verlag, 2004.

[105] P. Eaton and P. West. *Atomic Force Microscopy*. Oxford University Press, 2010.

[106] U. D. SCHWARZ, H. HAEFKE, P. REIMANN, and H.-J. GüNTHERODT. Tip artefacts in scanning force microscopy. *Journal of Microscopy*, (3):183–197, 1994.

[107] Hui Xie, Danish Hussain, Feng Yang, and Lining Sun. Atomic force microscopy deep trench and sidewall imaging with an optical fiber probe. *Review of Scientific Instruments*, (12):123704, 2014.

[108] Bernard Mesa and Sergei Magonov. Novel diamond/sapphire probes for scanning probe microscopy applications. *Journal of Physics: Conference Series*, (1):770, 2007.

[109] Neil R. Wilson and Julie V. Macpherson. Carbon nanotube tips for atomic force microscopy. *Nat Nano*, (8):483–491, Aug 2009.

[110] P Neuzil and R Nagarajan. The formation of sharp afm tips by single step etching. *Journal of Micromechanics and Microengineering*, (7):1298, 2006.

[111] Jong Min Kim and Hiroshi Muramatsu. Two-photon photopolymerized tips for adhesion-free scanning-probe microscopy. *Nano Letters*, (2):309–314, 2005.

[112] Woo-Sik Kim, Kang-Min Park, Jung Jin Park, Sang-Mok Chang, In-Ho Kim, Hiroshi Muramatsu, and Jong Min Kim. Polymer tips for application of atomic force microscopy. *Current Applied Physics*, (5):528 – 531, 2007.

[113] Byung Je Jung, Hong Jin Kong, Yong-Hoon Cho, Chung Hyun Park, Min Kwan Kim, Byoung Goo Jeon, Dong-Yol Yang, and Kwang-Sup Lee. Fabrication of 15 nm curvature radius polymer tip probe on an optical fiber via two-photon polymerization and o2-plasma ashing. *Current Applied Physics*, (9):2064 – 2069, 2013.

[114] Jae Seol Lee, Jungki Song, Seong Oh Kim, Seokbeom Kim, Wooju Lee, Joshua A. Jackman, Dongchoul Kim, Nam-Joon Cho, and Jungchul Lee. Multifunctional hydrogel nano-probes for atomic force microscopy. pages 11566 EP –, May 2016.

[115] Gerald Göring, Philipp-Immanuel Dietrich, Matthias Blaicher, Swati Sharma, Jan G. Korvink, Thomas Schimmel, Christian Koos, and Hendrik Hölscher. Tailored probes for atomic force microscopy fabricated by two-photon polymerization. *Applied Physics Letters*, (6):063101, 2016.

[116] Sergei Magonov. *Surface analysis with STM and AFM : experimental and theoretical aspects of image analysis*. VCH, Weinheim New York, 1996. ISBN 978-3-527-61510-0.

[117] Y. F. Wang, J. I. Kilpatrick, S. P. Jarvis, F. M. Frank Boland, A. Kokaram, and D. Corrigan. Double-tip artifact removal from atomic force microscopy images. *IEEE Transactions on Image Processing*, (6):2774–2788, June 2016.

[118] Peter Markiewicz and M. Cynthia Goh. Simulation of atomic force microscope tip-sample / sample-tip reconstruction. *Journal of Vacuum Science & Technology B: Microelectronics and Nanometer Structures Processing, Measurement, and Phenomena*, (3):1115–1118, 1995.

[119] Tobias Meier, Alexander Förste, Ali Tavassolizadeh, Karsten Rott, Dirk Meyners, Roland Gröger, Günter Reiss, Eckhard Quandt, Thomas Schimmel, and Hendrik Hölscher. A scanning probe microscope for magnetoresistive cantilevers utilizing a nested scanner design for large-area scans. *Beilstein Journal of Napppnotechnology*, pages 451–461, 2015.

[120] Ali Tavassolizadeh, Karsten Rott, Tobias Meier, Eckhard Quandt, Hendrik Hölscher, Günter Reiss, and Dirk Meyners. Tunnel magnetoresistance sensors with magnetostrictive electrodes: Strain sensors. *Sensors (Basel)*, (11):1902, Nov 2016.

[121] L. H. Mak, M. Knoll, D. Weiner, A. Gorschlüter, A. Schirmeisen, and H. Fuchs. Reproducible attachment of micrometer sized particles to atomic force microscopy cantilevers. *Review of Scientific Instruments*, (4):046104, 2006.

[122] Franz J. Giessibl. Advances in atomic force microscopy. *Rev. Mod. Phys.*, pages 949–983, Jul 2003.

[123] Nicolas F Martínez and Ricardo García. Measuring phase shifts and energy dissipation with amplitude modulation atomic force microscopy. *Napppnotechnology*, (7):S167, 2006.

[124] Hongyu Ximen and Phillip E. Russell. Microfabrication of afm tips using focused ion and electron beam techniques. *Ultramicroscopy*, pages 1526 – 1532, 1992.

[125] Johannes H Kindt, Georg E Fantner, James B Thompson, and Paul K Hansma. Automated wafer-scale fabrication of electron beam deposited tips for atomic force microscopes using pattern recognition. *Napppnotechnology*, (9):1131, 2004.

[126] R. Kuse, S. Schuster, H. Schübbe, S. Dix, and K. Hausmann. Blood lymphocyte dddvolumes and diameters in patients with chronic lymphocytic leukemia and normal controls. *Blut*, (4):243–248, Apr 1985.

[127] Christian Obermair, Andreas Wagner, and Thomas Schimmel. The atomic force microscope as a mechano-electrochemical pen. *Beilstein Journal of Napppnotechnology*, pages 659–664, 2011.

[128] John E. Sader, James W. M. Chon, and Paul Mulvaney. Calibration of rectangular atomic force microscope cantilevers. *Review of Scientific Instruments*, (10):3967–3969, 1999.

[129] John E. Sader, Ian Larson, Paul Mulvaney, and Lee R. White. Method for the calibration of atomic force microscope cantilevers. *Review of Scientific Instruments*, (7):3789–3798, 1995.

[130] Ruben Hünig, Adrian Mertens, Moritz Stephan, Alexander Schulz, Benjamin Richter, Michael Hetterich, Michael Powalla, Uli Lemmer, Alexander Colsmann, and Guillaume Gomard. Flower power: Exploiting plants' epidermal structures for enhanced light harvesting in thin-film solar cells. *Advanced Optical Materials*, (10):1487–1493, 2016.

[131] Bert Stegemann, H Backhaus, H Kloss, and E Santner. Spherical afm probes for adhesion force measurements on metal single crystals. *Modern Research and Educational Topics in Microscopy*, 07 2007.

[132] Changgu Lee, Xiaoding Wei, Jeffrey W. Kysar, and James Hone. Measurement of the elastic properties and intrinsic strength of monolayer graphene. *Science*, (5887):385–388, 2008.

[133] K. L. Johnson. *Contact Mechanics*. Cambridge University Press, 1985.

[134] Heinrich Rudolf Hertz. Über die berührung fester elastischer körper und über die härte. *Verhandlungen des Vereins zur Beförderung des Gewerbfleiẅes, Berlin : Verein zur Beförderung des Gewerbefleisses*, pages 449 – 463, 2006.

[135] B. V. Derjaguin, V. M. Muller, and Yu. P. Toporov. Effect of contact deformations on the adhesion of particles. *Journal of Colloid and Interface Science*, (2):314 – 326, 1975.

[136] K.L. Johnson, K Kendall, , and A.D. Roberts. Surface energy and the contact of elastic solids. *Proceedings of the Royal Society of London A: Mathematical, Physical and Engineering Sciences*, (1558):301–313, 1971.

[137] W.C. Oliver and G.M. Pharr. An improved technique for determining hardness and elastic modulus using load and displacement sensing indentation experiments. *Journal of Materials Research*, (6):1564–1583, 1992.

[138] Swati Sharma, Ashutosh Sharma, Yoon-Kyoung Cho, and Marc Madou. Increased graphitization in electrospun single suspended carbon nanowires integrated with carbon-mems and carbon-nems platforms. *ACS Applied Materials & Interfaces*, (1):34–39, 2012.

[139] J. Bauer, A. Schroer, R. Schwaiger, and O. Kraft. Approaching theoretical strength in glassy carbon nanolattices. *Nat Mater*, (4):438–443, Apr 2016.

[140] Jens Bauer, Almut Schroer, Ruth Schwaiger, and Oliver Kraft. Approaching theoretical strength in glassy carbon nanolattices. pages 438–443, 02 2016.

[141] Olivier J. A. Schueller, Scott T. Brittain, Christian Marzolin, and G. M. Whitesides. Fabrication and characterization of glassy carbon mems. *Chemistry of Materials*, (6):1399–1406, 1997.

[142] Swati Sharma and Marc Madou. Micro and nano patterning of carbon electrodes for biomems. *Bioinspired, Biomimetic and Nanobiomaterials*, (4):252–265, 2012.

[143] Santiago D. Solares and Hendrik Hölscher. dddnumberical analysis of dynamic force spectroscopy using a dual-oscillator sensor. *Journal of Vacuum Science & Technology B, Napppnotechnology and Microelectronics: Materials, Processing, Measurement, and Phenomena*, (3):C4E1–C4E11, 2010.

[144] Santiago D Solares and Hendrik Hölscher. dddnumberical analysis of dynamic force spectroscopy using the torsional harmonic cantilever. *Napppnotechnology*, (7):075702, 2010.

[145] Adam U Kareem and Santiago D Solares. Characterization of surface stiffness and probe-sample dissipation using the band excitation method of atomic force microscopy: a dddnumberical analysis. *Napppnotechnology*, (1):015706, 2012.

[146] Stephen Jesse, Sergei V Kalinin, Roger Proksch, A P Baddorf, and B J Rodriguez. The band excitation method in scanning probe microscopy for rapid mapping of energy dissipation on the nanoscale. *Napppnotechnology*, (43):435503, 2007.

[147] Constant A. J. Putman, Kees O. Van der Werf, Bart G. De Grooth, Niek F. Van Hulst, and Jan Greve. Tapping mode atomic force microscopy in liquid. *Applied Physics Letters*, (18):2454–2456, 1994.

[148] Jeanne Hossenlopp, Lizhong Jiang, Richard Cernosek, and Fabien Josse. Characterization of epoxy resin (su-8) film using thickness-shear mode (tsm) resonator under various conditions. *Journal of Polymer Science Part B: Polymer Physics*, (12):2373–2384, 2004.

[149] E. Meyer, H. J. Hug, and R. Bennewitz. Ultra-sensitive nems-based cantilevers for sensing, scanned probe and very high-frequency applications. *Nature napppnotechnology*, (2):114–120, 2007.

[150] R. KASSIES, K. O. VAN DER WERF, A. LENFERINK, C. N. HUNTER, J. D. OLSEN, V. SUBRAMANIAM, and C. OTTO. Combined afm and confocal fluorescence microscope for applications in bio-napppnotechnology. *Journal of Microscopy*, (1):109–116, 2005.

[151] Klony Lieberman, Nily Ben-Ami, and Aaron Lewis. A fully integrated near-field optical, far-field optical, and normal-force scanned probe microscope. *Review of Scientific Instruments*, (10):3567–3572, 1996.

[152] Toshio Ando, Noriyuki Kodera, Eisuke Takai, Daisuke Maruyama, Kiwamu Saito, and Akitoshi Toda. A high-speed atomic force microscope for studying biological macromolecules. *Proceedings of the National Academy of Sciences*, (22):12468–12472, 2001.

[153] M Antognozzi, A Ulcinas, L Picco, S H Simpson, P J Heard, M D Szczelkun, B Brenner, and M J Miles. A new detection system for extremely small vertically mounted cantilevers. *Napppnotechnology*, (38):384002, 2008.

[154] Mo Li, TangH X., and RoukesM L. Ultra-sensitive nems-based cantilevers for sensing, scanned probe and very high-frequency applications. *Nat Nano*, (2): 114–120, Feb 2007.

[155] Tomas R. Rodríguez and Ricardo García. Theory of q control in atomic force microscopy. *Applied Physics Letters*, (26):4821–4823, 2003.

[156] Liwei Chen, Xuechun Yu, and Dan Wang. Cantilever dynamics and quality factor control in ac mode afm height measurements. *Ultramicroscopy*, (4):275 – 280, 2007.

[157] Timo Gissibl, Sebastian Wagner, Jachym Sykora, Michael Schmid, and Harald Giessen. Refractive index measurements of photo-resists for three-dimensional direct laser writing. *Opt. Mater. Express*, (7):2293–2298, Jul 2017.

[158] Oscar Custance, Ruben Perez, and Seizo Morita. Atomic force microscopy as a tool for atom manipulation. *Nat Nano*, (12):803–810, Dec 2009.

[159] Ricardo García, Armin W. Knoll, and Elisa Riedo. Advanced scanning probe lithography. *Nat Nano*, (8):577–587, Aug 2014.

[160] Koo-Hyun Chung. Wear characteristics of atomic force microscopy tips: A reivew. *International Journal of Precision Engineering and Manufacturing*, (10): 2219–2230, Oct 2014.

[161] David Alsteens, Hermann E. Gaub, Richard Newton, Moritz Pfreundschuh, Christoph Gerber, and Daniel J. Müller. Atomic force microscopy-based characterization and design of biointerfaces. pages 17008 EP –, Mar 2017.

[162] Gheorghe Cojoc, Carlo Liberale, Patrizio Candeloro, F Gentile, Gobind Das, Francesco De angelis, and Enzo Di Fabrizio. Optical micro-structures fabricated on top of optical fibers by means of two-photon photopolymerization. pages 876–879, 05 2010.

[163] Timo Gissibl, Simon Thiele, Alois Herkommer, and Harald Giessen. Sub-micrometre accurate free-form optics by three-dimensional printing on single-mode fibres. *Nat Commun*, page 11763, Jun 2016.

[164] Timo Gissibl, Simon Thiele, Alois Herkommer, and Harald Giessen. Two-photon direct laser writing of ultracompact multi-lens objectives. *Nat Photon*, (8):554–560, Aug 2016.

[165] Hui Wang, Zhenwei Xie, Mile Zhang, Hailin Cui, Jingsuo He, Shengfei Feng, Xinke Wang, Wenfeng Sun, Jiasheng Ye, Peng Han, and Yan Zhang. A miniaturized optical fiber microphone with concentric nanorings grating and microsprings structured diaphragm. 08 2015.

[166] Zahra Faraji Rad, Robert E. Nordon, Carl J. Anthony, Lynne Bilston, Philip D. Prewett, Ji-Youn Arns, Christoph H. Arns, Liangchi Zhang, and Graham J. Davies. High-fidelity replication of thermoplastic microneedles with open microfluidic channels. *Microsystems &Amp; Nanoengineering*, pages 17034 EP –, Oct 2017.

[167] Seizo Morita, Franz J. Giessibl, and Roland Wiesendanger. *Noncontact Atomic Force Microscopy*. Springer, Berlin, Heidelberg, dddvolume 2 edition, 2009. ISBN 978-3-642-01495-6.

[168] Nikodem Tomczak. *Scanning Probe Microscopy*. World Scientific Publishing Company, 2010. ISBN 9814324760.

[169] Aleksander Labuda, Jason Cleveland, Nicholas A Geisse, Marta Kocun, Ben Ohler, Roger Proksch, Mario B Viani, and Deron Walters. Photothermal excitation for improved cantilever drive performance in tapping mode atomic force microscopy.

[170] Daniel Kiracofe, Kei Kobayashi, Aleksander Labuda, Arvind Raman, and Hirofumi Yamada. High efficiency laser photothermal excitation of microcantilever vibrations in air and liquids. *Review of Scientific Instruments*, (1):013702, 2011.

[171] Drew R. Evans, Ponlawat Tayati, Hongjie An, Ping Koy Lam, Vincent S. J. Craig, and Tim J. Senden. Laser actuation of cantilevers for picometre amplitude dynamic force microscopy. pages 5567 EP –, Jul 2014.

[172] E. D. Lemma, F. Rizzi, T. Dattoma, B. Spagnolo, L. Sileo, A. Qualtieri, M. De Vittorio, and F. Pisanello. Mechanical properties tunability of three-dimensional polymeric structures in two-photon lithography. *IEEE Transactions on Napppnotechnology*, (1):23–31, Jan 2017.

[173] Jingyuan Qu, Muamer Kadic, Andreas Naber, and Martin Wegener. Microstructured two-component 3d metamaterials with negative thermal-expansion coefficient from positive constituents. page 40643 EP, Jan 2017.

[174] Omega.com. Table of total emissivity, october 2017. URL `http://www.omega.com`.

[175] William S. Janna. *Engineering Heat Transfer, Third Edition*. CRC Press, 2009. ISBN 1420072021.

[176] P. B. Johnson and R. W. Christy. Optical constants of the noble metals. *Phys. Rev. B*, pages 4370–4379, Dec 1972.

[177] Michael G. Ruppert, Anthony G. Fowler, Mohammad Maroufi, and S. O. Reza Moheimani. On-Chip Dynamic Mode Atomic Force Microscopy: A Silicon-on-Insulator MEMS Approach. *JOURNAL OF MICROELECTROMECHANICAL SYSTEMS*, (1):215–225, FEB 2017.

[178] H. P. Lang, R. Berger, C. Andreoli, J. Brugger, M. Despont, P. Vettiger, Ch. Gerber, J. K. Gimzewski, J. P. Ramseyer, E. Meyer, and H.-J. Güntherodt. Sequential position readout from arrays of micromechanical cantilever sensors. *Applied Physics Letters*, (3):383–385, 1998.

[179] S. C. Minne, J. D. Adams, G. Yaralioglu, S. R. Manalis, A. Atalar, and C. F. Quate. Centimeter scale atomic force microscope imaging and lithography. *Applied Physics Letters*, (12):1742–1744, 1998.

[180] S. C. Minne, S. R. Manalis, and C. F. Quate. Parallel atomic force microscopy using cantilevers with integrated piezoresistive sensors and integrated piezoelectric actuators. *Applied Physics Letters*, (26):3918–3920, 1995.

[181] N. Lagakos, J. Jarzynski, J. H. Cole, and J. A. Bucaro. Frequency and temperature dependence of elastic moduli of polymers. *Journal of Applied Physics*, (12):4017–4031, 1986.

[182] Robert F. Landel and Lawrence E. Nielsen. *Mechanical Properties of Polymers and Composites, Second Edition (Mechanical Engineering)*. CRC Press, 1993. ISBN 0824789644.

[183] SQS Fiberoptics. Datasheet v-grooves and fiber optics arrays, october 2017. URL http://www.sqs-fiberoptics.com/data/produkty/v-grooves-fiber-optic-arrays/v-grooves-fiber-optic-arrays.pdf.

[184] K. Koyabu, F. Ohira, and T. Yamamoto. Fabrication of two-dimensional fiber arrays using microferrules. *IEEE Transactions on Components, Packaging, and Manufacturing Technology: Part C*, (1):11–19, Jan 1998.

[185] PETER TRUCANO and RUEY CHEN. Structure of graphite by neutron diffraction. *Nature*, (5531):136–137, Nov 1975.

[186] U. Dürig, D. W. Pohl, and F. Rohner. Near-field optical-scanning microscopy. *Journal of Applied Physics*, (10):3318–3327, 1986.

[187] D. W. Pohl, W. Denk, and M. Lanz. Optical stethoscopy: Image recording with resolution $\lambda/20$. *Applied Physics Letters*, (7):651–653, 1984.

[188] Eric Betzig and Robert J. Chichester. Single molecules observed by near-field scanning optical microscopy. *Science*, (5138):1422–1425, 1993.

[189] R. Zhang, Y. Zhang, Z. C. Dong, S. Jiang, C. Zhang, L. G. Chen, L. Zhang, Y. Liao, J. Aizpurua, Y. Luo, J. L. Yang, and J. G. Hou. Chemical mapping of a single molecule by plasmon-enhanced raman scattering. *Nature*, (7452):82–86, Jun 2013.

[190] R. Hillenbrand, T. Taubner, and F. Keilmann. Phonon-enhanced light-matter interaction at the nanometre scale. *Nature*, (6894):159–162, Jul 2002.

[191] Jianing Chen, Michela Badioli, Pablo Alonso-Gonzalez, Sukosin Thongrattanasiri, Florian Huth, Johann Osmond, Marko Spasenovic, Alba Centeno, Amaia Pesquera, Philippe Godignon, Amaia Zurutuza Elorza, Nicolas Camara, F. Javier Garcia de Abajo, Rainer Hillenbrand, and Frank H. L. Koppens. Optical nano-imaging of gate-tunable graphene plasmons. *Nature*, (7405):77–81, Jul 2012.

[192] Wei Bao, M. Melli, N. Caselli, F. Riboli, D. S. Wiersma, M. Staffaroni, H. Choo, D. F. Ogletree, S. Aloni, J. Bokor, S. Cabrini, F. Intonti, M. B. Salmeron, E. Yablonovitch, P. J. Schuck, and A. Weber-Bargioni. Mapping local charge recombination heterogeneity by multidimensional nanospectroscopic imaging. *Science*, (6112):1317–1321, 2012.

[193] Eric A. Muller, Benjamin Pollard, Hans A. Bechtel, Peter van Blerkom, and Markus B. Raschke. Infrared vibrational nanocrystallography and nanoimaging. *Science Advances*, (10), 2016.

[194] W. D. Herzog, M. S. Ünlü, B. B. Goldberg, G. H. Rhodes, and C. Harder. Beam divergence and waist measurements of laser diodes by near-field scanning optical microscopy. *Applied Physics Letters*, (6):688–690, 1997.

[195] Sergey I. Bozhevolnyi. Topographical artifacts and optical resolution in near-field optical microscopy. *J. Opt. Soc. Am. B*, (9):2254–2259, Sep 1997.

[196] N. Lindenmann, G. Balthasar, D. Hillerkuss, R. Schmogrow, M. Jordan, J. Leuthold, W. Freude, and C. Koos. Photonic wire bonding: a novel concept for chip-scale interconnects. *Opt. Express*, (16):17667–17677, Jul 2012.

[197] Philipp-Immanuel Dietrich, Gerald Göring, Mareike Trappen, Matthias Blaicher, Thomas Schimmel, Hendrik Hölscher, and Christian Koos. Highly integrated 3d printed scanning probe microscope with fiber actuation and sensing. *Manuscript prepared for submission*, 2018.

[198] T. J. Drapela, D. L. Franzen, A. H. Cherin, and R. J. Smith. A comparison of far-field methods for determining mode field diameter of single-mode fibers using both gaussian and petermann definitions. *Journal of Lightwave Technology*, (8): 1153–1157, Aug 1989.

[199] L. Raddatz, I. H. White, D. G. Cunningham, and M. C. Nowell. An experimental and theoretical study of the offset launch technique for the enhancement of the bandwidth of multimode fiber links. *Journal of Lightwave Technology*, (3):324–331, Mar 1998.

[200] M. Moehrle, J. Kreissl, W. D. Molzow, G. Przyrembel, C. Wagner, A. Sigmund, L. Moerl, and N. Grote. Ultra-low threshold 1490 nm surface-emitting bh-dfb laser diode with integrated monitor photodiode. In *2010 22nd International Conference on Indium Phosphide and Related Materials (IPRM)*, pages 1–4, May 2010.

[201] S. Sederberg and A. Y. Elezzabi. Nanoscale plasmonic contour bowtie antenna operating in the mid-infrared. *Opt. Express*, (16):15532–15537, Aug 2011.

[202] Anatoly V. Zayats and David Richards (Prof.). *Nano-optics and near-field optical microscopy*. Boston: Artech House, 2009. ISBN 9781596932845.

[203] Satoshi Takahashi, Wayne Dickson, Robert Pollard, and Anatoly Zayats. Near-field magneto-optical analysis in reflection mode snom. *Ultramicroscopy*, (3):443 – 447, 2004.

[204] B. Hecht, H. Bielefeldt, Y. Inouye, D. W. Pohl, and L. Novotny. Facts and artifacts in near-field optical microscopy. *Journal of Applied Physics*, (6):2492–2498, 1997.

[205] C. Durkan and I. V. Shvets. Reflection-mode scanning near-field optical microscopy: Influence of sample type, tip shape, and polarization of light. *Journal of Applied Physics*, (3):1171–1176, 1998.

[206] Masaru Muranishi, Kazutaka Sato, Sumio Hosaka, Atsushi Kikukawa, Toshimichi Shintani, and Kenchi Ito. Control of aperture size of optical probes for scanning near-field optical microscopy using focused ion beam technology. *Japanese Journal of Applied Physics*, (7B):L942, 1997.

Closing Words

It is a pleasure to thank all my friends, colleagues and institutions for the support and helpful discussions.

First of all, I want to thank Prof. Dr. Thomas Schimmel and Prof. Dr. Gerd Ulrich Nienhaus for the support and the chance two write this thesis at the Institute of Applied Physics (APH).

A special thanks goes to PD Dr. Hendrik Hölscher from the Institute of Microstructure Technology (IMT), for the co-integration into his group, which helped me with further discussions and new ideas to develop this project. He set the ball rolling for this thesis by his idea to write a 3D printed tip.

This work would not exist without the ideas and innovations of Philipp-Immanuel Dietrich from the Institute of Photonics and Quantum Electronics (IPQ). Supported by our former master student Mareike Trappen, he was responsible for various design calculations, simulations and the fabrication. He was the colleague who wanted to push the most out of this project.

Furthermore, I want to thank all my colleagues from my working group for the support and all the different proofreaders, Dr. Stefan Walheim, Dr. Roland Gröger, Dr. Florian Wertz, Dr. Jonathan Berson, Torben Staiger, Alan Jones and my dear friend Anja Holzberg. Each of those delivered various correction proposals.

It is also a pleasure to thank Paul Abaffy for numerous hours at the SEM and Richard Thelen for the inspirations during the measurements in the clean room at the IMT, which also shortened the time during long measurements.

Not to forget the hard working bees, keeping the university running: The mechanics workshop with its leader Frank Landhäußer which produced the mechanical parts for the setup. The team from the electronics workshop, Michael Hippe, Helmuth Lay and Werner Gilde, which supported me with fruitful discussions, circuits and an optimally working IT-infrastructure and the office with Ursula Mösle, Claudia Alaya and Monika Brenkmann which supported me at various paperworks and always kept me up to date.

I also want to thank Claudius Beuthner and Tim Schwarzkopf for the hard work-outs in the evening, which helped to stay focused during the thesis.

Finally, I would like to thank Lisa Köhler and our families for their understanding and loving support especially during the last years.